END-OF-INJECTION EFFECTS ON DIESEL SPRAY COMBUSTION

A Dissertation
Presented to
The Academic Faculty

by

Benjamin W. Knox

In Partial Fulfillment
of the Requirements for the Degree
Doctor of Philosophy in the
School of Mechanical Engineering

Georgia Institute of Technology
December 2016

END-OF-INJECTION EFFECTS ON DIESEL SPRAY COMBUSTION

Approved by:

Dr. Caroline Genzale, Advisor
School of Mechanical Engineering
Georgia Institute of Technology

Dr. Srinivas Garimella
School of Mechanical Engineering
Georgia Institute of Technology

Dr. Wenting Sun
School of Mechanical Engineering
Georgia Institute of Technology

Dr. Jerry Seitzman
School of Aerospace Engineering
Georgia Institute of Technology

Dr. Lyle Pickett
Combustion Research Facility
Sandia National Laboratories

Date Approved: 25 August 2016

ACKNOWLEDGEMENTS

I would like to thank the many people who have supported me throughout the years. Any successes I've had and any obstacles I've overcome would not have been possible without them. To my advisor, Dr. Caroline Genzale: thank you for developing me as a professional. You were always patient, supportive, and allowed me the freedom to pursue my goals. These are characteristics of a true educator. To my parents, Tim and Sally Knox: you loved me unconditionally and supported me through whatever I wanted to do (within reason of course :)). Your marriage was an excellent model and gave me a primer for my marriage. To my amazing wife, Nicole: its true, I *am* waterproof! You have taught me so much and I can only hope to keep learning new things from you. You kept me together these past few years and I am truly grateful.

An old African proverb says that *it takes a village to raise a child.* I think there is much truth to this in the context of academia. My advisor, class professors, qualification exam committee, dissertation committee have in many ways raised me. To them and for my entire experience at Georgia Tech, I am truly grateful.

In no particular order, I would like to thank the following Combustion Lab folks for their involvement in my life: Gina Magnotti (Sforzo), Thomas Furlong, Mike Tree, Dr. John (Matt) Quinlan, Dr. Chris Foley, Ianko Chterev, Dr. Prabhakar Venkateswaran, Dr. Andrew Marshall, Brad Ochs, Dr. David Scarborough, Dr. Bobby Noble, Dr. Ben Emerson, David Wu, Dr. Brandon Sforzo, Sayop Kim, Dr. Dorrin Jarrahbashi, Darshan Pahinkar, Aimee Williams, Dr. Nick Magina, Sampath Adusumilli, and Dr. Vishal Acharya. Details of any specific activities have been intentionally omitted for fear of self-incrimination :)

TABLE OF CONTENTS

vi

LIST OF TABLES

LIST OF FIGURES

NOMENCLATURE

A Jet cross-sectional area.

A_a Ambient cross-sectional area.

A_{eff} Effective orifice area.

A_f Fuel cross-sectional area.

A_{geo} Geometric orifice area.

α Characteristic timescale of velocity decrease.

ASI   After start-of-injection.

ASORD   After start-of-ramp-down.

β Transition parameter.

C Constant.

C_a Orifice area contraction coefficient.

C_d Discharge coefficient.

C_e Entrainment coefficient.

χ Scalar dissipation rate.

CO   Carbon monoxide.

C_v Velocity coefficient.

Da Damköhler number.

d_{ap} Aperture diameter.

d_{eff} Effective orifice diameter.

δ Limiting location for ignition.

d_m Momentum diameter.

d_o Geometric orifice diameter.

$\dot{M}$ Jet momentum rate.

$\dot{m}_a$ Ambient mass flow rate.

$\dot{m}_{ent}$ Entrainment mass flow rate.

$\dot{m}_f$	Fuel mass flow rate.
$\dot{m}_o$	Orifice mass flow rate during steady injection.
D_Z	Mixture fraction diffusivity.
EGR	Exhaust gas recirculation.
EOI	End-of-injection.
f	Focal length.
FLOL	Flame lift-off length.
f_n	Resonant frequency.
γ	Inflection point location.
h	Enthalpy of jet.
h_a	Enthalpy of ambient gases.
HTC	High-temperature combustion.
K	Nurick cavitation number.
k_c	Coverage factor.
KHP	Ketohydroperoxides.
KL	Optical thickness.
$\langle R \rangle$	Ensemble-averaged combustion recession metric.
LLFC	Leaner lifted-flame combustion.
LTC	Low-temperature combustion.
M	Jet momentum.
m_a	Ambient mass.
m_f	Fuel mass.
m_{inj}	Total injected mass.
N	Total number of injections.
NOx	Nitrogen oxides.
NTC	Negative temperature coefficient.
$\overline{\dot{M}_f}$	Time-averaged fuel momentum rate.

P_a	Ambient pressure.
PAH	Polycyclic aromatic hydrocarbons.
ϕ	Equivalence ratio.
ϕ_s	Stoichiometric mass ratio.
P_{inj}	Injection pressure.
PLIF	Planar laser-induced fluorescence.
PPCI	Partially-premixed compression-ignition.
P_v	Vapor pressure.
Q	Alkene.
R	Alkyl radical.
R	Individual combustion recession metric.
RD	Ramp-down.
R_F	Reaction force.
ρ	Jet density.
ρ_a	Ambient density.
ρ_f	Fuel density.
σ_A	Precision uncertainty.
σ_B	Systematic uncertainty.
σ_C	Combined uncertainty.
σ_{x_j}	Individual uncertainty.
S_L	Laminar flame speed.
t	Time.
T_a	Ambient temperature.
τ_{ign}	Ignition timescale.
τ_{res}	Residence timescale.
TCI	Turbulence-chemistry interaction.
T_f	Fuel temperature.

θ	Full spreading angle.
U	Velocity.
U_{eff}	Effective injection velocity.
UHC	Unburned hydrocarbons.
U_o	Injection velocity at orifice exit during steady conditions.
V	Jet volume.
x	Axial distance from orifice exit.
x'	Axial distance from orifice virtual origin.
X_f	Fuel volume fraction.
x_i	Axial length of distinct ignition pockets.
x_{NR}	Axial distance not resolved near orifice exit.
x_o	Axial distance from orifice virtual origin to orifice exit.
x_R	Recessed flame length.
Y_i	Jet species mass fractions.
$Y_{i,a}$	Ambient species mass fractions.
Z	Mixture fraction.
Z_{st}	Stoichiometric mixture fraction.

SUMMARY

Increasingly stringent emissions regulations have created a demand for cleaner burning engines. Low-temperature combustion (LTC) strategies have been proposed to meet low soot and nitrogen oxides emissions but LTC strategies suffer from excessive unburned hydrocarbon (UHC) and carbon monoxide (CO) emissions. These emissions have been shown to originate from overly fuel-lean mixtures near the nozzle that do not burn to completion. These mixtures are said to be *over-mixed* beyond a flammability limit and are caused by increased entrainment during end-of-injection. The coupling between end-of-injection entrainment and incomplete combustion of near-nozzle mixtures is not well understood, however, in part due to the large parameter space in engines. Thus, this thesis aims to develop tools and models to measure end-of-injection combustion observables and predict the likelihood of UHC and CO emissions over a wide range of conditions.

This thesis seeks to perturb the coupling between end-of-injection entrainment and incomplete combustion of near-nozzle mixtures by systematically varying the ambient thermodynamic conditions, injection parameters, as well as the end-of-injection transient. To this end, three significant developments were made: a novel injection system that can vary the end-of-injection transient on command, a measurement technique to quantify the transient injection rate with high confidence, and characterization of three simultaneous, high-speed optical diagnostics for measurements of end-of-injection combustion observables. Four distinct behaviors of the spray flame following end-of-injection were identified: *soot recession*, *complete combustion recession*, *partial combustion recession*, and *no/weak combustion recession*. Combustion

recession is the process whereby the initially lifted reaction zone retreats back towards the nozzle immediately following end-of-injection, thus consuming UHC/CO that would otherwise remain near the nozzle. Soot recession spatially and temporally overlaps with combustion recession and is the result of igniting rich mixtures. Regression of a comprehensive dataset indicates that combustion recession is promoted with higher ambient temperatures, higher ambient oxygen concentrations, higher ambient densities, longer end-of-injection transients, lower injection pressures, and larger nozzle orifice diameters. Similar trends are observed for soot recession as well.

Rather than rely solely on regression for predictions of combustion recession, a first-principles based approach was used to develop a scaling law for combustion recession that is applicable to a wider class of injectors and injection strategies than those tested experimentally. A new reduced-order model, premised on the similarity between diesel sprays and dense turbulent gas-jets, was developed that captures only key physics regarding combustion recession. This model was used to better understand the coupling between end-of-injection mixing and near-nozzle ignition timescales that are thought to control combustion recession. Using a definition for the local Damköhler number throughout the jet, a limiting location of ignition was identified and linked to the flame lift-off length to develop both an end-of-injection ignition timescale and a steady injection ignition timescale. The proportionality between the two timescales was used to predict the likelihood of combustion recession and thus UHC/CO emissions.

CHAPTER I

INTRODUCTION

1.1 Motivation

Diesel engine technologies are a promising candidate to meet the global demand for high efficiency engines due to their superior peak thermal efficiencies. While diesel engines are capable of high thermal efficiencies, emissions regulations can be challenging to meet, which is why much research has been devoted to understanding the physical mechanisms that are responsible for each regulated pollutant. Historically, previous emissions regulations were achieved with in-cylinder strategies such as high injection pressure, low or moderate amounts of exhaust gas recirculation (EGR), or improved combustion chamber design, rather than with aftertreatment. Now though, emissions regulations for particulate matter, nitrogen oxides (NOx), and unburned hydrocarbons (UHC) are 2%, 3-12%, and 6-12% of their 1990 levels suggesting the use of aftertreatment to meet these demands [1]. However, aftertreatment use suffers from higher economic costs, durability issues, and fuel economy penalties providing motivation for further research to meet emissions regulations in-cylinder.

To meet emissions regulations in-cylinder, low-temperature combustion (LTC) strategies have received much attention in recent years [2, 3, 4, 5, 6, 7, 8, 9]. LTC strategies strive to lower in-cylinder combustion temperatures, thereby slowing NOx formation kinetics, and increase mixing prior to combustion to bring local fuel-ambient ratios below a sooting limit. This thesis is focused on a particular LTC strategy known as partially-premixed compression-ignition (PPCI) where the injection event is still coupled to combustion but with longer mixing times relative to more conventional diesel strategies. PPCI shows great promise but suffers from high UHC

and carbon monoxide (CO) emissions that originate from overly lean mixtures near the nozzle due to end-of-injection entrainment.

Recent research on PPCI strategies has linked these high UHC and CO emissions to end-of-injection processes that inhibit combustion from going to completion [4, 10, 11]. However, only a few attempts, namely multiple injections and piston bowl redesign, have been made to mitigate these high UHC and CO emissions in-cylinder with limited success [12, 13]. Part of the reason for the limited success in mitigating UHC and CO emissions is due to the lack of knowledge regarding the link between end-of-injection processes and combustion. Furthermore, *a priori* knowledge of the exact conditions for which unacceptable levels of these emissions are expected is not available. Thus, this thesis aims to develop tools and models to measure end-of-injection combustion observables and predict the likelihood of UHC and CO emissions over a wide range of engine operating conditions and injectors.

The rest of this chapter is dedicated to the fundamental in-cylinder spray, combustion, and emission processes that are relevant to diesel engines. This knowledge forms the foundation for which the measurement tools and modeling approaches are based.

1.2 Background and Literature Review

1.2.1 High-temperature combustion (HTC)

A wealth of knowledge and generally accepted conceptual model has been generated by other researchers for HTC [14], shown in Figure 1. The sequence begins by injecting high pressure liquid fuel (generally in the range of 400-1200 bar) through orifices ($\sim$100-300 µm in diameter) at the tip of the injector. As the fuel penetrates into the combustion chamber, it forms a spray (color - maroon), shown at 140 µs after start-of-injection (ASI). This time is not universal to all diesel combustion conditions but rather illustrates the short time durations over which the process takes place. While

the fuel penetrates further into the chamber, the spray continuously entrains hot air from the ambient environment. The ambient environment need not be just air; it could contain recirculated products, or EGR. Depending on ambient thermodynamic conditions and injector parameters, as well as fuel properties, the liquid spray will have completely vaporized by a steady distance from the orifice (555 µs ASI), often called the liquid length.
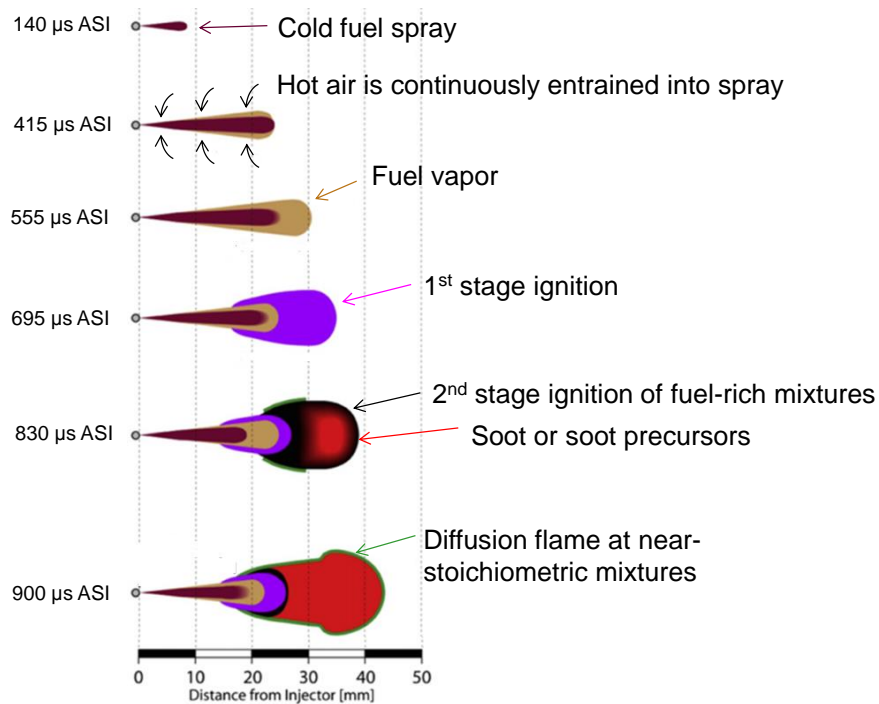
Figure 1: Example time sequence of diesel direct-injection under high-temperature combustion (HTC) conditions [1].

The spray then becomes a jet since the penetrating fuel is single phase and gaseous. Due to its momentum, the fuel vapor jet (color - tan) will continue to penetrate into the chamber and entrain the surrounding ambient gases. By 695 µs ASI, fuel-air mixtures at the jet head are now more fuel lean and warmer than they were at previous time instances. Thus, they have reached a more reactive mixture state and have had sufficient time for the parent fuel molecule to break down and begin the transition to a fully burned state. The first identifiable phase in the transition to

a fully burned state is called first-stage ignition (color - magenta). In this phase, a small amount of heat is produced and certain combustion intermediates, e.g. CH_2O, are identifiable experimentally [15]. This is the first of two stages of ignition, if using diesel-like fuel under HTC conditions. While fuel-air mixtures at this stage are more fuel lean than they were at previous instances in time, they are still rich compared to stoichiometric. After first-stage ignition, these fuel-rich mixtures at the head of the jet undergo second-stage ignition (color - black). This is the final stage in the transition to a fully burned state where a large amount of heat is produced and other radicals, e.g. electronically-excited OH* and CH* are some of the most notable, are observed experimentally [16]. Since these igniting mixtures are fuel rich, they tend to form soot and/or soot precursors (color - red), e.g. polycyclic aromatic hydrocarbons (PAH) [14]. Finally, the jet reaches a quasi-steady condition where a diffusion flame envelopes the core.

The quasi-steady lifted flame is shown in more detail in Figure 2. The distance from the orifice to the most upstream region of the enveloping diffusion flame is called the flame lift-off length. Soot, a major component of particulate matter, begins to form at this axial location and continues through many stages of growth before being partially oxidized in a diffusion flame at the periphery of the jet. Near the diffusion flame where combustion temperatures are high, NOx formation is high primarily due to the Zeldovich mechanism, which is strongly dependent on temperature [17].

In the absence of EGR, the flame lift-off length magnitude has been shown to correlate well with the amount of soot produced [18, 19], with more soot being generated for shorter flame lift-off lengths. Siebers and coworkers demonstrated a simple scaling law for the flame lift-off length, $FLOL$, as a function of many parameters: ambient gas temperature, T_a; ambient gas density, ρ_a; nozzle orifice diameter, d_0; injection velocity, U_f; as well as the stoichiometric mixture fraction, Z_{st}, which accounts for ambient oxygen concentration and fuel properties [18],
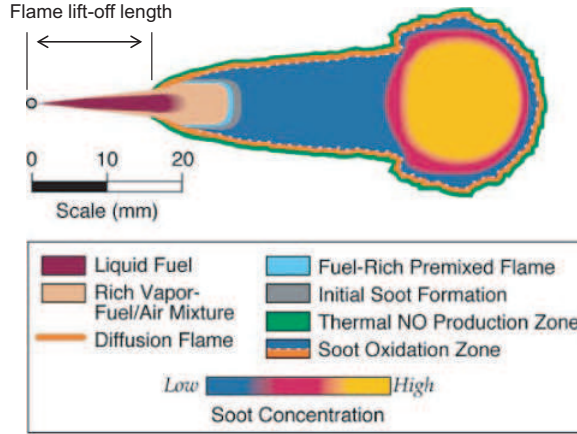
Figure 2: Diesel combustion conceptual model from Dec [14].

$$FLOL \propto T_a^{-3.74} \rho_a^{-0.85} d_0^{0.34} U_f^1 Z_{st}^{-1}. \tag{1}$$

The exponent values for each parameter in Eq. 1 illustrate the dependence of flame lift-off length, and thus the potential for soot, on each parameter with larger absolute values indicating greater dependence. From this equation, we can see that ambient temperature is the greatest contributor whereas nozzle orifice size is the least.

1.2.1.1 Mixing and Entrainment

Building on the analysis of Wakuri [20], Naber and Siebers [21] developed one of the first reduced-order models that successfully captured many of the experimentally observed trends regarding mixing in diesel sprays. By assuming a 1-D, isothermal, incompressible high-density gas-jet with fixed spreading angle, they used an integral control surface technique to develop a scaling law for diesel spray penetration, shown in Figure 3. Though several empirical correlations for spray penetration had been previously proposed [22, 23, 24], they were typically reliant on multiple empirical constants and yielded a wide range of scatter in predicted results. In treating the diesel spray as a dense, turbulent gas-jet, Naber and Siebers were able to provide a predictive

relationship between diesel jet penetration and jet/ambient densities, indicating that diesel sprays are predominantly mixing-controlled rather than atomization-controlled, and justifying the analogy of mixing in diesel sprays to that of a gas-jet. The term *mixing* describes the entrainment of ambient fluid into the spray and the overall transport throughout the cross-section.
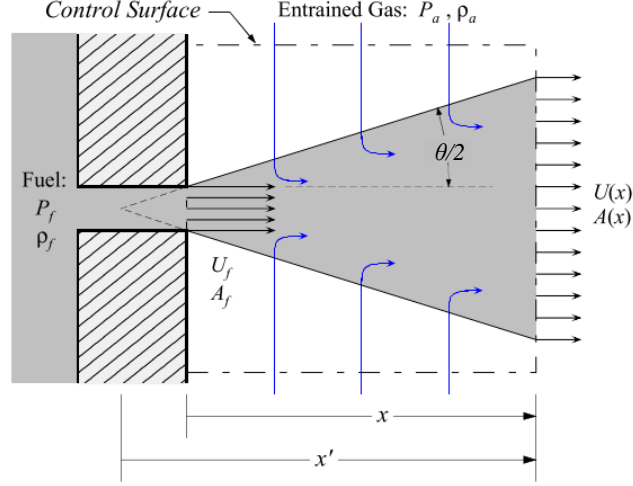
Figure 3: Schematic of spray model assuming 1-D, isothermal, incompressible high-density gas-jet with fixed spreading angle [21].

Based on their analysis, we can analyze the ratio of local fuel and ambient flow rates to understand how changes in the orifice flow or ambient fluid affect the mixing of the jet. In Eq. 2, the fuel mass flow rate, $\dot{m}_f$, is written as a function of fuel mass density, ρ_f, fuel velocity at the orifice exit $(x = 0)$, $U_f(0)$, and orifice exit area, $A_f(0)$. The ambient mass flow rate, $\dot{m}_a$, is written as a function of ambient mass density, ρ_a, jet velocity at x, $U(x)$, and jet area occupied by the ambient gas at x, $A_a(x)$.

$$\frac{\dot{m}_f}{\dot{m}_a} = \frac{\rho_f U_f(0) A_f(0)}{\rho_a U(x) A_a(x)} \tag{2}$$

By assuming that the area occupied by the fuel is small relative to the jet area $(A_a(x) \approx A(x))$ and using the equations for fuel mass and total momentum in Ref. [21], an equation for the jet velocity can be substituted into Eq. 2 to yield the

6

relation in Eq. 3. The terms C_a, θ, and d_0 represent the nozzle orifice area contraction coefficient, full spray spreading angle, and nozzle orifice diameter, respectively. Notice that the fuel-air ratio does not depend on the fuel velocity (injection pressure), since these terms canceled out in the substitution. The fuel mass flow rate is balanced by the ambient gas flow rate, resulting in no dependence of the axial distribution of the fuel-ambient ratio on injection pressure for steady sprays. However, the residence time history, which will become important when combustion is coupled to this mixing behavior, is dependent on injection pressure.

$$\frac{\dot{m}_f}{\dot{m}_a} \propto \frac{\rho_f C_a d_0^2 U_f(0)}{\sqrt{\rho_f \rho_a}\sqrt{C_a}d_0 U_f(0)x\tan(\theta/2)} \propto \frac{\sqrt{C_a}d_0\sqrt{\rho_f/\rho_a}}{x\tan(\theta/2)} \tag{3}$$

Unfortunately, because internal nozzle flows and turbulent mixing of the spray are not well understood, no universal theory exists for the spray spreading angle as a function of the parameters involved [25]. The spray spreading angle is thus experimentally determined and represents the jet's growth rate due to ambient gas entrainment. The effect of entrained ambient gas on the fuel-air distribution is twofold: directly from the ambient gas density itself, and from the dependence of the spray spreading angle on ambient gas density. As the ambient density increases, the spray spreading angle increases resulting in higher entrainment. Measurements of the far-field spray spreading angle, during the quasi-steady portion of injection (i.e. after passage of the transient head vortex), have shown that this angle is independent of axial position and time indicating that the entrainment varies linearly with distance much like a turbulent gas-jet [25]. Furthermore, at higher ambient density, typical angles were found to approach $\tan(\theta/2) \approx 0.22$ to 0.29, which are often measured for incompressible, fully developed gas-jets.

One reason for the similarity between diesel sprays and gas-jets is that typical injection pressures are quite high, and thus, the exiting flow is in the atomization

regime, which tends to exhibit rapid breakup and produce very small droplets. Simulations from Bajaj suggest that as the droplet size, or Sauter Mean Diameter (SMD), is reduced, the incompressible gas-jet approximation becomes better [26]. This is because the momentum transfer rate increases with decreasing droplet size. Even under vaporizing conditions the gas-jet approximation appears reasonable, due to the fact that Naber and Siebers found only moderate differences between vaporizing and non-vaporizing sprays for diesel relevant conditions [21]. As the nozzle orifice diameter increases, fuel density increases, or ambient gas density decreases, the deviation between vaporizing and non-vaporizing sprays becomes worse, however [21]. SMD also increases with increasing nozzle orifice diameter, increasing fuel density, and decreasing ambient gas density, which is consistent with the concepts introduced by Bajaj in that as SMD increases, the incompressible gas-jet approximation becomes worse.

The discrepancy between non-vaporizing and vaporizing diesel sprays under some conditions may be attributed to contraction of the jet in the near-field of the spray. The contraction is caused by an increase in gas phase density and a decrease in gas phase temperature. Increased gas phase density can be attributed to the increase in molecular weight from the heavier fuel molecule compared to air while the decrease in temperature is due to the lower temperature fuel (sensible enthalpy effect) and the latent heat of vaporization (cooling effect) [26]. From a thermodynamic perspective, however, as ambient gas density increases and thus the pressure approaches the critical pressure of the fuel, the latent heat of vaporization decreases to zero suggesting that the cooling effect is small relative to the sensible enthalpy effect.

The similarity of diesel sprays to gas-jets, at certain conditions, could also be explained by the recent experimental observations from Manin et al. [27] and the recent theoretical work from Dahms and Oefelein [28]. Manin et al. found no evidence of droplets at sufficiently high ambient temperatures and pressures suggesting that

surface tension effects were reduced, consistent with the behavior of a supercritical fluid [27]. Under these conditions, Dahms and Oefelein argued that diesel sprays may fall under the diffusion-controlled mixing category as opposed to being dominated by classical two-phase atomization processes, shown in Figure 4 [28]. They related the Knudsen number, $Kn = \lambda/L$, to spray mixing by using the thickness of the density profile at the droplet interface as the physical length scale, L, and the mean free path, λ. At small Kn, $Kn \ll 1$, the system is in the continuum regime and diffusion processes dominate while at $Kn \gg 1$, two-phase atomization processes dominate. They do acknowledge, however, that since the fuel temperature is below the critical temperature there will likely be a transition from atomization-controlled to diffusion-controlled mixing as the spray penetrates into the ambient gases.
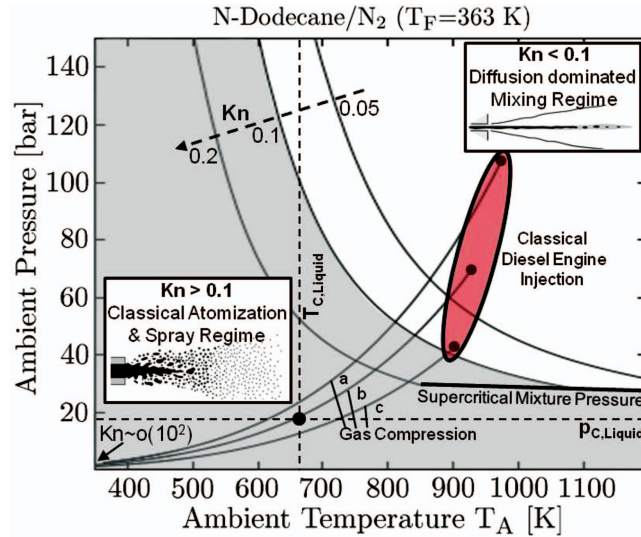
Figure 4: Regime diagram for n-dodecane injected into gaseous nitrogen at varying ambient pressures and temperatures, adapted from Dahms and Oefelein [28].

The studies outlined above suggest that diesel sprays can be understood from a gas-jet point of view for many conditions of interest. These conditions include high ambient densities, small nozzle orifice diameters, and high injection pressures - even at high ambient temperatures where the spray is vaporizing. Whether the physical reasoning for the similarity between diesel sprays and gas jets is attributed to small

droplet sizes or diffusion-controlled mixing or both, the utility is the same. This thesis takes advantage of these findings by modeling the spray as a simple gas-jet to better understand the coupling between end-of-injection processes, ignition, and UHC/CO emissions in near-nozzle mixtures.

1.2.1.2   Ignition and Flame Stabilization

The basic processes of mixing and entrainment leading to autoignition in diesel sprays were outline above. Below, autoignition and the reaction pathways that occur in tandem with mixing and entrainment will be discussed, followed by relevant flame stabilization mechanisms.

Diesel fuel generally contains a large fraction of saturated hydrocarbons, both paraffinic and cycloparaffinic, and a smaller amount of aromatics. Since diesel is chemically quite complex, the chemical kinetics of simpler fuels that are representative of diesel (large, saturated, straight-chained paraffins) will be discussed. Westbrook explains that the key to understanding ignition kinetics is to identify the chain branching steps, where the number of radicals increases, under the conditions being studied [29]. After initiation reactions from thermal decomposition, i.e. pyrolysis, the parent fuel molecule (a paraffin, or alkane, in this simplified case) produces alkyl radicals, R. These smaller hydrocarbons then react to produce H and O atoms where under high temperature conditions (>1200 K), the dominant chain branching reaction is one that consumes H atoms and produces two radicals, O and OH:

$$H + O_2 \Rightarrow O + OH \tag{4}$$

At temperatures below 1200 K but above 850 K, reaction 4 is too slow and a different reaction path dominates. Important reactions include the following:

$$H + O_2 + M \Rightarrow HO_2 + M \tag{5}$$

$$RH + HO_2 \Rightarrow R + H_2O_2 \tag{6}$$

10

$$H_2O_2 + M \Rightarrow OH + OH + M \tag{7}$$

where RH is an alkane and M is a third body. Reactions 5-7, as a whole, may be considered a chain branching sequence because they consume one H radical and produce two OH radicals. In many systems, the dominant characteristic is the build-up of H_2O_2 until a critical temperature is reached followed by rapid decomposition and then ignition. At atmospheric pressure, H_2O_2 decomposes around 1000 K. However, with increasing pressures, decomposition occurs at lowers temperatures - generally in the range 900-1000 K for diesel relevant pressures.

At lower temperatures (<850 K), O_2 combines with the alkyl radical that was originally produced by thermal decomposition of the parent fuel molecule:

$$R + O_2 + M \Rightarrow RO_2 + M \tag{8}$$

The alkylperoxy radical, RO_2, then isomerizes to produce a hydroalkylperoxy radical, QOOH, where Q represents an alkene:

$$RO_2 \Rightarrow QOOH \tag{9}$$

QOOH radicals may react via a few different paths:

$$QOOH \Rightarrow Q + HO_2 \tag{10}$$

$$QOOH \Rightarrow QO + OH \tag{11}$$

to create an HO_2 or OH radical, in addition to a stable alkene or cyclic ether (QO). It is also possible for O_2 to combine with QOOH to creating another radical, O_2QOOH, which can then isomerize further:

$$QOOH + O_2 \Rightarrow O_2QOOH \tag{12}$$

This radical then decomposes into a relatively stable ketohydroperoxide (KHP) species and an OH radical. KHP species decompose at about 800 K, where it breaks

into at least two radicals - a chain branching step. This phase of oxidation continues until the temperature reaches approximately 850 K, where reactions 8-12 shift towards dissociation. The rapid consumption of KHP leads to the so-called "negative temperature coefficient" (NTC) regime, where heat release rates slow despite increasing temperature. Illustration of the NTC regime, along with the effect of pressure on the temperature range for each set of dominating reactions is shown in Figure 5a. Furthermore, the two stages of ignition are also a consequence of this KHP behavior. Each stage and the important intermediates associated with their development are shown in Figure 5b.
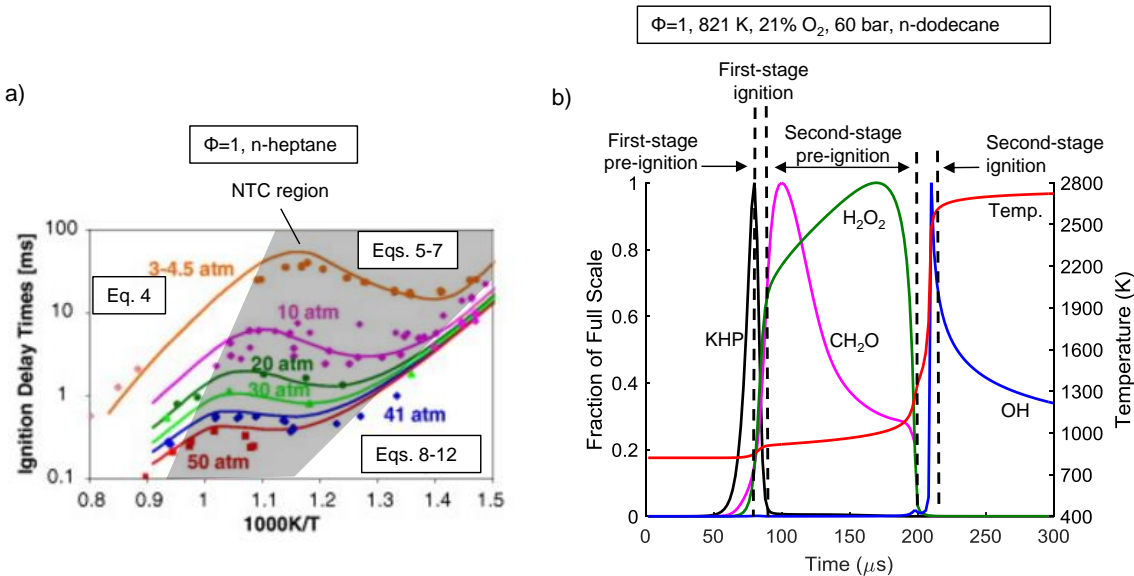
Figure 5: a) Illustration of NTC regime and dominating reactions from Mehl et al. [30] and b) illustration of two-stage ignition processes adapted from Musculus et al. [1]

Since mixing in diesel sprays occurs simultaneously with these ignition kinetics, it is common to consider the ignition delay as comprising a physical and chemical delay. The physical delay refers to the time required to prepare a fuel-air mixture to a ratio where any significant chemical activity may occur. This delay includes the time required for atomization, evaporation, and mixing. Turbulent mixing in non-premixed systems, e.g. diesel sprays, can delay ignition due to heat and species loss from an

igniting kernel if high scalar dissipation rates are observed, $\chi = 2D_Z(\nabla Z \cdot \nabla Z)$. Here, D_Z represents the mixture fraction diffusivity and Z is the local mixture fraction. Low scalar dissipation rates, however, allow radicals and heat to accumulate during the induction time, which leads to autoignition [31]. In the context of diesel spray combustion, Bolla et al. investigated the influence of turbulence-chemistry interactions (TCI) by employing the conditional moment closure model for TCI and comparing results of ignition delay to a "direct-integration" model, for which turbulent fluctuations of species and temperature on reaction rates are neglected [32]. They found that the influence of TCI on ignition delay is small for a wide range of ambient densities and oxygen concentrations because ignition occurs in regions of low χ, much lower than the critical χ where the delaying effects of TCI become important. Even though dilution decreases the critical χ for which autoignition becomes significantly delayed, ignition occurs further downstream with increasing dilution, to regions of low χ since χ decreases with increasing distance from the orifice.

The chemical delay refers to the sequence of reactions outlined above that must take place before thermal runaway, i.e. ignition. Even in the presence of atomization, evaporation, and mixing, the chemical delay can be understood as the minimum possible time for ignition in non-premixed systems. A very useful concept for ignition in turbulent non-premixed systems is the most reactive mixture fraction, where in the absence of a physical delay, the chemical ignition delay is at a minimum. This concept is especially helpful for understanding diesel spray combustion because many of the important turbulent quantities, e.g. χ and higher moments of other fluctuating quantities, are difficult to measure and have yet to be modeled adequately. For hydrocarbon-air mixtures at diesel relevant temperature and pressure, the most reactive mixture fraction is rich (about 1.5-2.5 in equivalence ratio).

Pei et al. used the ignition delay at the most reactive mixture fraction from a closed homogeneous reactor to estimate the ignition delay in an n-dodecane spray

13

and found surprising agreement [33]. Closed homogeneous reactor results can be thought of as a limit case in which a fluid element instantly achieves the state of the most reactive mixture thereby neglecting the added physical delay of evaporation and turbulent mixing [33]. To first order, perhaps bulk entrainment dominates any turbulence effects and the similarities to gas-jets reduces the necessity to model diesel sprays as very complex for many conditions. The reduced-order model presented in this thesis takes advantage of these key findings on mixing, entrainment, and TCI.

After ignition in a diesel spray, a stabilized flame is formed downstream of the nozzle orifice, referred to as a lifted flame. The flame lift-off length in diesel sprays is defined as the distance from the nozzle to reaction zone stabilization and follows the power-law trend given in Eq. 1. The fact that the flame is lifted is important because it allows fuel and air to mix upstream, and the amount of air entrained upstream can have a large impact on the amount of soot formed downstream.

In a pioneering study, Siebers and coworkers measured diesel spray flame lift-off lengths for various ambient gas conditions (temperature, pressure, oxygen concentration) and injector conditions (injection pressure, orifice diameter) [18]. This data was then compared to gas-jet diffusion flame lift-off trends, shown in Eq. 13, where the flame is believed to be stabilized by flame propagation processes.

$$FLOL \propto \frac{U_f Z_{st} \alpha_t}{[S_L(Z_{st})]^2} \tag{13}$$

Here, α_t, $S_L(Z_{st})$, and U_f represent the thermal diffusivity, laminar flame speed at the stoichiometric mixture fraction, and fuel velocity at the orifice exit, respectively. Essentially, the gas-jet diffusion flame will anchor along the stoichiometric contour and at a location where the turbulent flame speed upstream is balanced by the convective velocity downstream. While some of the same trends between diesel sprays and gas-jet diffusion flames were observed, others were not. Specifically, there is no dependence of FLOL on orifice diameter in Eq. 13 while there is a dependence in Eq. 1. This suggests that mechanisms other than flame propagation may play a role in diesel

14

spray flame lift-off stabilization.

Indeed, Pickett and coworkers observed a cool flame upstream of the flame lift-off length in diesel sprays, suggesting that ignition processes are continuously occurring upstream of the flame lift-off length [34]. The cool flame could also enhance flame speeds, however, meaning that it is difficult to say which mechanism (flame propagation or ignition) is dominant. Interestingly though, they also found evidence of second-stage ignition kernels that were upstream and detached from any combustion downstream at the flame lift-off length. If flame propagation were occurring, we would expect a connected reaction sheet that opposes the incoming flow of reactants. Lastly, shorter flame lift-off lengths were found for fuels with shorter ignition delays even though the flame speeds varied little between the different fuels. These findings suggest that ignition processes play an important, if not dominating, role in diesel spray flame lift-off stabilization.

Other flame lift-off stabilization mechanisms include a reservoir of high temperature, slow-moving, combustion products that surround the core of the jet and are left over from the autoignition event [35], shown in Figure 6. The products in Zone 3 are entrained into the reaction zone (Zone 2) and can help ignite fresh incoming mixtures from Zone 1. In an effort to understand flame stabilization mechanisms, Juneja, Ra, and Reitz simulated a ramp-up rate-of-injection, where the injection velocity increased after the flame has been stabilized, and found that the flame lift-off length did not increase as it should have if flame stabilization were controlled solely through fuel-air mixing, i.e. no mixing with combustion products [36]. In support of this modeling study, Pickett et al. used laser-induced plasma ignition to decouple the autoignition event, which creates the combustion product reservoir, from flame stabilization [35]. They measured the response of the reacting jet and found that the lifted flame persisted at the upstream laser ignition site for a substantial period of time before moving downstream to its "natural" position. They reasoned that a

reservoir of high-temperature combustion products feeds the reaction zone and helps stabilize the flame at the point of laser ignition. The reservoir eventually depletes and the flame returns to its "natural" lifted flame position because there is no continuous ignition source that fills the reservoir (like there would in the case of natural autoignition).
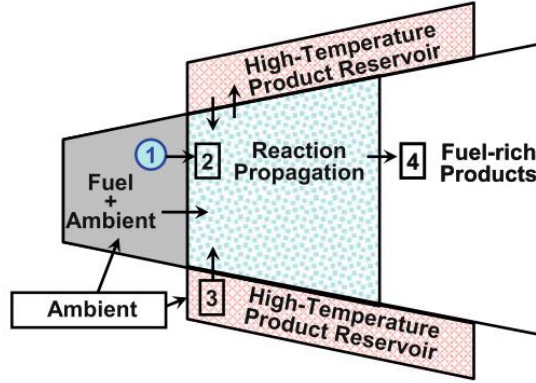
Figure 6: Schematic of additional lift-off stabilization mechanism [35].

1.2.2 Low-temperature combustion (LTC)

LTC strategies are generally achieved with any combination of lower ambient gas temperatures, densities, and oxygen concentrations, as well as smaller nozzle orifices and higher injection pressures, compared to HTC conditions. As seen in Eq. 1, changes to these parameters in these ways serves to increase the flame lift-off length and reduce the amount of soot formed. Lower ambient gas oxygen concentrations are achieved with cooled EGR where the reduced oxygen environment slows NOx formation kinetics and the diluent gases raise the thermal capacity of the combined ambient gases to reduce combustion temperatures. Lower ambient gas temperatures and densities are achieved by injecting earlier or later than top-dead center, which is primarily the timing for HTC conditions. The lower ambient gas temperatures and densities (pressures) delay ignition kinetics and allow for more premixing prior to combustion. Higher injection pressures, upwards of 3000 bar [37], and smaller nozzle

orifices, down to 50 μm [38], enhance mixing, which in turn allows for more premixing prior to combustion.

As was done for HTC, researchers have put forth a conceptual model for PPCI [1], shown in Figure 7. Only the later stage of the injection sequence is shown in the figure because previous instances in time undergo similar processes and share many of the same features to those shown in Figure 1. Comparing this PPCI conceptual model and the later stage of HTC reveals a striking difference. In the PPCI model, soot (color - red) appears only in small regions within the side lobes of the head vortex whereas soot fills the majority of the jet downstream of the flame lift-off length in the HTC model. There is no clear evidence of a diffusion flame surrounding the core of the jet but rather complete, second-stage combustion, without soot, is seen to nearly fill the jet (color - green). Unfortunately, while soot and NOx formation kinetics are slowed under PPCI conditions, ignition kinetics are also much slower, which makes complete combustion more difficult to achieve. From the figure, much of the jet near the nozzle (between 0 and 30 mm from the nozzle) contains only unburned fuel or formaldehyde, which is an indicator of incomplete combustion. It is important to note that liquid is not shown in the conceptual model because end-of-injection has already occurred. Thus, fuel is no longer being injected and has vaporized well before this stage. The coupling between end-of-injection and incomplete combustion, i.e. UHC emissions, will be the focus of this thesis.

1.2.2.1   *End-of-Injection Observations*

Before addressing the possible physical mechanisms responsible for the coupling between end-of-injection and incomplete combustion near the nozzle, a motivational study will first be presented. Musculus, Lachaux, Pickett and Idicheria compiled unpublished UHC emissions data from Cummins Inc. that spans a wide range of engine conditions and found that UHC emissions very quickly become unacceptable under
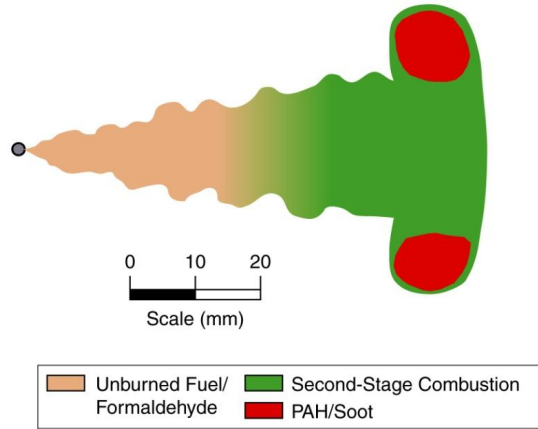
Figure 7: Diesel Partially-Premixed Compression-Ignition (PPCI) conceptual model from Musculus et al. [1]

conditions where the ignition dwell is positive [10]. Ignition dwell is referred to as the time between end-of-injection and ignition, or the start-of-combustion. HTC is often characterized by negative ignition dwell whereas LTC, or PPCI, is often associated with positive ignition dwell. This was the first known study to demonstrate the importance between end-of-injection processes on UHC emissions in engines over such a broad range of operating conditions and engine architectures that then motivated further study into end-of-injection processes.
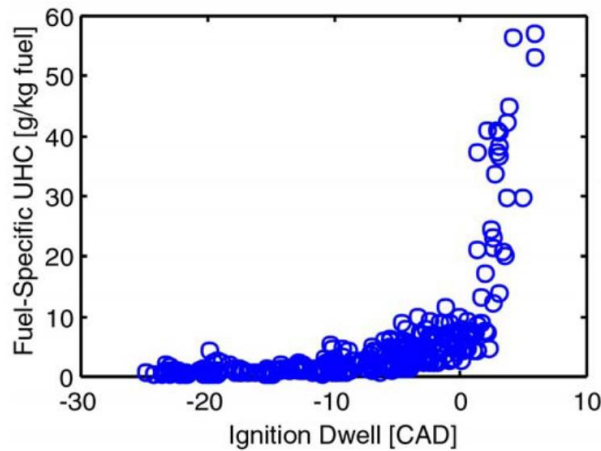
Figure 8: Correlation between unburned hydrocarbons (UHC) and ignition dwell from Musculus, Lachaux, Pickett, and Idicheria [10].

The mixing and entrainment behavior discussion presented earlier focused on the important findings for steady diesel sprays, which have many similarities to steady gas-jets. Relative to steady jets, much less information is available about the end-of-injection transient, or decelerating phase, on the evolution of jet fluid during this transition. Some information is available, however, from large-eddy simulations by Hu, Musculus, and Oefelein [39]. They show that compared to a steady jet, a decelerating jet exhibits larger indentations of the jet boundary. Near these indentations, large radial velocities are shown inward toward the core of the jet, which are evidence of entrainment by large-scale motions due to changes in the boundary condition, i.e. injection rate. They go on to explain that these large scale structures are likely due to changes in vorticity production and transport at the nozzle orifice during the deceleration phase. As the injection is reduced, both vorticity at the nozzle and shear in the jet decreases resulting in slower vortex breakdown and longer eddy turnover times. These two effects will result in the larger vortical structures, or indentations, along the jet boundaries. These results are evidence that the dominant fluid-mechanical mechanism of entrainment is large-scale vortical motions, as opposed to small-scale turbulent mixing. The important implication of this finding is that entrainment can be controlled through modification of the boundary conditions. In the context of diesel sprays, this is fortuitous because the injection rate profile can act as a tuning parameter for control of combustion characteristics, i.e. heat release rate, pollutant emissions, etc.

From a simplified view of diesel sprays, Musculus considered an integral transport equation for momentum flux, $\dot{M}$, in the axial direction, x, to understand the effect of nozzle momentum flux at the end of injection on the downstream mixing field [40]. Assuming that the spreading angle is constant and there exists negligible axial pressure gradient, Eq. 14 can demonstrate how temporal changes in the momentum flux at the injector nozzle give way to local changes in the mixing field downstream,

$$\frac{\partial \dot{M}}{\partial t} = -c\frac{\partial \dot{M}}{\partial x}. \tag{14}$$

The wave speed, $c = 2\beta U$, is defined in terms of the mean axial velocity averaged over the jet cross-section, U, and transition parameter, β, that accounts for the velocity profile along the radial direction. During end-of-injection, $\frac{\partial \dot{M}}{\partial t}$ becomes negative since the fueling rate decreases and thus the nozzle momentum flux decreases. Therefore, according to Eq. 14, $\frac{\partial \dot{M}}{\partial x}$ must become locally positive to maintain the assumed constant spreading angle and zero axial pressure gradient. Accordingly, from the continuity equation, the entrainment rate must locally increase given a locally positive $\frac{\partial \dot{M}}{\partial x}$. This region of increased entrainment then travels downstream at a speed specified by c and is referred to as an "entrainment wave" [40, 41].

This entrainment wave is illustrated in Figure 9a, where the entrainment rate relative to a steady jet is shown at several instances in time after the deceleration transient. At t = 0.1 ms after end-of-injection, the peak relative entrainment rate reaches 1.5 at 10 mm downstream of the orifice exit. The entrainment wave can be tracked by locating this peak in time, often referred to as the head of the entrainment wave. The peak relative entrainment rate continues to grow until it reaches an asymptotic value near three. After passage of the enhanced entrainment region, the relative entrainment rate drops below that of a steady jet. The head of the entrainment wave can also be identified with the approximate mixture fraction, shown in Figure 9b, by the departure from the steady jet solution at each instance in time. We can see that the approximate mixture fraction quickly decreases and becomes very fuel lean immediately following the end of injection. From this simplified analysis, rapid end-of-injection causes enhanced entrainment in the near-nozzle region that will produce very lean fuel-air mixtures. Furthermore, we can see that the end-of-injection fueling rate, $\frac{\partial \dot{M}}{\partial t}$, directly controls how fuel lean near-nozzle mixtures become with time after end-of-injection. A major focus of this thesis is the end-of-injection fueling

rate, or ramp-down, and its effects on ignition and UHC/CO formation in near-nozzle mixtures.
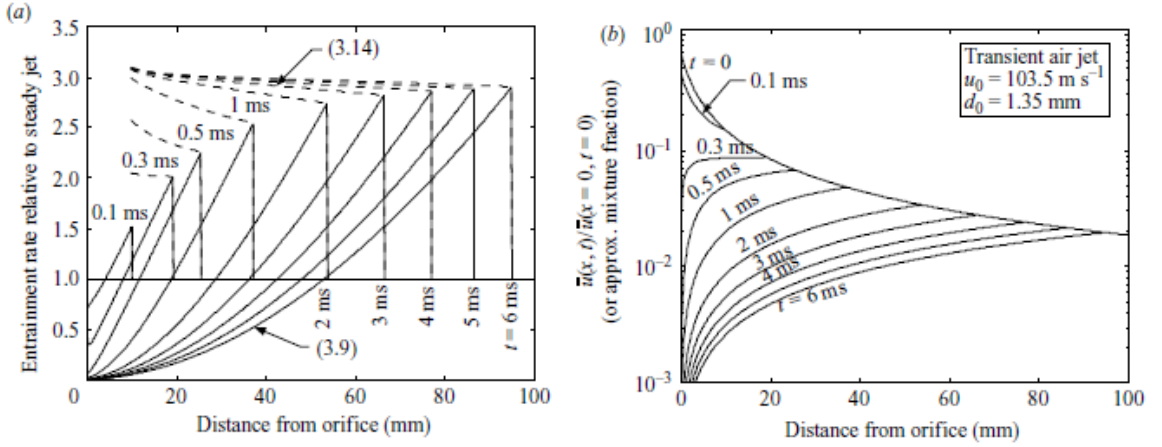
Figure 9: a) Entrainment rate relative to steady jet (solid lines) at various times after the beginning of the deceleration transient; b) Cross-sectionally averaged jet velocity normalized by the jet exit velocity, which is also the approximate mixture fraction [40].

While the above analysis simplified diesel spray physics considerably, it captured the end-of-injection mixing effect that went unnoticed in higher fidelity simulations for years. Singh and Musculus have confirmed the existence of this entrainment wave through 2D simulations of transient gas-jets [42] but found that the width of the enhanced entrainment region and the peak entrainment were wider and lower, respectively, compared to that predicted by Musculus's 1-D model. They attributed the differences between predictions to the exclusion of compressibility and turbulent diffusion in the 1D model. They go on to show that a fast acoustic wave initiates the enhanced entrainment during deceleration but the increase in entrainment is small compared to the slower momentum wave that follows. While the 1D model neglects the acoustic wave, it does capture the momentum wave, where a large majority of the enhanced entrainment is adequately captured. Very recently, experimental verification for the existence of the entrainment wave in diesel sprays was demonstrated by Eagle, Musculus, Malbec, and Bruneaux [43], shown in Figure 10. They used the

entrainment coefficient to show the enhanced entrainment, which is defined in Eq. 15. Here, $d\dot{m}/dx$ and m_o represent the differential entrainment rate and orifice mass flow rate during steady injection, respectively. They also confirm the results from Singh and Musculus in that the entrainment wave is wider and with lower peak entrainment compared to the 1D model. While the exact structure of the entrainment wave, as predicted by the 1D model, is not entirely correct the cumulative effect on local fuel-air ratios is likely very similar to higher fidelity simulations or experiments.

$$C_e = \frac{d\dot{m}}{dx} \frac{d_0 \sqrt{\rho_f/\rho_a}}{\dot{m}_0}. \tag{15}$$
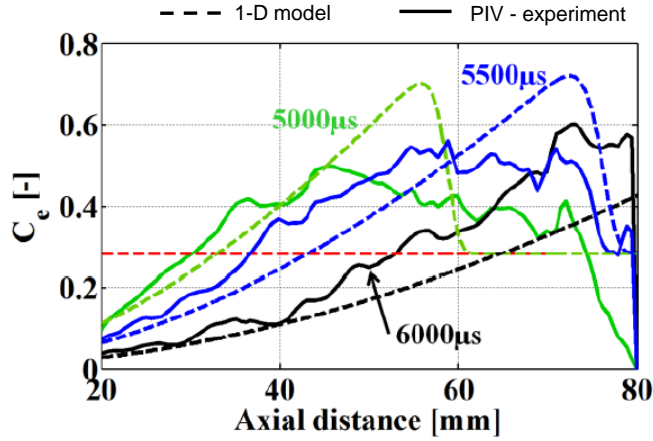
Figure 10: Experimental verification of the entrainment wave concept by Eagle, Musculus, Malbec, and Bruneaux [43].

With regard to combustion and the impact on emissions, end-of-injection processes have seldom been the focus. A few exceptions are Refs. [10, 44, 45] where end-of-injection combustion processes were identified through high-speed measurements of soot luminosity and chemiluminescence, primarily due to better time-resolution compared with low repetition rate laser diagnostics. These measurements can be done with high-speed CMOS cameras, typically operating at tens of kilohertz, that can better resolve the transient evolution of near-nozzle mixtures. Espey and Dec [44] were some of the first to notice that under the conditions of their study, which were at

high ambient temperature and oxygen concentration - typical of HTC, soot luminosity propagated back towards the nozzle after end-of-injection. This phenomenon will be referred to as *soot recession*. Prior to end-of-injection, soot luminosity was limited to downstream portions of the jet, at distances beyond the flame lift-off length. This result suggests that end-of-injection processes bring near-nozzle mixtures towards a condition that supports combustion and even soot formation. Bobba, Genzale and Musculus were the first to systematically study soot recession by varying only the ambient temperature with all other variables held constant. They found that as the ambient temperature was reduced, approaching more LTC conditions, soot recession ceased to exist, which demonstrates that end-of-injection processes can even inhibit soot formation under some conditions [45]. While there was no evidence of near-nozzle soot at these conditions, combustion of near-nozzle mixtures could presumably still exist. However, this was not their focus but the importance of this thought will become apparent in the next section. For the cases that did exhibit soot recession, soot in the near-nozzle region appeared ∼3 crank-angle degrees (400 µs) after end-of-injection and was the first to oxidize. Thus, the evolution of near-nozzle soot appears to be quite transient, suggesting a complex interaction between formation and oxidation that is a direct result of end-of-injection processes.

Motivated by the correlation between UHC and ignition dwell in Figure 8, Musculus, Lachaux, Pickett and Idicheria were the first to focus on second-stage combustion, or lack thereof, in mixtures near the nozzle under LTC conditions, shown in Figure 11 [10]. They used high-speed broadband chemiluminescence imaging for evidence of second-stage combustion reactions. This technique collects light emitted from the combustion process, much like soot luminosity imaging, but is more sensitive to the low levels of light produced by excited radicals during combustion. Similar to the concept of soot recession, evidence of second-stage combustion reactions propagating back towards the nozzle after end-of-injection will be referred to as *combustion*

recession. Combined with fuel-air mixing measurements, they showed that mixtures near the nozzle were very lean; perhaps too lean to support combustion recession. Even though second-stage combustion reactions were not observed under these conditions, first-stage ignition is still very likely. Indeed, as demonstrated by Genzale, Musculus, and Reitz [46], as well as Musculus and Lachaux [47], formaldehyde (an optically accessible indicator of first-stage ignition) was visible throughout the entire cross section of the near-nozzle jet. Since formaldehyde tracks well with UHC, these measurements were evidence that incomplete combustion of near-nozzle mixtures was an important source of UHC emissions for LTC strategies. UHC emissions that result from incomplete combustion of very lean mixtures are often referred to as *lean-source.* Other causes of UHC emissions in engines are often from a *rich-source* and include wall-wetting from excessive liquid penetration, quenching of mixtures near cold walls, and poorly-atomized fuel leaving the nozzle sac and orifice after end-of-injection, often referred to as dribble [48, 49, 50].
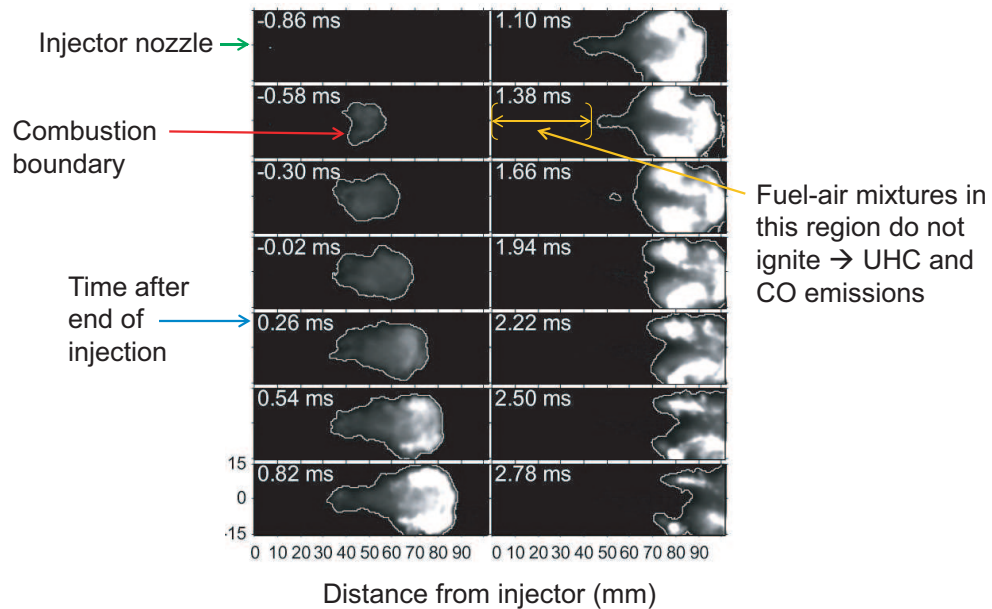
Figure 11: Chemiluminescence images indicating lack of *combustion recession* for LTC operating condition from Musculus, Lachaux, Pickett and Idicheria [10].

1.3 Research Objectives

From the previous section, several unresolved issues remain regarding the coupling of end-of-injection processes and combustion and their link to emissions of UHC/CO and soot. Few studies have focused on end-of-injection in general and even fewer have focused on end-of-injection combustion processes, highlighting a substantial knowledge gap. Measurements have shown that end-of-injection processes create lean mixtures near the nozzle but the coupling to combustion is unknown, that is, the exact operating conditions or injector parameters for which we should expect to observe failure of second-stage ignition (UHC/CO) or excessive soot formation in near-nozzle mixtures is not understood. LTC strategies may indeed be a solution to achieve simultaneous low soot and NOx emissions but their utility is undermined by excessive UHC and CO emissions, which require a sufficient knowledge base to develop innovative methods for their minimization.

A central hypothesis to this thesis is that the problematic near-nozzle UHC/CO emissions at LTC conditions are not merely due to positive ignition dwell but rather a competition between end-of-injection mixing rates and combustion that could also occur for negative ignition dwell conditions. Soot formation in near-nozzle mixtures is also likely due to the same competition. Thus, this work seeks to understand the coupling between end-of-injection mixing time scales and near-nozzle ignition/soot formation time scales by using quasi-steady fuel sprays with a negative ignition dwell. The relationship between timescales will be perturbed by systematically varying the ambient thermodynamic conditions as well as the injection parameters.

Specific objectives to test this hypothesis and address the issues outlined above are provided below:

- Develop a reduced-order model to investigate the impact of end-of-injection transients on combustion recession and lean-source UHC and CO emissions for a wide range of engine thermodynamic conditions and injection parameters.

25

This computationally-inexpensive model will help provide physical insight into the coupling between mixing and chemistry processes that are thought to control combustion recession.

- Design and construct fully-flexible experimental rate-shaping system to perturb the end-of-injection transient and develop a measurement technique to quantify transient injection mass flow rate.

- Evaluate high-speed imaging diagnostics to measure the occurrence and characteristics of combustion and soot recession.

- Systematically develop an experimental database to support validation of reduced-order model predictions. Synthesize experimental and numerical results to create a regime diagram for combustion and soot recession using first-principles.

- Provide physical insight to support the practical application of injection rate-shaping for UHC emissions control under PPCI conditions. Further utilize this insight to provide recommendations for the development of spray and turbulent combustion sub-models that attempt to capture combustion recession computationally.

CHAPTER II

METHODS

Many of the experimental and numerical methods presented in this section have been published in previous works by the author and will be shown here for posterity [51, 52, 53, 54, 55].

2.1 High Pressure-Temperature Vessel

This work was performed in a nominally-quiescent spray chamber without the complications of in-cylinder flows, thus providing a baseline for which combustion recession can be characterized. This facility, shown in Figure 12, is capable of creating a high-pressure (3 bar to 100 bar) and high-temperature (293 K to 950 K) environment in which to optically probe a fuel injection event. The vessel is a two-part design with an outer chamber to hold pressure while the inner chamber is insulated to contain the high temperature gases. High pressure air is fed through the bottom of the vessel and passes through two 15 kW electrical heaters to raise the temperature of the incoming air. Then, the air enters the insulated inner chamber through a diffuser designed to promote temperature uniformity within the test section. Directly beneath the diffuser lies an additional 5 kW heater to further enable temperature uniformity. The injector is mounted in a cooling jacket such that with vessel heating, the injector body temperature can be controlled down to $\sim 80°$ C. Four sets of quartz windows (one set is not visible due to the cut-away and is located along the spray axis) surround the spray providing 100 mm of optical access.

Measurements of the temperature distribution within the high pressure/temperature vessel have been completed to characterize the thermodynamic conditions of the ambient gases in which the spray is injected and to quantify boundary conditions

27
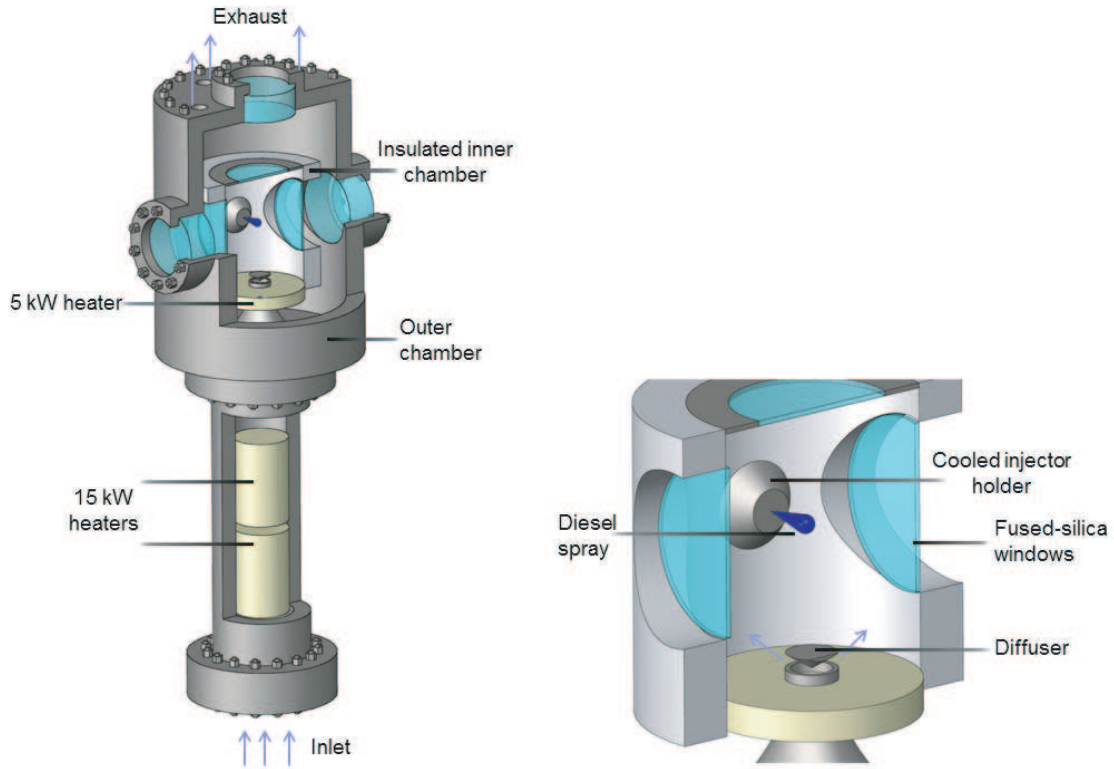
Figure 12: High temperature and pressure optical spray chamber.

for use in the model. Since diesel spray combustion is highly sensitive to ambient temperature, the temperature distribution within the spray chamber is important to keep in consideration for interpretation of the experimental results presented in this work and for future comparisons with modeling results. A non-uniform temperature distribution of the ambient gases occurs in all diesel spray combustion chambers since material temperatures must be maintained below the high ambient gas temperatures to avoid material failure.

To assess the degree of non-uniformity within the chamber, the temperature was measured at 11 locations on the vertical plane that is coincident with the injector axis for a wide range of vessel pressures (40, 60, and 80 bar) and temperatures (700, 800, and 900 K). Exposed junction K-type thermocouples (special limits of error = 0.4% or at most 3.6 K for the conditions in this study) with a bead diameter of 0.5

mm were fed through a multi-element pass-through fitting and positioned at locations shown in Figure 13 (shown as squares). The target temperature and pressure for this measurement was 900 K and 60 bar. The thermocouples were positioned as close as 4 mm from the injector holder wall, which are believed to be outside the thermal boundary layer associated with the vessel wall. At axial locations closer than 4 mm from the vessel wall temperatures as much as 50 K cooler than the target temperature have been observed [56]. Using Spray A PIV results from the ECN database [57], a simple estimate of the time required to entrain gas from a region outside of the spray can be determined. For example, at 10 mm radial distance from the spray axis and 30 mm axial distance from the injector tip, the ambient gas radial velocity is at most -0.5 m/s (inward toward the spray). If we assume that this velocity is relatively constant (which does appear reasonable), the time required to entrain gas from this position is approximately 20 ms. Since 20 ms is quite long relative to an injection event, it is safe to say that the region of influence is most likely much less than 10 mm radial distance surrounding the spray. Based on the temperature measurements and the estimated region of influence, the ambient temperature appears to be within +1% to -1.5% of the target temperature.

During spray combustion experiments, the thermocouple array was replaced by two thermocouples with diameters of 3 mm and 1 mm, located ~40 mm axially and vertically from the injector tip. These two thermocouples were used for radiation-corrected measurements of the target temperature within the chamber. Radiation correction was found to be at most 5 K for the targeted 900 K and 60 bar ambient condition. Conduction error is likely low because much of the sheath near the sensing element is exposed to the hot ambient gases, which should create only a small temperature gradient.

Injector nozzle tip temperatures have also been measured to estimate the temperature of the fuel injected into the vessel using a special injector fitted with a

thermocouple in the nozzle sac. For example, under a nominal vessel pressure and temperature of 60 bar and 900 K, the injector tip temperature was measured to be approximately 84° C.
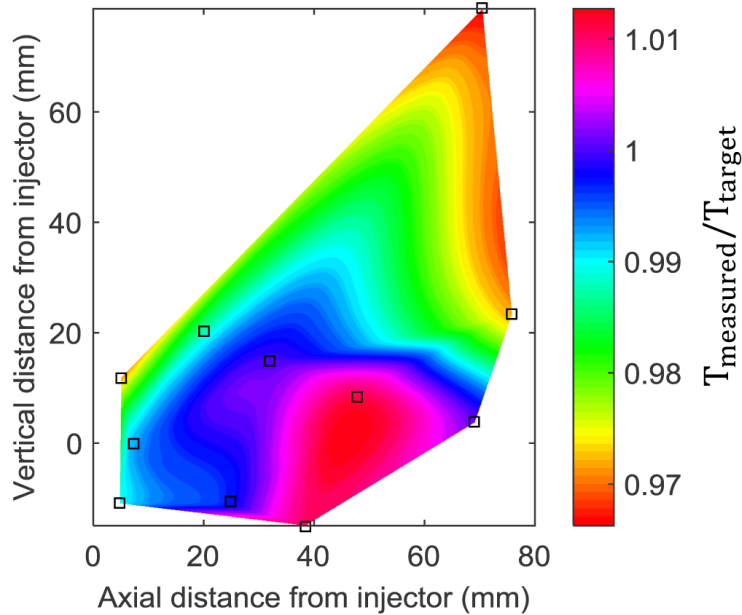
Figure 13: Sample temperature distribution within spray chamber. The target temperature is 900 K and pressure is 60 bar.

2.1.1 Additional Equipment

To probe a wide range of injector operating conditions, such as fuel pressure and type, a custom Maxpro Technologies pnuematically-operated pump is used to provide fuel pressures up to 4100 bar and can handle a range of fuel types, including oxygenated compounds. Time-resolved measurement of fuel pressure near the injector inlet is achieved with a Kistler piezoresistive pressure sensor model 4067A5000 and anti-aliasing, 50 kHz, analog low-pass filter. The fuel pressure measurement was sampled by a National Instruments 9215 16-bit input module at 100 kHz. A cooling jacket that surrounds the injector can be continuously cycled with silicone 180 oil, heated or cooled between −40° C and 200° C externally by a Thermo Scientific Haake A40 heater, to provide consistent fuel temperature, i.e. boundary conditions, between

non-heated and heated vessel experiments. Also, to probe a complete sweep of possible engine conditions, oxygen concentration is varied with an on-demand nitrogen generator and mixing panel to provide high-pressure gases, from 0% to 21% oxygen, to the optically accessible pressure vessel. The nitrogen generator is a pressure swing adsorption type, made by South-Tek Systems, and is capable of producing nitrogen at a rate of 5200 SCFH with a purity down to 500 ppm oxygen (99.95% by volume N2 purity).

2.2 Injection Rate-Shaping System

A significant contribution of this thesis is the development of a fully-flexible injection rate-shaping apparatus, shown in Figure 14, which controls the pressure supplied to the experimental injector by charging or discharging the fuel lines that feed into it. Common rail injectors are used as ultra-high-pressure, fast-acting valves that can operate at pressures up to 200 MPa and fully open/close in approximately 100 μs. Fuel is fed to the common rail by a high-pressure pump, which is then routed to the charging injector. A custom coupling block provides a unique seal for the charging injector to the rest of the system. Fuel can then travel to the experimental injector, discharging injector, or is stopped by a check valve. A low-pressure fuel pump supplies fuel through the check valve when the pressure in the system decreases below a predefined minimum. The pressure supplied to the experimental injector must remain above some minimum in order to prevent air in the high pressure/temperature vessel from escaping back through the injector.

Nearly any injection rate shape desired is possible with this injection system offering a unique opportunity to explore the benefits of injection rate-shaping for combustion/emissions control. A sample control strategy for ramp-down injection rate-shaping is also shown in Figure 14. The charging injector opens well before the experimental injector in order to provide a constant high-pressure volume upstream.
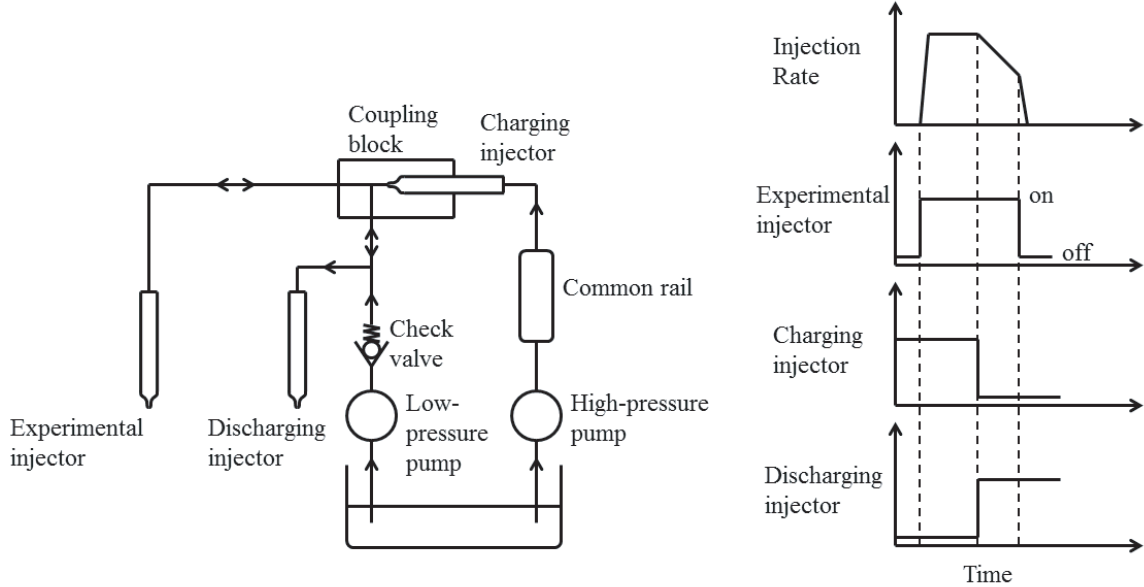
Figure 14: Injection rate-shaping apparatus and control strategy.

Then, the experimental injector is energized in which the injection rate resembles the initial portion of a conventional injection rate shape. Shortly thereafter, the charging injector is de-energized at nearly the same instance as the discharging injector is energized. The fuel pressure that supplies the experimental injector quickly decays as the volume upstream empties.

The charging injector is a commercially-available 7-hole, solenoid-actuated Bosch CRI2.2 with nominal 140 µm diameter holes. The discharging injector is a custom 4-hole, solenoid-actuated Caterpillar CR350 with nominal 374 µm diameter holes. Using control volume analysis, the pressure in the fuel line that feeds the experimental injector is simulated along with the measured value in Figure 15. Also, a custom LabVIEW program simultaneously controls each injector and further data acquisition needs.

2.3 Rate-of-Momentum Measurement

Historically, injection systems have been characterized with an injection discharge rate-curve indicator, e.g. long-tube or Bosch method [58]. These devices measure the
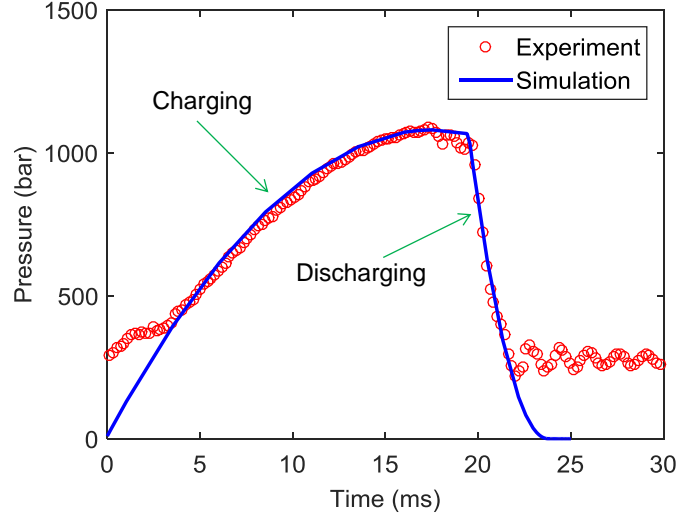
Figure 15: Pressure control capabilities of injection rate-shaping apparatus.

instantaneous mass flow rate of fuel through the injector nozzles, often referred to as the rate of injection. While these measurement devices are commonly used, interpretation of their signals is often difficult. For instance, the long-tube method exhibits large oscillations in the measured signal that have only recently been found to be non-physical, i.e. the oscillations are not a true feature of the instantaneous mass flow rate through the nozzle orifices [59]. These oscillations are the result of injector motion causing acoustic fluctuations within the fluid-filled control volume [59]. The rate-of-momentum is less often measured though its measurement technique is preferable to the long-tube method because it is less susceptible to injector motion (and thus non-physical oscillations) in addition to the fact that more information is available about the injection. Specifically, the rate of momentum measurement enables quantification of the nozzle flow coefficients when coupled with a measurement of the total injected mass. Rate of injection can also be inferred from a rate-of-momentum measurement by assuming that the temporal profiles are similar.

By accurately measuring the rate-of-momentum, and thus rate-of-injection, the rate-shaping potential of the newly developed injection system can be quantified. The rate-of-momentum measurement technique relies on fuel spray impingement, where

33

fuel is sprayed onto the face of a transducer in close proximity to the injector nozzle, depicted in Figure 16. Application of conservation of momentum to the control volume (CV) drawn enables measurement of the instantaneous fuel spray rate-of-momentum at the nozzle orifice exit by simply equating the reaction force (as measured by the transducer) and the fuel spray rate-of-momentum, $\dot{M}_f$.
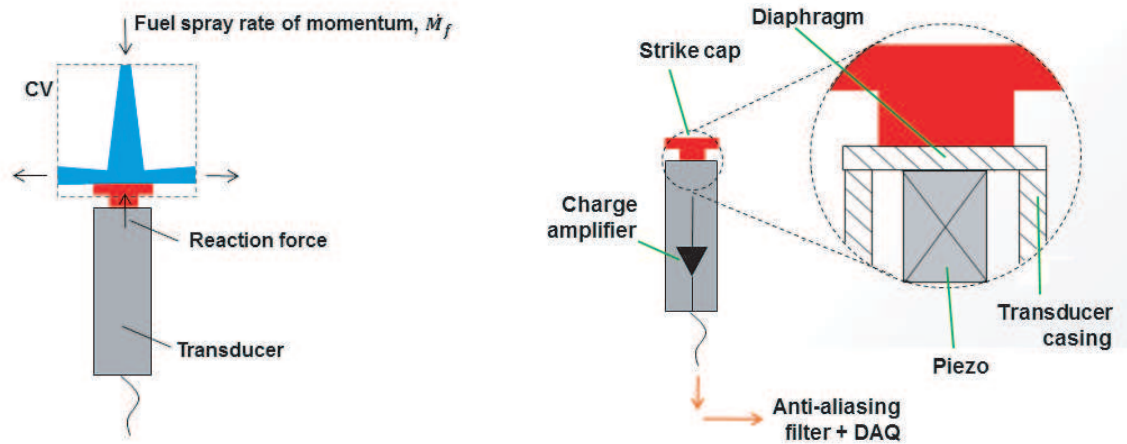
Figure 16: Impingement technique used to measure rate-of-injection/momentum.

Two transducers were used in this study, namely a PCB 113B26 piezoelectric dynamic pressure transducer and a Kistler 9215 piezoelectric force transducer. For the PCB 113B26 sensor, a National Instruments 9234 24-bit analog input module was used for analog-digital conversion and anti-aliasing filtering. A CompactDAQ data acquisition system sampled the signal at 51.2 kHz. For the rate of momentum measurement, the sensor was operated in AC-coupled mode to minimize measurement drift. Additionally, the discharge time constant was estimated to be approximately 50 seconds, ensuring that the signal was not corrupted by charge leakage during the injection. Calibration of the PCB 113B26 pressure sensor to provide force measurements was achieved by DC-coupling the sensor, thus utilizing the NI 9234 module's much longer discharge time constant, and placing NIST calibrated weights statically on the face of the transducer in a vertical position. This process was repeated twenty

times for each NIST calibrated weight. The Kistler 9215 piezoelectric force transducer was coupled with a 5010B charge amplifier, passed through an anti-aliasing filter, and then sampled by a NI 9215 16-bit analog input module at 100 kHz. Since the transducer was already calibrated for force, re-calibration was deemed unnecessary.

In support of the rate-of-injection and nozzle flow coefficient measurements, total injected fuel mass was measured with a collection cup by weighing the difference between the filled and empty cup. The collection cup was designed to minimize fuel mass loss due to vaporization during the transfer of the cup to the mass balance. Using the rate at which the measured mass decreased with time once the collection cup was placed on the mass balance and the time estimated to transfer the collection cup from the injector to the mass balance, the estimated mass loss due to vaporization is approximately 0.07 mg per injection per hole. This estimate was then used for the uncertainty in total injected mass. The mass balance used for this measurement was an Ohaus Adventurer Pro model # AV313.

2.3.1   Design of Experiments for Rate-of-Momentum Measurements

While several researchers have employed the impingement technique to quantify rate-of-momentum [21, 60, 61, 62], questions still surround its use. No study has clearly outlined and estimated the possible sources of uncertainty in the rate of momentum measurement or provided estimates of the relative importance of each uncertainty in the final nozzle flow coefficients. An important subsection of this thesis is to address these issues, enabling higher confidence in the injection rate profiles as well as more wide spread use of the rate of momentum measurement. An outline of the important sources of uncertainty as well as the completed set of experiments is shown in Table 1. The injector used for these studies is a commercially-available 7-hole, solenoid-actuated Bosch CRI2.2 with nominal 140 µm diameter holes and the fuel used is 99.9% chemically pure n-heptane, unless otherwise stated.

Table 1: Rate-of-Momentum Measurements Test Matrix

Effect	Range
Strike cap stem-transducer diameter ratio	95%, 47%, 23%
Angular Misalignment	-20 to 20°
Temperature Sensitivity	35 to 105° C
Transducer Sensitivity	PCB113B26, Kistler9215
Back-Pressure Sensitivity	1, 10, 30, 60 bar

2.4 Back-lit Microscopy

To help assess some of the sources of uncertainty in the rate-of-momentum measurement, high-resolution images of the spray were taken with a back-illumination arrangement. To freeze the motion of the spray, a Light-Speed Technologies white LED (5500 K) was used with a pulse width of 80 ns. A plano-convex condenser lens (f = 85 mm, d = 75 mm) and fresnel lens (f = 254 mm, d = 154 mm) focuses the light to a 10 mm spot size at the injector spray axis. Images of the spray were recorded by a Photron SA-X2 high speed camera with a Questar QM-1 long-range microscope attachment. The projected pixel size for this arrangement was 7.5 µm per pixel. Reference [63] more precisely quantified the spatial resolution of this setup as 72 lines/mm by quantifying the modulation transfer function.

2.5 Combustion Optical Diagnostics

The short time frame in which combustion recession occurs precluded the use of slow repetition-rate laser diagnostics for this thesis. One study, however, has contributed to the understanding of combustion recession by assembling an image sequence of slow repetition-rate formaldehyde planar laser-induced fluorescence from separate injection events [64]. They showed that combustion recession starts with the appearance of formaldehyde (an indicator of first-stage ignition) and is followed by its disappearance (an indicator of second-stage ignition). Further evidence of second-stage ignition was provided by the simultaneous schlieren imaging (an indicator of high-temperature

combustion products). Since some of the details regarding the structure of combustion recession have already been studied, this work utilizes high-speed diagnostics for efficient characterization of the conditions that exhibit the different combustion recession regimes.

Since time-resolving the combustion recession process is a goal of this study, high-speed line-of-sight simultaneous optical diagnostics were performed for each test case; namely OH* chemiluminescence, broadband chemiluminescence/soot luminosity, and schlieren; each of which are shown schematically in Figure 17. Each of the three cameras was positioned to image from the side of the spray chamber. To avoid interference with the schlieren beam, the two other cameras were positioned at a slight angle ($<10°$) off-axis. Correction of these images was achieved through application of a projective transformation matrix, which was found by off-axis imaging a grid of known spacing.

2.5.1   Schlieren imaging

Schlieren imaging relies on collimated light rays that are passed through the measurement volume and refracted by optical inhomogeneities (schliere) along the beam path. These bent rays are then blocked by a so-called schlieren stop such that the collected rays produce an intensity image with the amount of contrast dependent on the refraction angle. Schliere can be detected because they cause gradients of refractive index, where the amount of refraction is dependent on the gas composition, density (and temperature), as well as the wavelength of illumination [65]. Thus, gradients in composition (fuel liquid/vapor at jet boundary) or gradients in temperature (high temperature combustion products) can be detected with schlieren imaging. Schlieren images of diesel spray combustion remain qualitative though due to significant challenges in linking measured refractive index gradients to composition or density gradients.
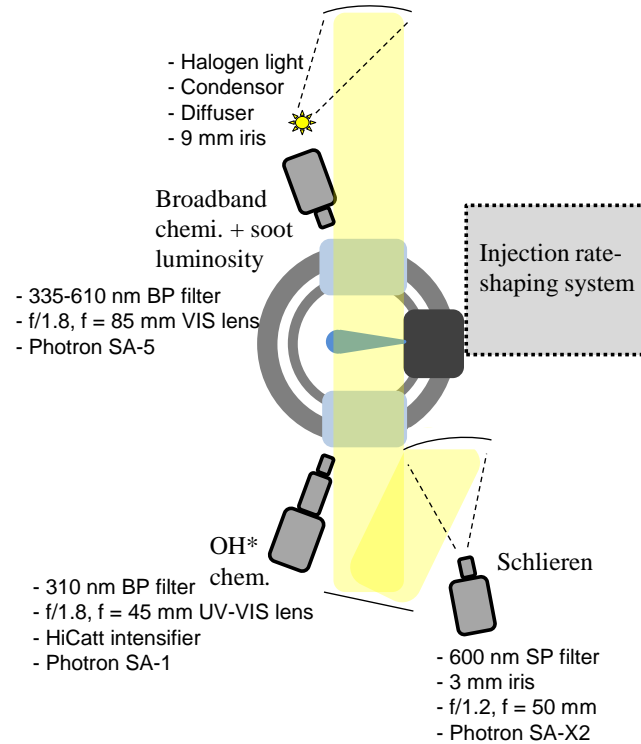
Figure 17: Schematic of optical diagnostics arrangement for measurements of combustion observables.

Because cold liquid/vapor fuel as well as high-temperature combustion products create schliere, interpretation of the schlieren imaging signal requires care. In Figure 18, a sample sequence of an auto-igniting spray demonstrates how discerning schliere is commonly done. By 0.46 ms after start-of-injection (ASI), the fuel spray is seen to penetrate into the high-temperature ambient gases. By 0.56 ms ASI the jet boundary slightly disappears at the head of the jet indicating a change in local refractive index gradients. This change is caused by first-stage ignition reactions that release a small amount of heat to bring local temperatures near that of the ambient gases. Second-stage ignition is then identifiable at 0.72 ms ASI by the reappearance of the jet boundary and local dilatation.

To perform schlieren imaging, the following equipment and settings are used. Illumination is provided by a 150 W tungsten-halogen lamp, where light is passed

Fuel spray + vapor   0.46 ms ASI

1st stage ignition   0.56 ms ASI

2nd stage ignition   0.72 ms ASI

10   20   30   40   50   60   70
Distance from injector (mm)
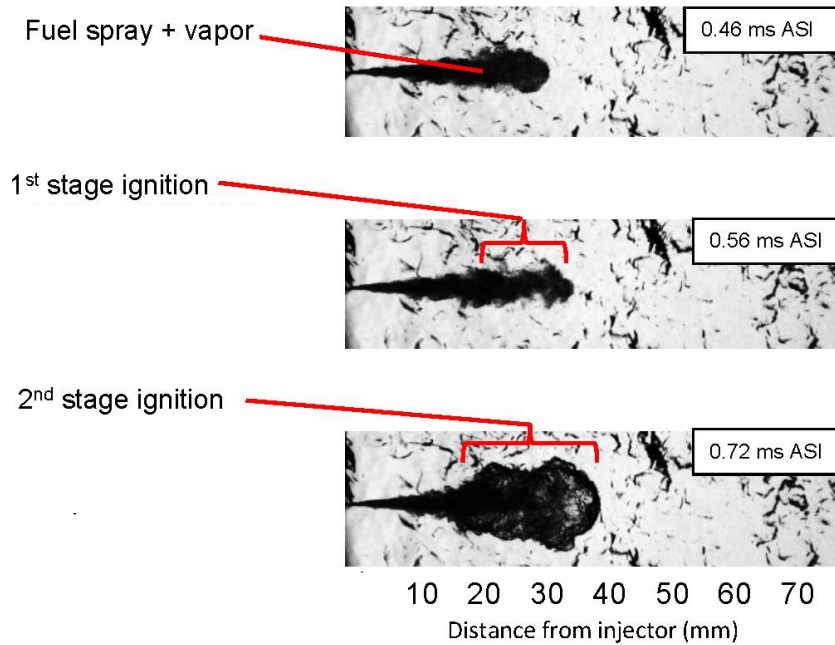
Figure 18: Sample schlieren images to identify first and second stage ignition.

through an f/1 aspheric condenser lens, 600 grit ground glass diffuser, and then a 9 mm iris to emulate an "extended light source". Light is then collimated by an f/8 parabolic mirror, passed through the measurement volume and focused back down by another f/8 parabolic mirror in a typical Z-shaped arrangement. A 3 mm iris is used as the schlieren stop, located at the focal point of the second mirror, to enable adequate schlieren sensitivity. Light is passed through a 600 nm short-pass filter to minimize soot incandescence and then collected by an f/1.2, f = 50 mm Nikkor lens and Photron SA-X2 CMOS camera to provide a projected pixel size of 0.13 mm/pixel.

2.5.2 Chemiluminescence imaging

Complementary to schieren imaging, chemiluminescence imaging was also employed to gather further evidence of ignition reactions. Chemiluminescence is the emission of light from de-excitation of electronically-excited species that are formed via chemical reactions in a combusting flow. Chemiluminescence imaging in both the visible

and ultra-violet range was performed to identify regions of chemical activity, or ignition intermediates. A sample of visible range, or broadband chemiluminescence, is demonstrated in Figure 19.

Broadband chemiluminescence imaging was achieved by collecting light emitted from CH^*, HCO^*, CH_2O^*, CO_2^* and C_2^* (if any). Filtering was performed with a BG40 Schott glass filter (transmission range of 335-610 nm). An f/1.8, f = 85 mm visible lens and Photron SA-5 CMOS camera collected the light without the need for intensification. The projected pixel size for these broadband chemiluminescence images was 0.11 mm/pixel and the framing rate was set to 30 kfps with fully-open shutter duration of 33 µs. Note that soot luminosity is spectrally broad and could have a significant contribution to the overall signal under some conditions even with the employed filter. However, soot is typically discernable by its higher signal compared to chemiluminescence (by orders of magnitude) [66]. Therefore, these images will provide a measurement of chemiluminescence but also a qualitative indication of soot.

Guided by Engine Combustion Network recommendations, the border of second-stage ignition was defined by the intensity count in the broadband chemiluminescence/soot luminosity images such that the threshold is above first-stage ignition and is sufficiently low to capture the boundary (see Figure 19). Note that this sequence is a sample and does not match the conditions in Figure 18. First-stage ignition is evident at t = 0.53 ms after the start of injection, where the maximum intensity count is approximately 15. Prior to this time instance, the maximum intensity count was ~1-2. By 0.63 ms, second-stage ignition is evident where the maximum intensity count is ~500. Based on these findings, the boundary for second-stage ignition was chosen to be 30 counts. Note that images were captured with 12-bit resolution, or 4096 counts full scale.
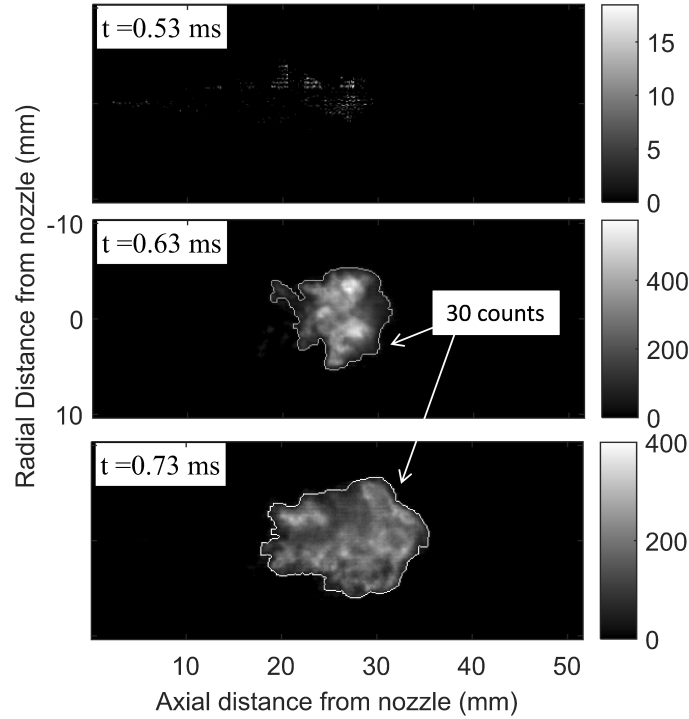
Figure 19: Sample time sequence of broadband chemiluminescence showing progression from first to second-stage ignition and the measured intensity of each.

OH* chemiluminescence and CO_2* (if any) was filtered through a narrow bandpass interference filter centered at 310 nm and then collected by an f/1.8, f = 45 mm UV-VIS lens coupled to a HiCatt 25 image intensifier and Photron SA-1 CMOS camera. The projected pixel size for these OH* chemiluminescence images was 0.14 mm/pixel and the framing rate was set to 30 kfps. Images were captured with intensifier exposure duration and voltage of 5 µs and 700 V. To ensure that regions of chemiluminescence were correctly identified, the boundary of OH* chemiluminescence was set sufficiently low but above the background.

The stabilized lifted flame position, often referred to as the flame lift-off length, was measured with the OH* chemiluminescence technique. For each injection, OH* chemiluminescence images were averaged over the steady portion of injection to provide a time-averaged representation of the lifted spray flame (see Figure 20). To measure the flame lift-off length, we start by identifying two intensity lobes on either

side of spray axis. Then, the intensity profile along the axial distance for each lobe (shown as magenta lines) is measured. The average of these two curves for a range of conditions is shown in Figure 20. To ensure proper comparison with other researchers, this thesis has adopted the Engine Combustion Network definition for flame lift-off length [57]. The flame lift-off length is identified at the 50% threshold of the first peak (show as circles) in Figure 20.
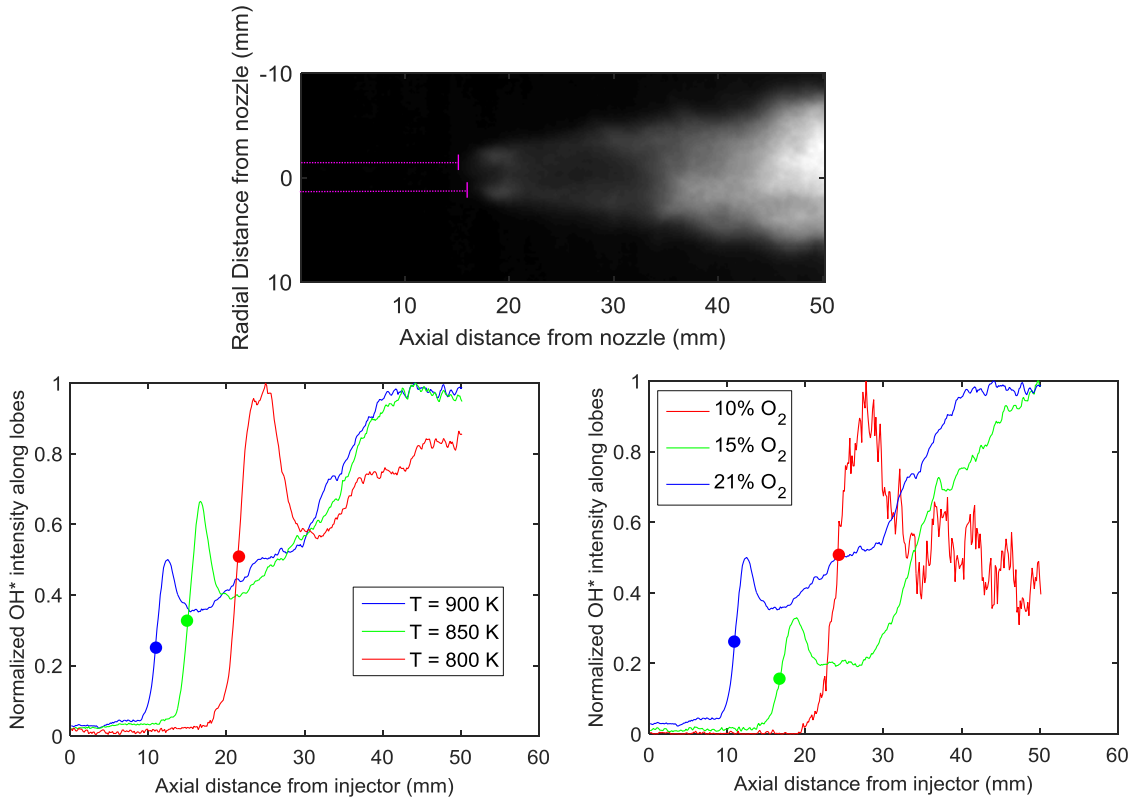
Figure 20: Illustration of lift-off length determination with OH* chemiluminescence technique. Circles indicate the threshold used for lift-off length - values set to 50% of the first peak.

2.5.3 Design of Experiments for Combustion Optical Measurements

This thesis seeks to understand the coupling between end-of-injection entrainment and incomplete combustion of near-nozzle mixtures by systematically varying the ambient thermodynamic conditions, injection parameters, as well as the end-of-injection transient. To do so, a full factorial two-level design of experiments (shown in Table 2) was

performed for six factors; nozzle orifice diameter, ambient temperature, ambient density, ambient oxygen concentration, injection pressure, and ramp-down profile. Both of the injectors (one for each nozzle diameter) are part of the Engine Combustion Network [57] and provided by Bosch. Each common rail injector is solenoid-actuated and features a single, hydro-ground, axially-drilled hole with k-factor = 1.5. The smaller of the two nozzles (90 µm) is from the Spray A injector set (injector #211020) while the larger (186 µm) is part of the Spray D set (injector #209133). While a fractional factorial or other reduced design of experiments could have been performed, a full factorial design of experiments ensures that no higher order interactions are confounded with any main effects. For example, the combined effect of ambient temperature and density is not confounded with the effect of nozzle diameter, or ramp-down profile, or any other main effect. Furthermore, only two nozzle diameters and two ramp-down profiles were available for this study, which precludes response surface methodologies or adding center points to the design. Thus, testing for curvature in the regression (shown later) was not possible. Efforts were made to collect data at 800 K and $7.8\,\mathrm{kg\,m^{-3}}$ but these conditions were simply not reactive enough to simulate a free combusting diesel spray in the spray chamber. For the few trials performed at these conditions, no evidence of combustion recession was observed. Therefore, to complete the full factorial design of experiments, the combustion recession metric, R (introduced in a later section), is assumed to be equivalently zero for all cases with both 800 K and $7.8\,\mathrm{kg\,m^{-3}}$. Other conditions in Table 2, particularly at 850 K, are included for additional validation of the proposed scaling (also shown later) but not in the regression. Lastly, six repeated injections were performed for each condition except for select cases.

Table 2: Combustion Optical Measurements Test Matrix

Nozzle Diameter, d_0 (µm)	90			186		
Ambient Temperature, $T_a(K)$	800	850	900	800	850	900
Ambient Density, ρ_a $(\mathrm{kg\,m^{-3}})$	7.8, 22.8	22.8	7.8, 14.8, 22.8	7.8, 22.8	14.8	7.8, 22.8
Ambient Oxygen, O_2 (%)	10, 15, 21	15, 21	10, 15, 21	10, 21		
Injection Pressure, P_{inj} (bar)	500, 1000					
Ramp-Down Profile, RD	fast, slow					

2.6 Soot Extinction Measurement

To complement the qualitative soot luminosity imaging, quantitative point-based laser soot extinction measurements were performed. The experimental setup for these measurements is depicted in Figure 21. A similar setup has been utilized by Musculus and Pickett [67] and many of their recommendations have been employed in this thesis to minimize the unwanted effects of beam steering. A 10 mW 0.7 mm diameter HeNe laser, centered at 633 nm, passes through the spray flame and is focused with a f=125 mm plano-convex lens through the divergence aperture and then into the integrating sphere. The plano-convex lens was sized (d = 50.8 mm) to capture the entire beam under conditions with the highest index of refraction gradients, or where beam steering effects are most severe. The divergence aperture controls the amount of light collected and a balance is sought to minimize combustion luminosity with a small aperture while not clipping any steered beams. More on this topic will be discussed later. The integrating sphere collects the light and acts as a diffuser, removing much

of the beam orientation information as the light leaves through the exit aperture. The narrow band-pass filter, used to reject much of the combustion luminosity, was placed on the exit side of the integrating sphere because of potential spatial non-uniformities such that the transmitted light could be sensitive to the relative position of the incident light on the filter. The filter was also placed in between two identical f = 50 mm plano-convex lenses such that angle-tuning effects were minimized. Essentially, the first lens is positioned at its focal length away from the exit aperture to minimize the angle of incident light with respect to the filter. The second lens then focuses the light back down to the photodiode entrance. The HeNe laser and light collection optics are each mounted on separate traverses, which are synchronized to maintain alignment and allow for measurements at many locations throughout the chamber.
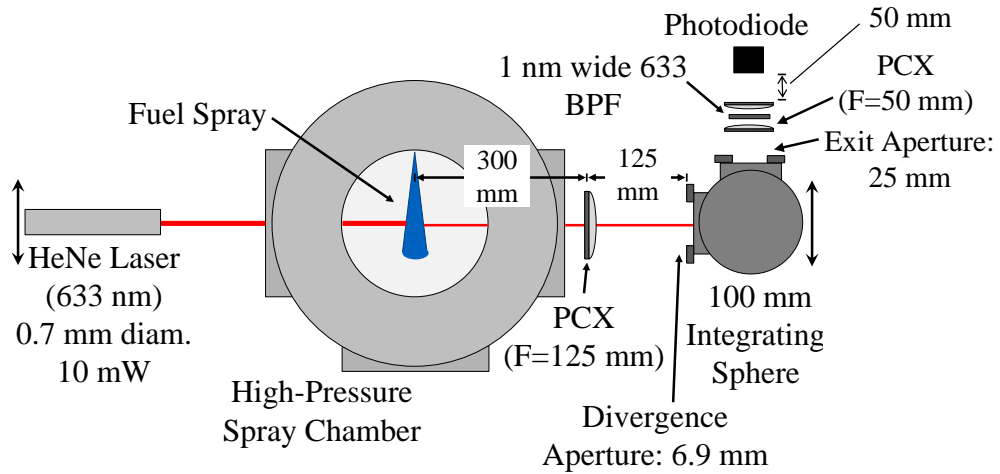
Figure 21: Laser soot extinction measurement setup.

To understand the effect of beam steering and its sources, the beam was projected onto a screen placed 1.2 m away from the centerline of the spray and imaged with a high-speed camera. Two images are shown in Figure 22, where the left image was taken prior to injection, but the beam still passes through the high-temperature and pressure gases within the chamber, and the right image was taken during injection

in a region where significant index of refraction gradients were expected due to combustion. Even in the case of the beam passing through the vessel without injection, index of refraction gradients from boundary layers along the vessel windows and inhomogeneities of the gases within cause the beam to diverge. Using a threshold of 1% of the maximum intensity to define the boundary of the beam, the divergence angle for this case was estimated to be at most 3 mrad. For the case where the beam passes through a combusting region, and experiences significant index of refraction gradients, the beam diverges much more - approximately 24 mrad. To avoid clipping any steered beams, the collection angle must be greater than this, which will be discussed in the next section.
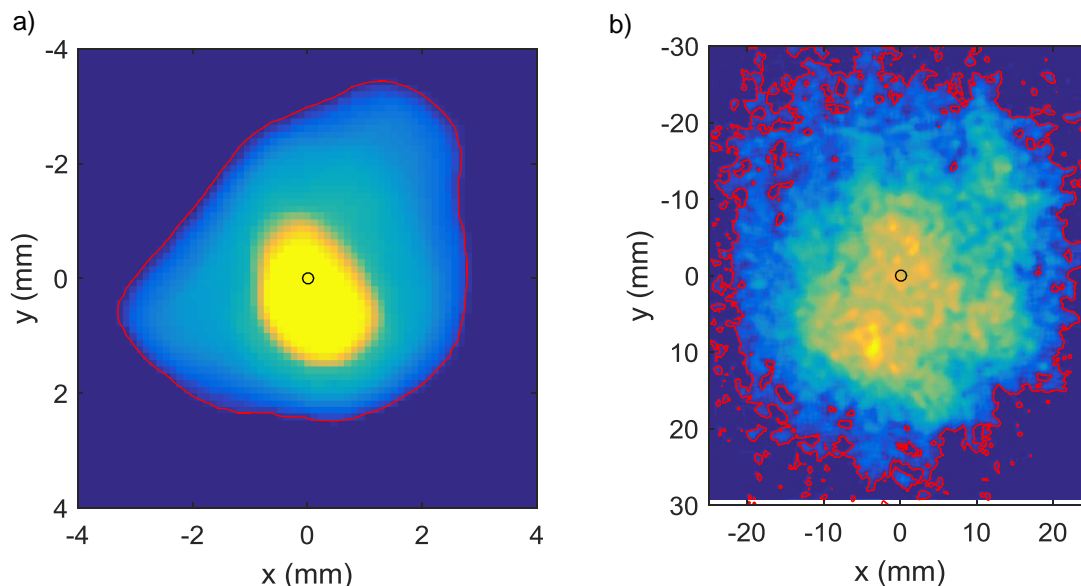
Figure 22: Beam size 1.2 m away from spray centerline a) before injection but during heated and pressurized vessel conditions b) during combustion.

To minimize combustion luminosity while avoiding clipped beams, the divergence aperture, d_{ap} was varied to determine the minimum required collection angle, θ_{col}. Shown in Figure 23 is the apparent soot optical thickness, KL, versus time for various apertures. Equation 16 demonstrates how KL is found from the Beer-Lambert law,

$$KL = -ln\left(\frac{I}{I_0}\right), \tag{16}$$

where I and I_0 are the signal and reference signal intensities, respectively. Conditions for this study were selected to produce soot-free combusting conditions such that any apparent extinction is due to clipping of the steered beams. The conditions are as follows: $T_a = 900$ K, $\rho_a = 22.8$ kg m^{-3}, $P_{inj} = 1500$ bar, $O_2 = 8\%$, $d_0 = 90\,\mu$m. From Figure 23, as the divergence aperture increases the apparent extinction decreases until it reaches nominally zero at 0.27" diameter (collection angle = 55 mrad). Since the combustion at these particular conditions produced very little light, KL was not corrupted. What little light was produced was largely rejected by the narrow band-pass filter. Under conditions of higher luminosity, light emitted from the combustion process is not entirely rejected indicating the need for a correction procedure, which will be outlined below.
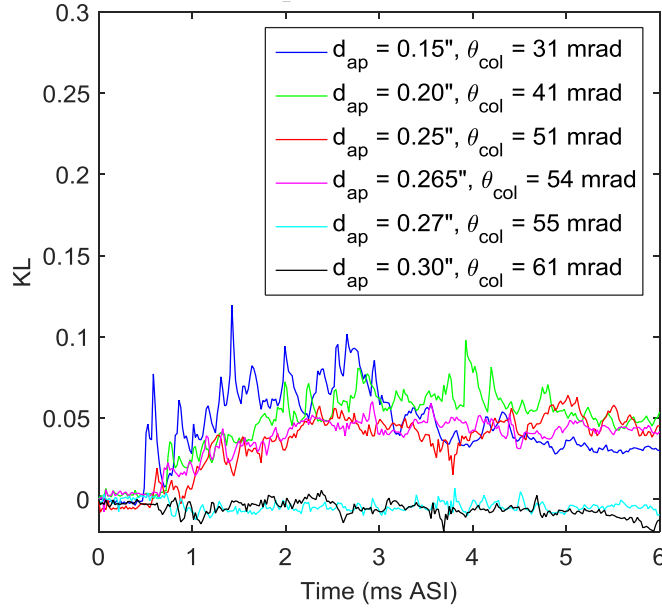
Figure 23: Variation of divergence aperture, d_{ap}, and collection angle, θ_{col}, to test the effect of beam steering on collected signal.

At conditions where soot is expected, a sample raw photodiode signal is shown at the top of Figure 24. At 1 ms ASI the signal begins to increase slightly, which is

47

due to incomplete rejection of combustion luminosity by the narrow band-pass filter. This incomplete rejection is shown in the middle of Figure 24 where the laser has been turned off. Several different injections are shown in various colors with the mean shown as blue and wider line width. By subtracting the mean of these laser-off combustion luminosity traces, a "corrected signal" can be obtained, shown in the bottom of Figure 24. This correction procedure effectively cancels out the biased signal from combustion luminosity. Without this procedure, KL would be severely underestimated.
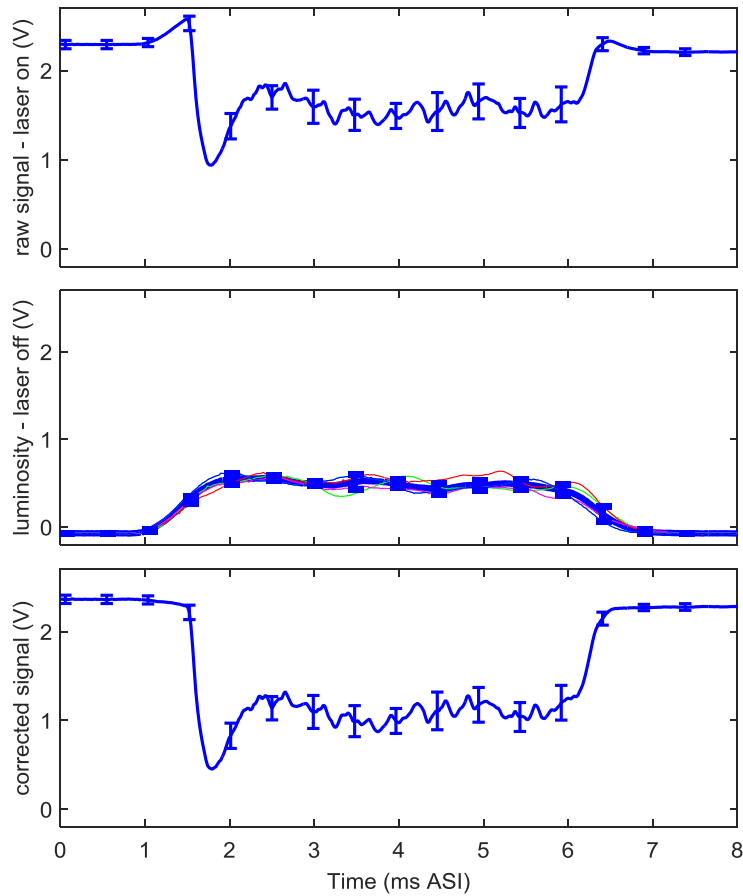
Figure 24: Combustion luminosity correction procedure for laser soot extinction measurements.

48

2.7 Reduced-Order Modeling

Some researchers have shown that straightforward links between fuel injection bound-ary conditions and combustion or performance outcomes can be found through the use of simplified models premised on the similarity between dense turbulent gaseous jets and diesel-like sprays at high ambient gas densities typical of realistic engine operating conditions [21, 41, 68, 69]. Such simplified modeling methods are attractive because they enable engine designers to explore and understand large-scale spray combustion characteristics, over wide ranges of engine operating conditions, at low computational costs. Though a range of simplified modeling approaches for diesel spray combustion have been proposed, with varying levels of chemical kinetics, existing models have focused primarily on steady-state reacting conditions, and lack the ability to link combustion and emissions outcomes to injector transients. Therefore, this thesis aims at providing a new reduced-order model that relates transient events in nozzle boundary conditions (i.e. fuel injection rate) to mixing, coupled with detailed chemical kinetics, to explore the effect of advanced diesel injection strategies on ignition and emissions.

This reduced-order model is based on the mixing model of Musculus and Kattke [41]. The Musculus-Kattke model [41] is used to find the locally transient ambient entrainment within the jet; then, at each distance from the injector orifice, the effects of the transient ambient entrainment on combustion are realized by solving energy and species balance equations. Figure 25 graphically depicts the numerical model, where each control volume, n, is a cell within the discretized space. Inputs to the model are the orifice diameter, d_0, fuel injection pressure, P_{inj}, fuel temperature, T_f, fuel density, ρ_f, nozzle flow coefficients (discharge, C_d, and area contraction coefficient, C_a), ambient conditions (temperature, T_a, species mass fractions, $Y_{i,a}$, and pressure, P_a), and full spreading angle θ. The nozzle boundary condition during the quasi-steady injection period is the Bernoulli velocity modified by the velocity coefficient,

assuming that the nozzle flow coefficients are constant throughout the injection event. To model the beginning and end of injection, a linear velocity change during ramp up and down is specified, unless otherwise stated.

Transients in the spreading angle of diesel sprays are observed to occur during needle opening and closing [70] and also under cavitating flow conditions [71]. Though such transients cannot be captured by the current model, it is not expected that these transients will play a significant role in the fuel-ambient mixing of the conditions explored in the current work. In the presented work, needle opening and closing times are extremely short relative to the main injection period, minimizing the effects of these transients on the cumulative fuel-ambient mixing process.
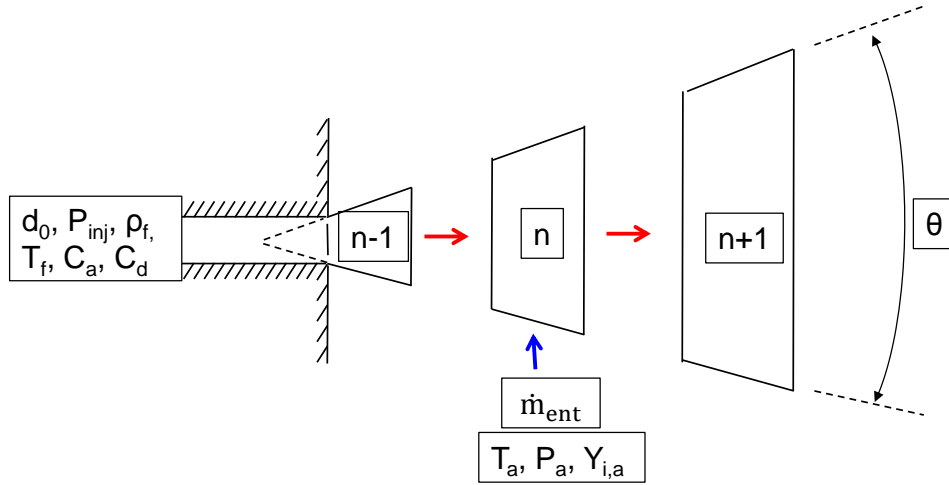
Figure 25: Schematic of 1-D numerical model of diesel jet.

In presenting the equations for solving the numerical model below, the Musculus-Kattke jet-mixing model equations (Eqs.17-24) are shown for completeness. The Musculus-Kattke model [41] considers the spatial and temporal distribution of liquid fuel volume fraction, X_f, by solving the finite volume form of liquid fuel mass, m_f, conservation in Eqs. 17 and 18. The variables ρ, V, A, U, and t are jet cross-sectionally averaged density, jet volume, jet cross-sectional area, jet cross-sectionally

50

averaged velocity, and time respectively, where the subscript f denotes fuel. Discretization, using a simple upwind approach, is then presented where $t-1$ and $n-1$ represent the previous time step and cell while t and n represent the current time and cell. The spatial grid size dx was selected to be 1 mm while the time step dt was determined from the Courant-Friedrichs-Lewy (CFL) condition ($CFL = 0.2$) where a is the fastest velocity within the domain, $dt = CFLdx/a$. This formulation is under the assumption of incompressible flow. Since the axial velocity scales inversely with axial distance from the injector, this assumption is likely poor very near the orifice exit during injection, where jet velocities can reach $\sim$600 m/s at typical diesel injection pressures, but becomes more reasonable further away and after end of injection.

$$\frac{\partial}{\partial t} \iiint \rho_f X_f dV + \iint \rho_f X_f (\vec{U} \cdot \vec{n}) dA = 0 \tag{17}$$

$$m_{f_n}^t = \rho_f X_f V_n^{t-1} + \rho_f X_f (U A_{n-1}^{t-1} - U A_n^{t-1}) dt \tag{18}$$

Jet momentum, M, is calculated under the assumption of no body forces or external surface forces, F_{ext}, acting on the control volume in Eqs. 19 and 20. Buoyancy is neglected since diesel sprays are momentum driven. Shearing forces are also neglected because downstream of the near-nozzle region, or more appropriately potential core, velocity gradients at the jet edges are small. While velocity gradients at the jet edges in the near-nozzle region will be very high due to the nearly uniform velocity profile, the near-nozzle region is expected to be very short and have minimal impact on the results. Also, no axial pressure gradient is considered in the model. Estimation of the pressure drop relative to the ambient gases was found to be at most 7% [40]. Since axial mixing and finite acceleration/deceleration of the jet source will tend to redistribute entrainment over a wider region, estimation of the pressure drop is then reduced to 3% [40]; therefore, neglect of an axial pressure gradient is considered reasonable.

$$\frac{\partial}{\partial t} \iiint \rho U \, dV + \iint \rho U (\vec{U} \cdot \vec{n}) dA = \sum F_{ext} \tag{19}$$

$$M_n^t = \rho U V_n^{t-1} + (\rho U^2 A_{n-1}^{t-1} - \rho U^2 A_n^{t-1}) dt \tag{20}$$

Fuel volume fraction, cross-sectionally averaged density, and cross-sectionally averaged velocity are then found at the current cell and current time step using Eqs. 21-23, where the subscript a denotes the ambient.

$$X_f = \frac{m_f}{\rho_f V} \tag{21}$$

$$\rho = \rho_f X_f + \rho_a (1 - X_f) \tag{22}$$

$$U = \frac{M}{\rho V} \tag{23}$$

The foregoing equations are used to find the transient ambient entrainment, $\dot{m}_{ent}$, in Eq. 24.

$$\dot{m}_{ent} = \rho_a (U A_n^t - U A_{n-1}^t) \tag{24}$$

Here, a new approach for linking the transient ambient entrainment to combustion is presented, which solves conservation of species and energy with the transient ambient entrainment included in the advection terms. The finite volume form and the discretization of conservation of species mass fraction, Y_i, is given in Eqs. 25 and 26.

$$\frac{\partial}{\partial t} \iiint \rho Y_i \, dV + \iint \rho Y_i (\vec{U} \cdot \vec{n}) dA = 0 \tag{25}$$

$$Y_{in}^t = (\rho Y_i V_n^{t-1} + (\rho U Y_i A_{n-1}^{t-1} - \rho U Y_i A_n^{t-1}$$
$$+ \dot{m}_{ent} Y_{ia}) dt) / \rho V_n^t \tag{26}$$

Conservation of energy (enthalpy, h) in its finite volume and discretized form is shown in Eqs. 27 and 28 under the assumption of negligible radiation. In the absence

of a soot model, radiation is considered unimportant for demonstrating the influence of transient mixing on combustion.

$$\frac{\partial}{\partial t} \iiint \rho h dV + \iint \rho h (\vec{U} \cdot \vec{n}) dA = 0 \tag{27}$$

$$h_n^t = (\rho h V_n^{t-1} + (\rho U h A_{n-1}^{t-1} - \rho U h A_n^{t-1}$$
$$+ \dot{m}_{ent} h_a) dt) / \rho V_n^t \tag{28}$$

Once the current cell's species and enthalpy are determined, the mixture is placed into a constant pressure homogenous batch reactor (i.e. no turbulent combustion model is employed) and allowed to react for the duration of the residence time. Large-eddy simulation results from Hu et al. have shown that scalar dissipation rates generally decrease after end-of-injection [39] suggesting that turbulence-chemistry interaction may be of low importance for ignition in near-nozzle mixtures after end-of-injection. The residence time is equal to the time step used in calculating the aforementioned properties. Since chemical reactions occur on a time scale much faster than that of the flow, a stiff equation solver is used to evaluate the kinetics. After the cell has been allowed to react, its contents are then updated to reflect the new enthalpy and species concentrations. Cantera, an open source software, is used for evaluating the thermodynamic properties as well as chemical kinetic rates [72].

Since the fluid mechanics are simplified, computational resources are reserved for large chemical mechanisms with hundreds of species and thousands of reactions. The capability to handle any chemical mechanism regardless of size and still capture the dynamics of a jet reasonably well is valuable for the following reasons. First, comprehensive or detailed chemical mechanisms are more widely available for chemicals like normal alkanes larger than heptane, certain methyl esters, in addition to important sub-mechanisms like polycyclic aromatic hydrocarbon growth [73, 74]. Second, a more comprehensive chemical mechanism is likely to outperform reduced mechanisms

for capturing cool flame behavior and matching experimental measurements of ignition delay, especially at low oxygen concentrations [75]. Indeed, while highly reduced mechanisms often perform reasonably well under a small equivalence ratio range with skilled tuning [76], diesel combustion can be highly heterogeneous, thus reducing the ability of a reduced mechanism to provide reasonable results under different operating regimes.

There are several important differences between this model and other reduced-order models in the literature. First, this model neglects the radial profile of velocity and fuel volume fraction applied in the Musculus-Kattke model and uses only cross-sectionally averaged quantities, much like the Two-Stage-Lagrangian (TSL) model [68]. In contrast to the TSL model, this model assumes that transient ambient entrainment is not affected by combustion. This thesis is focused on whether or not near-nozzle mixtures ignite and is less concerned with the evolution of these mixtures after ignition. It is likely that entrainment is only affected once ignition has already begun where heat release rates are high. However, first-stage ignition (cool flame) does release heat, albeit a small amount, and may have an impact on entrainment during this period. Its potential impact can be evaluated by estimating the entrainment reduction factor, $(T_{burned}/T_{unburned})^{0.5}$, proposed by Han and Mungal [77]. If we consider a stoichiometric mixture of adiabatically-mixed n-dodecane at 363 K and ambient air at 900 K, the resulting temperature is 823 K. Using Cantera, the temperature is found to be 891 K immediately after first-stage ignition. The resulting entrainment reduction factor is $(891K/823K)^{0.5} = 1.04$, or 4% error due to neglect of cool flame heat release on entrainment although the error is likely to grow for mixtures that ignite more fuel rich since the cool flame heat release and resulting temperatures are greater.

54

It is worthwhile to note that while the predicted entrainment physics of this reduced order model may be simplified, the net entrainment of ambient gases predicted by this approach is similar to predictions using higher-fidelity fluid mechanics approaches. To evaluate potential differences in predicted entrainment by the Musculus-Kattke model, Singh and Musculus studied single-pulsed transient round gas jets using the full compressible, unsteady Navier-Stokes equations on a 2D axisymmetric mesh [42]. The 2D CFD model predicted a wider axial region of increased entrainment, with a lower peak entrainment rate, compared to the Musculus-Kattke model. They attributed the differences between predictions to the exclusion of compressibility and turbulent diffusion in the 1D model. Measurements of entrainment in a real diesel spray confirm the results from Singh and Musculus in that the entrainment wave is wider and with lower peak entrainment compared to the 1D model. While the exact structure of the entrainment wave, as predicted by the 1D model, is not entirely correct the cumulative effect on local fuel-air ratios is likely very similar to higher fidelity simulations or experiments.

Because reduced-order models of this type [68, 78] are unable to capture all of the physics that drive flame lift-off stabilization, flame lift-off length is made an input to the model. Without this input, the 1-D model would over-predict the flame lift-off length because it does not account for recirculation of hot combustion products back into the stabilization location, in addition to other flame stabilization mechanisms. Capturing flame lift-off length is an important precursor for accurate predictions of unburned hydrocarbons (UHC) because the UHC emissions potential could scale by as much as $FLOL^2$. This estimate comes from the fact that the total mass of fuel in the jet scales as x^2 and the simplification that the entrainment wave is infinitely fast, bringing the entire jet to a rest, and thus no unreacted mixtures are convected into the reaction zone. Note that forcing the flame lift-off length does not affect ignition chemistry from occurring upstream of the flame lift-off length nor does it influence

55

the outcome of combustion recession in any way.
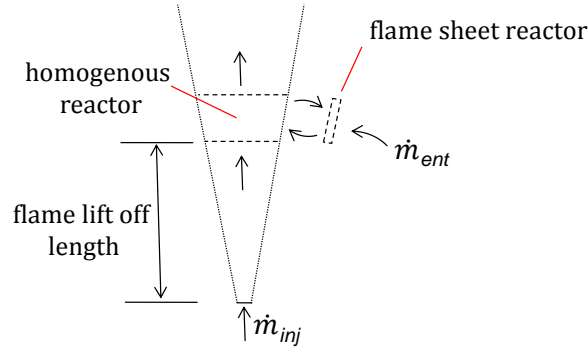
Figure 26: Schematic of flame lift-off input to model.

A schematic of the flame lift-off input is shown in Figure 26, where flame sheet reactors surround the core of the jet - a series of homogeneous reactors. A portion of the core fluid mixes with the entrained ambient gases to create stoichiometric conditions inside the flame sheet reactor. After the mixture in the flame sheet reactor undergoes equilibrium calculations at constant pressure, it is then combined with the core fluid and allowed to react for the duration of its residence time, as was explained previously. The flame sheet reactors are "turned on" only after the ignition delay, as predicted by the model. Note that after end-of-injection, the flame lift-off length input does not change because there is no reason to expect that the flame sheet reactor should move. The flame sheet reactor is meant to model a diffusion flame, which has no mechanism for propagation. Therefore, any combustion in the model upstream of the flame lift-off length input is due to autoignition of these mixtures.

CHAPTER III

VALIDATION OF METHODS

Many of the experimental and numerical validation results presented in this section have been published in previous works by the author and will be shown here for posterity [52, 55].

3.1   Mixing Model Validation (Non-Reacting)

For completeness, the mixing model presented by Musculus and Kattke (from which the joint mixing-chemistry model is based) is validated against a wide range of experimental data from the same institution. Because the joint mixing-chemistry model employs a radially-averaged approach, the spreading angle input will differ from the values presented by Pickett and coworkers in Ref. [79]. Table 3 contains the spreading angle input for each condition along with other important parameters. Validation of the mixing model will be achieved through comparison of vapor penetration, a common spray metric, for parametric variations about the Spray A condition [57] followed by a time sequence of quantitative mixing measurements of vapor fuel concentration for the Spray H condition [57].

Spray A vapor penetration was measured with high-speed focused shadowgraph imaging at Sandia National Laboratories [79]. The reported uncertainty, shown as red error bars in Figure 27, is based on scatter in the data due to the variation between separate injection events. For model comparisons to the experiment, the model definition for vapor penetration is the axial distance where the mixture fraction drops below a threshold value of 0.001, as recommended by the Engine Combustion Network [57]. Following the recommendations of Pickett et al. [79], the modeled jet spreading angle was selectively reduced in order for the predicted vapor penetration

57

Table 3: Model Inputs for Spray A Vapor Penetration Validation

Parameter	Value	Full spreading angle θ (deg.)
Ambient density ρ_a (kg m^{-3})	7.6	16.17
	15.2	16.54
	22.8	16.91
Injection pressure P_{inj} (bar)	1500	16.91
	1000	16.91
	500	16.91
Orifice diameter d_0 (µm)	90	
Discharge coefficient C_d	0.86	
Area contraction coefficient C_a	0.95	
Start of injection ramp duration (µs)	50	
Fuel temperature T_f (K)	363	
Fuel density ρ_f (kg m^{-3})	699	
Injection duration (ms)	6	

to match that of the experiment. Musculus [57] has also recommended this approach, arguing that the modification of the spreading angle may be considered a correction factor to account for the assumption of a uniform velocity profile across the jet cross-section.

By matching the measured vapor penetration, the model demonstrates that the physics of momentum exchange between the fuel jet and surrounding ambient gases are well captured. Thus, the residence time of reactive mixtures is expected to be closely matched to a real diesel jet. Also, since the local equivalence ratio is determined by entrainment of ambient gases into the jet, and follows from the ambient-gas jet momentum exchange, local equivalence ratios are also expected to be matched to those of a real diesel jet.

Figure 28 demonstrates agreement with this assessment, comparing cross-sectionally averaged experimental [79] and simulated mixture fraction for spray H, at four times after the start of injection. The Spray H nozzle is slightly different from the Spray
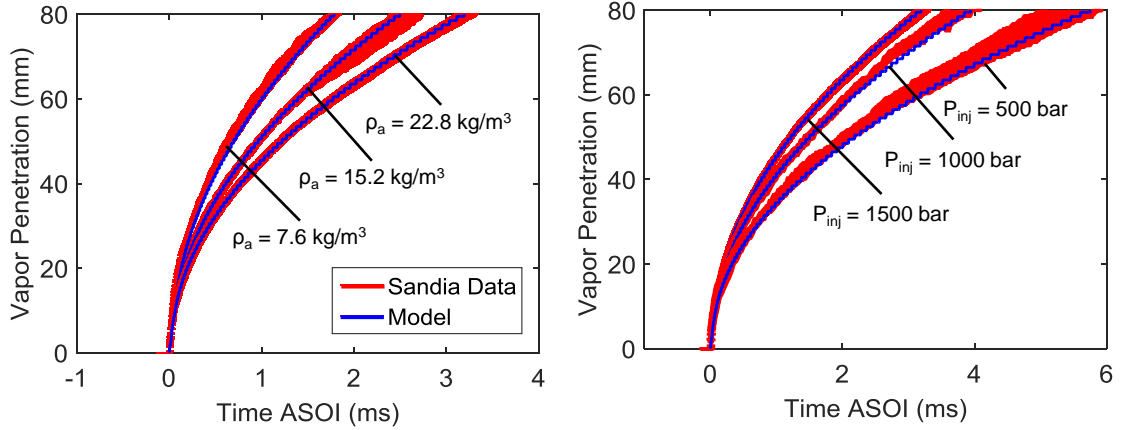
Figure 27: Non-reacting vapor penetration validation.

A nozzle in that the orifice is slightly larger ($100\,\mu m$ as opposed to $90\,\mu m$), non-hydroground, has a lower length-to-diameter ratio, and has a lower discharge coefficient (0.80 as opposed to 0.86). While mixture fraction measurements have been done for a steady injection of Spray A [79], a time sequence of the starting jet was captured for Spray H that provides more interesting validation data for the model. Simulation of Spray H was achieved by adjusting the fuel density (Spray H uses n-heptane), discharge coefficient, and nozzle orifice diameter accordingly. The experimental results were obtained by measuring Rayleigh scattering from the interaction between incident 532 nm laser radiation and fuel vapor molecules [79]. Based on Sandia's measured full spreading angle, cross-sectionally averaged mixture fraction was found from their ensemble-averaged 2-D data [57].

From Figure 28, the predicted cross-sectionally averaged mixture fraction is within the bounds of the measured uncertainty, shown by the width of the red experimental curve. From analysis of the experimental images, discrepancies between the predicted and experimentally measured mixture fraction in the most upstream portion of the jet seem to be dominated by disagreements in local full spreading angle. This is likely due to the fact that the model uses a constant full spreading angle, making the modeled jet perfectly conical, while the real jet has been shown to feature a

slight transition in spreading angle between the near and far-field of the spray, and thus, is not a perfect cone [79, 80]. Having demonstrated that both penetration rate and local mixture fraction are reasonably well predicted by the numerical model, indicating that the large-scale governing fluid mechanics are captured, the coupling between mixing and chemistry is assessed below against the measured quantities of combustion observables.
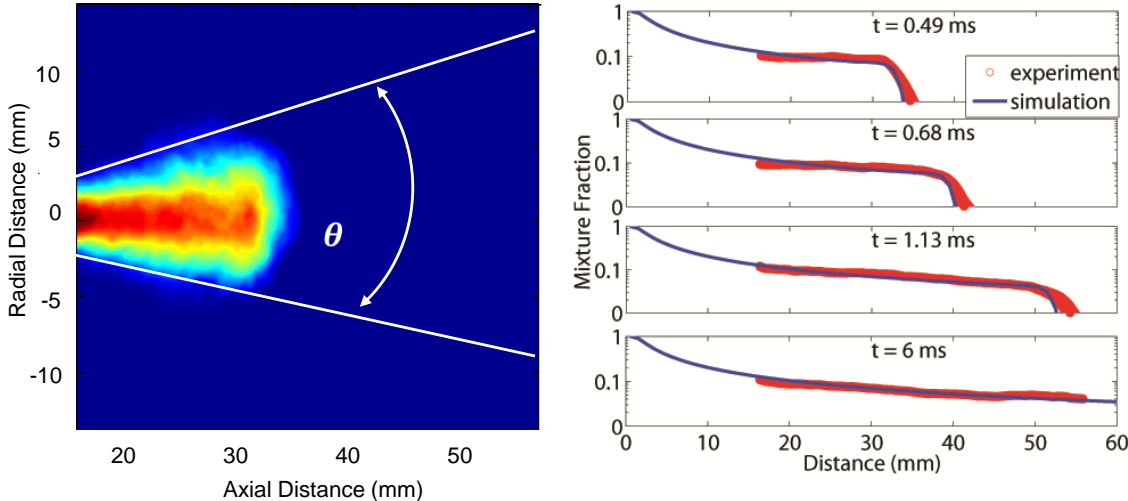
Figure 28: Ensemble and cross-sectionally averaged spray H mixture fraction validation under non-reacting conditions.

3.2 Joint Mixing-Chemistry Model Validation and Experimental Comparison with Other Institutions (Reacting)

To gain confidence in the experimental facility and optical diagnostics as well as validate the chemistry predictions of the proposed model, a comparison of combustion observables between this thesis and another institution (CMT - Motores Térmicos (CMT)) [81] that uses a similar continuous flow-through spray chamber is shown in Figure 29. Ignition delay and flame lift-off length were measured for Spray A injectors in accordance with Engine Combustion Network guidelines [57] by both institutions to ensure a valid comparison. Note that the injection pressure used by both institutions was 1000 bar and not the Spray A standard of 1500 bar. With

respect to ambient temperature and oxygen concentration, ignition delay results from this work are comparable to those from CMT. Even though the nozzles were slightly different between institutions (nozzle numbers are indicated in the figure legend), the ignition delay and flame lift-off length differences do not appear significant.

Also shown in Figure 29 are reduced-order model results of ignition delay to gain confidence in model predictions of conditions slightly beyond those tested experimentally. Since model results are likely dependent on the employed chemical mechanism, three different chemical mechanisms are used and the results from each are compared below. Note that the model uses flame lift-off length as an input and thus cannot predict its value. The Wang mechanism developed by Wang, Ra, Jia, and Reitz [82], is a reduced mechanism with 100 species and 432 reactions. The Cai mechanism is also a reduced mechanism, courtesy of Cai and Pitsch [83] with 57 species and 218 reactions. The CRECK mechanism is a detailed mechanism given by Ranzi et al. [84] and contains 451 species and 17848 reactions.

Comparison of the reduced-order model predictions and measurements of ignition delay in Figures 29a and 29b show reasonable agreement except at low temperatures and oxygen concentrations. Between the two reduced mechanisms, the Cai mechanism more closely matches the experimental ignition delay compared to the Wang mechanism for all ambient oxygen concentrations and temperatures. However, both predictions become worse at low oxygen concentration (10%) and especially at low temperature (800 K). One possible explanation is that the reduced mechanisms lose the ability to capture low-temperature pathways as reactions are either lumped or removed from the detailed mechanism on which they are based. To explore this possibility, the much more detailed (and also more computationally expensive) CRECK mechanism is used for a sweep of ambient temperatures. The ignition delay at 800 K using the CRECK mechanism is only marginally improved suggesting that a detailed mechanism is not necessarily the answer. Note that a detailed mechanism of this size

61

is computationally prohibitive in multi-dimensional spray combustion simulations. The ability to assess the impact of a very detailed mechanism with coupled mixing processes is a significant benefit of the reduced-order model. Also note that multi-dimensional spray simulations, with varying levels of complexity for both spray and turbulence-chemistry interaction sub-models, over-predict ignition delay by similar amounts to this reduced-order model [33, 82].

Interestingly, Wang et al. stated that at low temperatures, batch reactor-predicted ignition delays match well with shock tube experiments and the reason for the discrepancy of ignition delay with spray simulations is unknown [82]. Pei et al. investigated the effect of turbulence-chemistry interaction and found that ignition delay times were not improved with a complex model like the transported probability density function approach [33]. They also explored the effect of minor species (e.g. NO and OH) in the ambient gases, which are present in the pre-burn spray chamber used for validation of their data, and found a small effect that was not sufficient to explain the discrepancies in ignition delay at low ambient temperature. Pei et al. concluded their discussion on ignition delay discrepancies by suggesting that the detailed mechanism on which their reduced mechanism was based be further investigated. Based on the results using the CRECK mechanism, this work suggests agreement with Pei et al.

In an effort to further validate the chemistry prediction capabilities of the model, single-shot formaldehyde/PAH Planar Laser Induced Fluorescence (PLIF) images from Ref. [85] are shown with model predicted formaldehyde (shown as a dashed white line) in Figure 30 to compare the spatial locations of first and second stage ignition at a low ambient oxygen concentration of 10% and varying temperature. Note that these comparisons involve the use of Spray H and not Spray A. For these simulations, the Lawrence Livermore National Laboratory reduced n-heptane mechanism with 160 species and 1540 reactions was used [86]. In Figure 30, first-stage ignition is evidenced by the creation of formaldehyde, or the furthest upstream location (closest
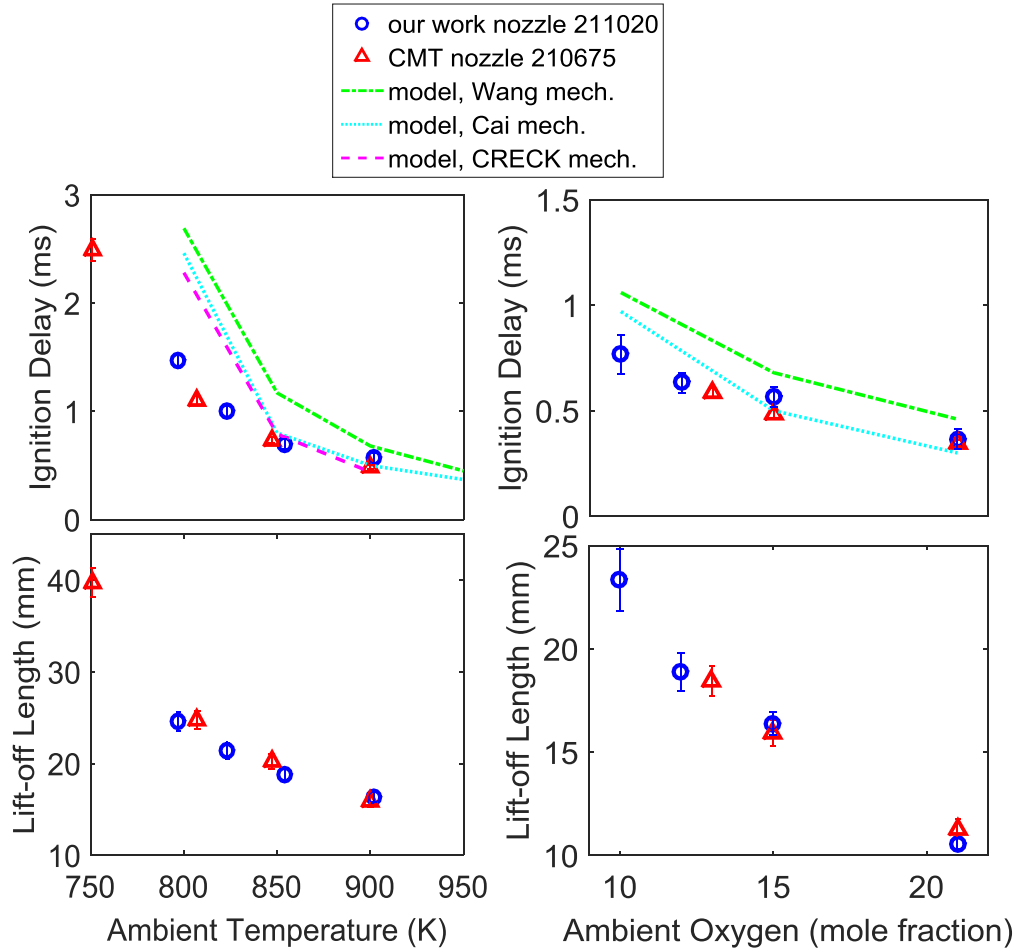
Figure 29: Comparison of experimental and model-predicted spray combustion observables for Spray A. Conditions are 900 K and 15% oxygen concentration unless otherwise specified. Note that injection pressure was 1000 bar, instead of 1500 bar. Model predictions for lift-off length are not shown since they are an input to the model.

to the injector nozzle) of a noticeable PLIF signal in the images. The solid white contour is from simultaneous OH* chemiluminescence images and indicates the border of second-stage combustion (not used for comparison to the model). The symbol "P" denotes a fuel-rich, "premixed" reaction zone that marks the transition from cool-flame/first-stage reactions to second-stage reactions, consistent with the conceptual model of Dec [14]. This fuel-rich, premixed reaction zone is identified by the observation that further downstream, past the solid white contour, the radial edges of formaldehyde begin to disappear until formaldehyde is no longer measured. This

consumption of formaldehyde along the edges is due to the mixing-layer where high-temperature combustion products from the surrounding diffusion flame mix with the fuel-rich reactants from the jet core [85]. Measurements by Collin [87] have shown that there is a disappearance of formaldehyde at the onset of second-stage ignition and thus the symbol "P" in Figure 30 marks the location of a high-temperature, fuel-rich, premixed reaction zone. Downstream of this premixed reaction zone for the 1000 K and 1100 K ambient temperature conditions, the signal is likely dominated by PAH fluorescence [85] and thus should not be considered in the comparison with model-predicted formaldehyde. The 900 K ambient temperature condition, however, does not suffer from interference due to PAH because this condition is non-sooting [85].
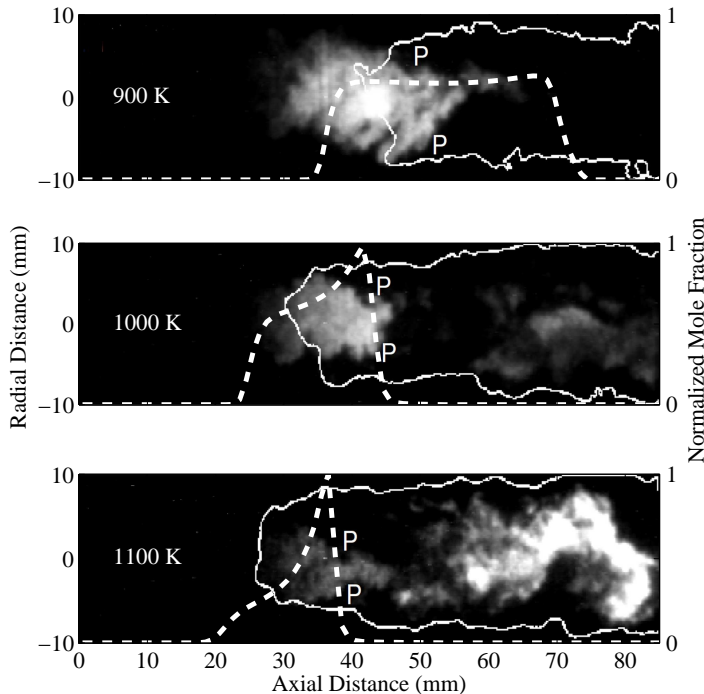
Figure 30: Spatial locations of formaldehyde/PAH from single-shot PLIF imaging [85] and model predictions (normalized mole fraction indicated by dashed line) for 10% ambient oxygen concentration. The solid white line indicates the border of second-stage combustion while "P" denotes a premixed reaction zone that consumes formaldehyde.

64

While the images in Figure 30 are single-shot and qualitative due to interference with PAH and lack of signal calibration, a comparison of axial locations for the creation and destruction of formaldehyde can still be made. For the higher ambient temperatures of 1000 K and 1100 K, the axial locations of formaldehyde creation and destruction agree reasonably well between the PLIF images and model predictions (dashed lines). For the lower ambient temperature of 900 K, the model prediction is not in complete agreement with the imaging, possibly due to shot-to-shot variation or chemical mechanism deficiencies. The model predicts that formaldehyde is first formed at 35 mm from the injector nozzle while experimental imaging shows formaldehyde is first formed approximately 28 mm from the injector. However, the persistence of predicted formaldehyde is consistent with the experimental imaging in that both predict destruction of formaldehyde by approximately 65 mm from the injector nozzle. Although the formaldehyde signal is weak by the location of destruction, Ref. [85] clearly shows complete disappearance of formaldehyde by 65 mm from the injector nozzle. Based on this analysis, at lower ambient temperatures, the model is expected to over-predict the axial location of first stage ignition while reasonably capturing the location of second-stage ignition.

CHAPTER IV

INJECTION SYSTEM CHARACTERIZATION

Many of the experimental results presented in this section have been published in previous works by the author and will be shown here for posterity [52, 53, 54].

4.1 Rate-of-Momentum Measurement Uncertainties

While several researchers have employed the impingement technique to quantify rate-of-momentum [21, 60, 61, 62], questions still surround its use. No study has clearly outlined and estimated the possible sources of uncertainty in the rate-of-momentum measurement or provided estimates of the relative importance of each uncertainty in the rate-of-momentum or nozzle flow coefficients uncertainties. An important subsection of this thesis is to address these issues, enabling higher confidence in the injection rate profiles as well as more wide spread use of the rate-of-momentum measurement.

Uncertainties in the rate-of-momentum measurement are classified under two categories; precision or systematic. Precision uncertainties arise from random fluctuations in the rate-of-momentum measurement system. For example, electrical noise and fluctuations in pump pressure at the time of injection are common sources. Systematic uncertainties are those that deviate the measurement from the true value and are difficult to quantify, since a more accurate transient rate-of-momentum measurement device does not exist. Fortunately, from sensitivity analysis, estimates can still be made of the systematic uncertainties in the rate-of-momentum measurement due to quantities like fuel temperature, angular alignment, as well as calibration and transducer parameters.

The expanded precision uncertainty, σ_A, is found from repeated sampling of the data to obtain a sample standard deviation, SSD, and coverage factor, k_c. Then,

this value is modified by the number of samples N for a 95% confidence interval in the following way:

$$\sigma_A = \frac{k_c SSD}{\sqrt{N}}.$$ (29)

Equation 29 represents the shot-to-shot deviation between repeated experiments. In all figures below, the vertical error bars are based on this equation. Systematic uncertainties are estimated by performing an experimental sensitivity analysis to obtain the influence coefficient, $\partial \overline{\dot{M}_f}/\partial x_j$, for each parameter x_j. For example, x_j may be fuel temperature or angular alignment. The uncertainty in each parameter, σ_{x_j}, is then estimated from observation, and the expanded systematic uncertainty, σ_B, is determined from:

$$\sigma_B = \sqrt{\sum_j \left(\frac{\partial \overline{\dot{M}_f}}{\partial x_j}\sigma_{x_j}\right)^2}.$$ (30)

Combination of precision and systematic uncertainties is performed to obtain a combined uncertainty, σ_C, assuming that all parameters are independent [88]:

$$\sigma_C = \sqrt{\sigma_A^2 + \sigma_B^2}.$$ (31)

4.1.1 Strike Cap Sensitivity

The strike cap is an essential feature of the rate-of-momentum measurement if using a pressure transducer (as opposed to the more conventional use of a force transducer). Without the strike cap, conversion from units of pressure to force can be difficult, since the distribution of spray momentum is transmitted over an unknown area of the transducer. Thus, the strike cap serves to uniformly redistribute the applied force from the spray over a known area. The strike cap also serves to provide a mechanical barrier between the spray and the face of the transducer. Protection of the sensor face from the spray is important because piezo-based sensors are sensitive

to high-temperature fuel and mechanical failure like pitting. Pitting causes the fuel spray to be re-directed back towards the orifice, transferring more momentum to the sensor and resulting in a higher measured signal. With prolonged use, or a soft strike-cap material, pitting of the strike cap surface may occur, resulting in an increase in measured rate of momentum [62].

Three different strike cap designs were considered in order to determine the sensitivity on the measured rate of momentum. Each strike cap was secured to the transducer with a strong and rigid adhesive, Loctite Instant-Bonding Adhesive #415. Within the frequencies resolved by the DAQ, the resonant frequency of the sensor was not affected. Therefore, the sensor response with and without the strike cap and adhesive is likely to be identical. An attempt to secure the strike caps using wax and RTV silicone gasket sealant was made, but they ultimately failed after only a few injections. As shown in Figure 31, different strike cap dimensions with various stem widths were selected to test the effect of its mechanical coupling to the diaphragm of the PCB 113B26 pressure transducer.

Calibration of each strike cap used with the PCB 113B26 pressure transducer was performed using the dead-weight methodology described in the Chapter 2 of this thesis, and is shown in Figure 31a. Also shown is the factory calibration, with pressure converted to force using the factory specified transducer area, for comparison purposes. The calibration constants, or calibration sensitivities, are given in the plot as well. From these results, it is evident that the sensitivity decreases with increasing stem diameter. As the stem diameter increases for each strike cap, more force is transferred to the sensor housing than to the sensor element. Uncertainty in each calibration constant is estimated using, $\sigma_{calibration} = k_c SEE$, where SEE is the Standard Error of Estimate. Uncertainty in the calibration for each strike cap was found to be 28%, 6%, and 2% for caps 1, 2, and 3 respectively.

The same strike caps were then used to observe the effect on the mean measured

rate-of-momentum over twenty injections, shown in Figure 31b. With identical fuel momentum rate applied to the transducer via controlled injection pressure, the strike cap with the largest stem diameter (Cap 1) produced the lowest signal. This finding is in agreement with the reduced sensitivity found from the dead-weight calibration in Figure 31a. There also appeared to be significant drift in the measured signal over the duration of the injection using the largest stem diameter strike cap. Fluctuations in the measured signal are also very large, compared to those measured with smaller diameter strike caps.
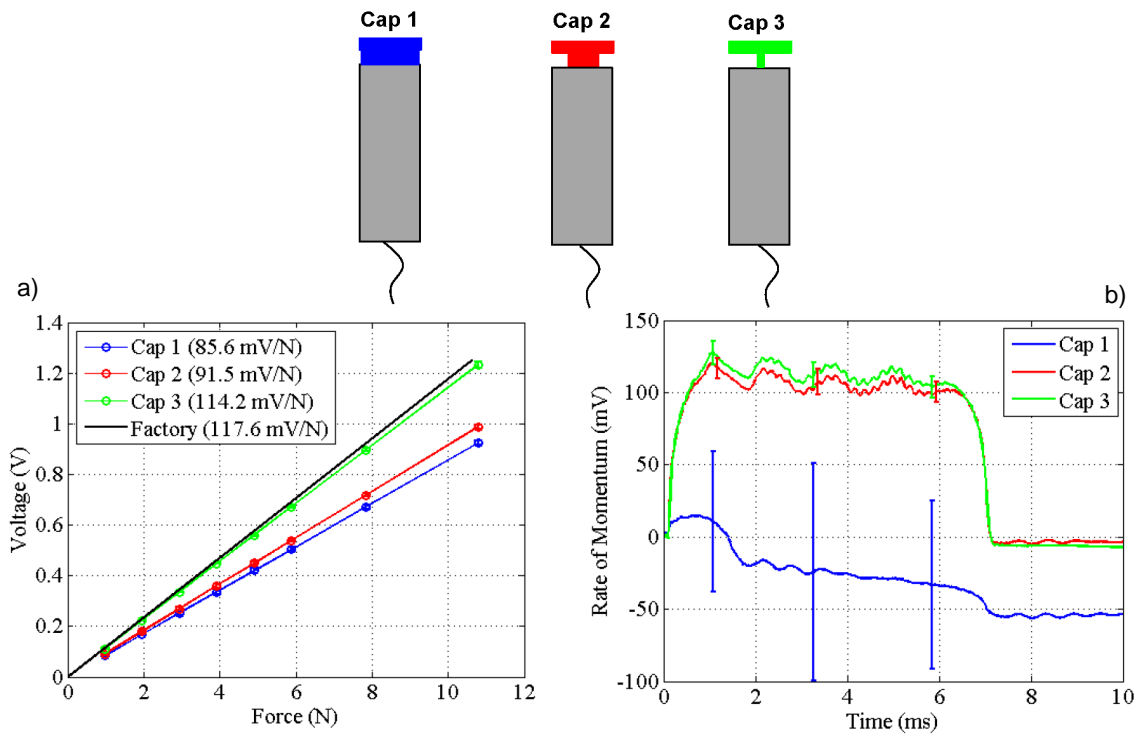
Figure 31: a) Calibration curves using the different strike caps; b) raw rate-of-momentum signal for each strike cap.

The raw rate-of-momentum signals were then calibrated for force, using the appropriate calibration constant from Figure 31a, and corrected for drift by applying a linearly increasing correction over the duration of the injection, based on the end-of-injection offset from zero volts. The calibrated and corrected measurements are shown in Figure 32a. Even with appropriate calibration and correction, the strike

69

cap with the largest stem diameter (Cap 1) proved to be impractical, yielding large shot-to-shot variation. The strike cap with the intermediate stem diameter (Cap 2) also exhibited higher shot-to-shot variation in both the calibration and rate-of-momentum measurement, contributing to larger uncertainties compared to the strike cap with the smallest stem diameter. Note that the large-scale oscillations in the rate-of-momentum profiles have a frequency of approximately 750 Hz and are due to acoustic oscillations in the fuel line (see the injection pressure trace in Figure 32b). There are also small-scale oscillations at a higher frequency of 5 kHz, which have been attributed to motion of the injector body as measured by an attached accelerometer in Ref. [59].
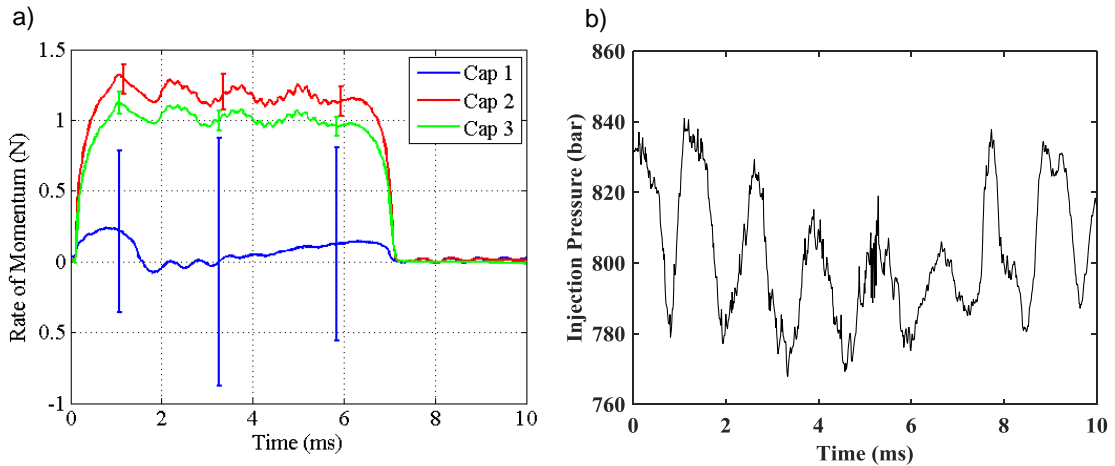
Figure 32: a) Calibrated and drift-corrected rate of momentum for each strike cap; b) injection pressure measured in the fuel line 7 cm upstream of the injector body inlet.

From these results, systematic uncertainty in the measured rate-of-momentum, due to strike cap geometry, will manifest itself in the calibration uncertainty. Therefore, it did not appear necessary to find an influence coefficient in this case, and it was assumed equal to unity. Also from these results, the strike cap geometry should be such that there is minimal contact area with the pressure transducer's diaphragm. Informed by these findings, the strike cap with the smallest stem diameter was used

70

for all other tests presented.

4.1.2 Angular Sensitivity

Having selected a strike cap design that reduced the calibration error, the sensitivity in rate-of-momentum due to misalignment of the spray with the transducer was then investigated. Non-orthogonality between the spray and transducer surface plane will result in a decrease in measured rate-of-momentum. Therefore, the time-averaged rate-of-momentum during the steady portion of injection, $\overline{\dot{M}_f}$, was measured versus polar angle, as shown in Figure 33. Twenty injections were performed to obtain a mean value at each polar angle. Vertical uncertainty bars are represented by Eq. 29, while horizontal uncertainty bars are representative of an estimated 1 deg. uncertainty in the desired angle. This estimate was obtained based on the resolution of the angle measurement within the experimental setup.
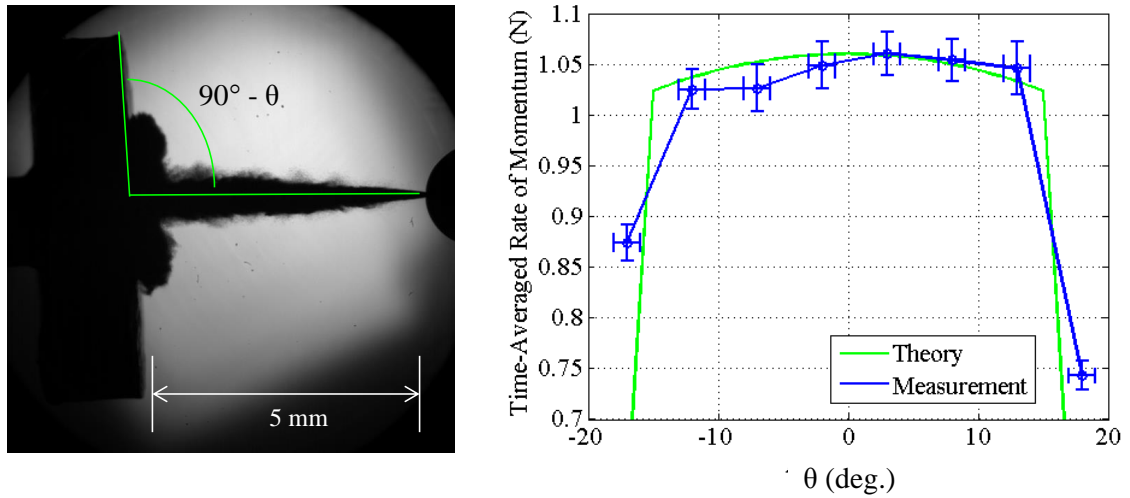
Figure 33: Angular sensitivity for time-averaged rate-of-momentum over steady portion of injection.

Also shown in Figure 33 is the angular sensitivity as predicted by control volume analysis (theory). The predicted rate-of-momentum due to misalignment can be represented by $\overline{\dot{M}_f} = \rho_f U_{eff}^2 A_{eff} cos\theta$, where θ represents the angle away from the transducer axis. The steep drop at 15 deg. is due to the spray no longer impacting

the transducer. Estimates of this angular position are found from the transducer diameter and distance to the nozzle. From Figure 33, the measured angular sensitivity agrees with the predictions. Therefore, the influence coefficient in the measured rate-of-momentum due to angular misalignment is $\partial \overline{\dot{M}_f}/\partial \theta = \rho_f U_{eff}^2 A_{eff} sin\theta$. As an example, while the experimental angular uncertainty was only 1 deg., for a less precise angular alignment of 5 deg., the measured rate-of-momentum varies by only 2%. The rate-of-momentum measurement is therefore insensitive to modest angular misalignment. Such insensitivity is in agreement with work from Peters [89] and Gimeno [90].

4.1.3 Fuel Temperature Sensitivity

Since many research groups conduct measurements under conditions where the injector body is heated [25, 62], the sensitivity of the measured rate-of-momentum to fuel temperature is shown in Figure 34a. The calibration constant for the smallest stem diameter strike cap was applied, but the signals were not corrected for drift. Lindström and Ångström have attributed drift in measured rate-of-momentum over the duration of an injection to temperature of the fuel [62]. They arrived at this conclusion from their observation that drift was nearly eliminated by the application of a strike cap, thereby thermally separating hot fuel from the sensor. This work shows, however, that drift, as indicated by a drop in measured signal after the end of injection to values below zero, appears to be insensitive to fuel temperature. Comparing the relative drift that occurs after the end of injection in Figure 31b and Figure 34a, the strike cap geometry has a far greater influence. The conclusion made by Lindström and Ångström may have some validity though. The Kistler 4065 transducer used for their rate-of-momentum measurements has much higher temperature sensitivity, by a factor of 19, than the PCB 113B26 transducer used for this study, potentially indicating the importance of this transducer property when selecting a

sensor for rate-of-momentum measurements with heated fuel conditions.
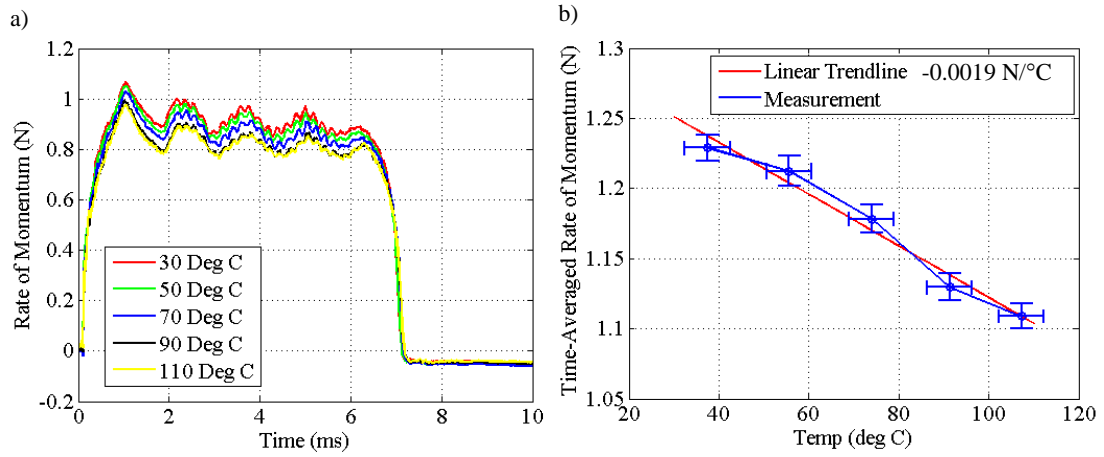
Figure 34: a) Calibrated, but not drift-corrected, rate of momentum versus time for different injector body temperatures; b) temperature sensitivity for time-averaged rate of momentum over steady portion of injection.

Figure 34b shows a linear regression of the time-averaged rate of momentum during the steady portion of injection demonstrating the effect of fuel temperature on the rate of momentum signal. The regression coefficients are displayed in the figure as well. Based on this regression, the influence coefficient in the measured rate-of-momentum due to fuel temperature is $\partial \overline{\dot{M}_f}/\partial T_f = -0.0019$ N/°C. PCB specifies the maximum temperature sensitivity of the transducer as -0.054%/°C or -0.00054 N/°C, using a representative value of 1 N. Since the measured rate of momentum sensitivity to temperature is much higher, by almost an order of magnitude, than the maximum specified by the manufacturer, the measurement indicates that the nozzle flow is changing in nature. From these results, accurate knowledge of the fuel temperature is important to properly account for the change in fluid properties. This is especially important for experiments that use heated ambient environments, such that the injector tip and fuel within the sac experience temperatures in excess of 100°C [57].

73

4.1.4 Transducer Selection

To understand the influence of transducer properties (e.g. axial acceleration sensitivity and resonant frequency) on the measured rate-of-momentum and to estimate the systematic uncertainties associated with these properties, two different piezoelectric transducers were then used to compare signals at the same nozzle relative position. Axial acceleration sensitivity refers to the false signal that arises when the sensor element is accelerated along its axis. Resonant frequency, f_n, specifies an upper limit to the stable frequency response of the sensor. The first sensor was the PCB 113B26 pressure sensor calibrated for force measurements, used in the previously presented measurements, while the second was a Kistler 9215 force transducer. Presented below in Figure 35a, are ensemble-averaged rates-of-momentum using each transducer, under identical conditions such as injection pressure, fuel temperature, and angular alignment. The results indicate that while the Kistler 9215 force transducer has an axial acceleration sensitivity nearly two orders of magnitude higher than the PCB 113B26 pressure transducer, the main features of the rate of momentum are similar. Also, the resonant frequency of the Kistler 9215 (>80 kHz) is much lower compared to the PCB 113B26 (>500 kHz). From these results, there appears to be negligible systematic uncertainty due to axial acceleration sensitivity and resonant frequency.

The maximum false signal that may appear at the beginning of an injection is estimated by considering an equation of motion for a free sensor body, $m_{sensor}a_{max} = \dot{M}_{f,max}$. If we use a maximum rate of momentum of 1 N and a sensor mass, m_{sensor}, of 6 grams [91], estimation of the maximum acceleration a_{max} experienced by the sensor body as a result of fuel spray impact is approximately $167\,\mathrm{m\,s^{-2}}$ (17 g). Using an axial sensitivity of 3.2e-5 N/g (given by PCB [91]), the maximum false signal possible is estimated to be 0.00054 N. This value is very small relative to the measured rate-of-momentum ($\sim$0.05%). The extremely low acceleration sensitivity of the PCB 113B26 is due to the built-in acceleration compensation. For transducers that are not
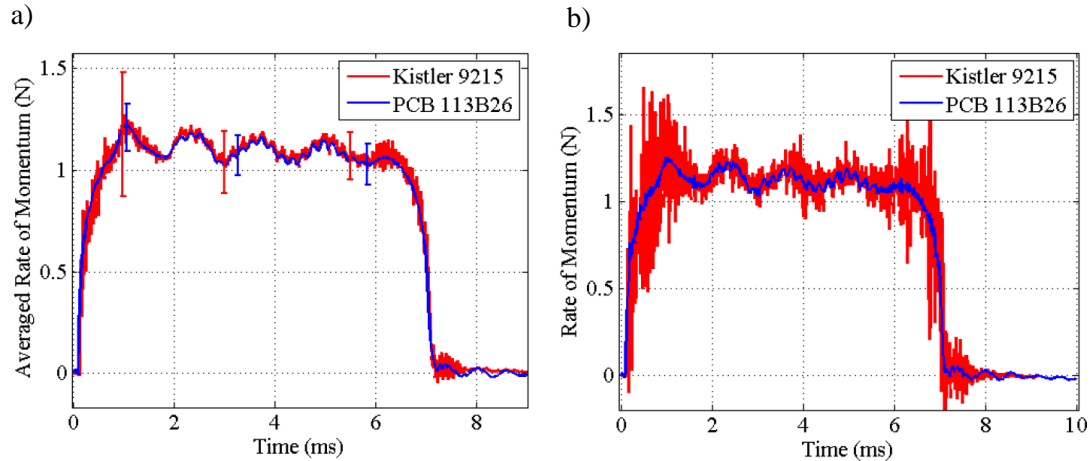
Figure 35: a) Ensemble-averaged rate of momentum; b) single injection rate-of-momentum using two different sensors under identical conditions.

acceleration compensated, e.g. Kistler 9215, an estimate of the false signal is 0.034 N, using an axial sensitivity of 2e-3 N/g [92]. While this value is small, ~3% of the steady-state rate-of-momentum, other non-acceleration compensated transducers like the Kistler 4065 may experience a much greater false signal, due to an even larger axial acceleration sensitivity. Indeed, using the same analysis as above and an axial acceleration sensitivity of 2.5e-2 N/g [93], the Kistler 4065 sensor may suffer a false signal up to 0.43 N or ~43% of the steady-state rate-of-momentum.

Random fluctuations in the measured rate-of-momentum due to electrical noise were evaluated by comparing single shot traces between the two transducers, presented in Figure 35b. As seen by comparing the two traces, the PCB 113B26 pressure sensor exhibited much less noise compared to the Kistler 9215. This is likely due to the relative position of the charge amplifier to the sensing element. The PCB 113B26 sensor is an Integrated Electronic PiezoElectric (IEPE) sensor, meaning that the charge amplifier is located directly next to the sensor. This design reduces noise often seen with signals arising from long cables between sensor and amplifier. The Kistler 9215, however, is separated from the 5010B charge amplifier by a 1-m cable, and is thus more susceptible to electromagnetic interference and triboelectric noise.

Table 4: Rate-of-Momentum Measurement Uncertainties

Parameter	Influence coefficient	Individual uncertainty	Relative contribution
Strike Cap Calibration	Unity[1]	2% using Cap 3	6%
Angular Alignment	$\rho_f U_{eff}^2 A_{eff} \sin\theta$	1 deg.	6%
Temperature	-0.0019 N/°C	10°C	26%
Electrical Noise & Rail Pressure Fluctuations	Unity[1]	6% using PCB113B26	62%

[1]Assumed

It is difficult to separate out the relative contributions of electrical noise and injection pressure variations from the total precision uncertainty because tests cannot be conducted for each contribution independently. The variation in injection pressure is due to the design of the pump. The injection frequency was 0.3 Hz while the pump stroking frequency was approximately 0.5 Hz, which is dependent on desired injection frequency, fuel pressure, and leakage of fuel through the spill port of the injector. Therefore, overlap of these two events is experimentally unavoidable without a feedback loop between the pump pressure and injector initiation. By comparing the single injection and ensemble-averaged rate-of-momentum traces as measured by the PCB113B26 sensor, the two are very similar suggesting that the precision uncertainty is dominated by injection pressure variations. In summary, the precision uncertainties were found to be 0.06 N and 0.11 N for the PCB 113B26 and the Kistler 9215, respectively. These values are 6% and 11% of the steady-state rate-of-momentum.

Table 4 presents a summary of the individual uncertainties that make up the combined uncertainty in the rate-of-momentum measurement. Following from Equation 31, the combined uncertainty in the rate-of-momentum measurement is approximately 0.07 N, or 7% of the steady-state value. From these results, it is clear that the electrical noise and fluctuations in pump pressure are the most important contributors to the combined uncertainty.

4.1.5 Transients

Uncertainties in the measured rate-of-momentum due to strike cap geometry, angular alignment, fuel temperature, and electrical noise/rail pressure fluctuations were mainly assessed by analyzing the steady portion of injection. Measurement uncertainties that arise during the transients, i.e. start- and end-of-injection, and are much less straightforward to quantify. The next section aims to understand these potential sources of uncertainty again through the use of two sensors with different characteristics and also through high-resolution back-lit microscopy. Imaging of a spray without interference from other plumes was achieved by employing an injector with a single axially-drilled hole. For this purpose, a solenoid-actuated ECN Spray A injector (#211020) with a hydroground, 90 μm diameter hole (k-factor = 1.5) is used. To support ECN measurements of Spray A, the fuel used was 99+% n-dodecane.

4.1.5.1 Sensor Resonant Frequency Excitation

In practice, $f_n/5$ is typically where the frequency response deviates by 5% of the stable region and is thus used as the practical upper limit. If an impact force is sufficiently rapid, the resonant or natural frequency of the sensor may be excited resulting in a false signal. Typical resonant frequencies of sensors are approximately 50 kHz. Estimation of the rate of impact force or initial slope in rate-of-momentum required to excite a typical sensor's resonant frequency is roughly $1/(f_n/5) = 100\,\mu\text{s}$. Since the internal volume of the single-hole Spray A injector likely fills much faster compared to the commercial 7-hole injector used previously, we accept the possibility of resonant frequency excitation of typical sensors.

To explore this possibility, measurements were conducted of the rate-of-momentum using the two different sensors previously discussed. Again, resonant frequencies for both the Kistler 9215 and the PCB 113B26 are >80 kHz and >500 kHz, respectively. From Figure 36, the Kistler transducer shows a high overshoot at the start-of-injection

transient, which could be due to resonant frequency excitation. This artifact could also be a result of the Kistler transducer's high axial acceleration sensitivity compared to the PCB transducer. The PCB transducer has built-in acceleration compensation and thus low acceleration sensitivity (in addition to high resonant frequency), so the initial rate-of-momentum is not corrupted by the sensor. At steady state, the expanded precision uncertainties are nearly identical for each transducer, suggesting that the uncertainties at steady injection are dominated by shot-to-shot variation and not transducer characteristics.
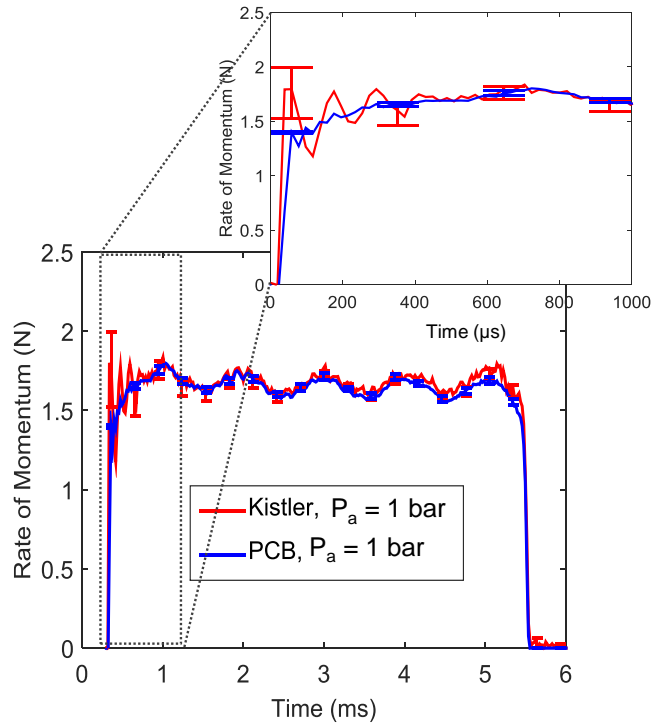
Figure 36: Identification of rate-of-momentum artifacts at the starting transient.

4.1.5.2   Possibility of Mass Accumulation at Head of Spray

Accumulation of fluid at the head of the spray during the initial injection transient has been suggested as a possible cause for rate-of-momentum artifacts during the initial transient [60]. As the needle in the injector opens, fluid exiting the nozzle orifice increases in velocity until the needle fully opens. Because fluid velocity increases as

the needle opens, fluid injected later in the transient catches up with fluid injected initially, potentially causing mass accumulation at the head of the spray. This mass accumulation could then create an artifact in the rate-of-momentum measurement at the start-of-injection transient which does not replicate the true rate-of-momentum exiting the nozzle orifice.

To better understand the possibility of mass accumulation, instantaneous images of spray optical thickness, KL, are captured just prior to impingement on the sensor face in Figure 37. While these measurements cannot be used as a direct measurement of fuel mass distribution, they can be used to identify the spray boundary [94]. With knowledge of the instantaneous spray boundary, evidence of mass accumulation can be found by observing a "mushroom-like" spray where the tip is much wider than the body. Figure 37 demonstrates that under a brief range of ambient and injection pressures, the instantaneous spray boundary does not mushroom out at the tip like that described in Ref. [95] indicating that little to no mass accumulation exists. It is important to note that the images in Ref. [95] are point-based projected mass measurements that are ensemble-averaged over many injections and are thus not an instantaneous representation of the spray, like the images shown here. Indeed, more recent work performed in the same laboratory has shown very large standard deviations at the head of the spray, indicating that the apparent mass accumulation described in Ref. [95] is merely due to shot-to-shot variation [96] and is not actual mass accumulation. These findings suggest that any artifacts in the Spray A rate-of-momentum measurements during the start-of-injection transient should not be attributed to mass accumulation since this phenomenon does not appear to be present.

4.1.5.3   Effect of Back-Pressure

When conducting measurements of the instantaneous fuel spray rate-of-momentum using the impingement technique, the transducer is measuring the reaction force, R_F,
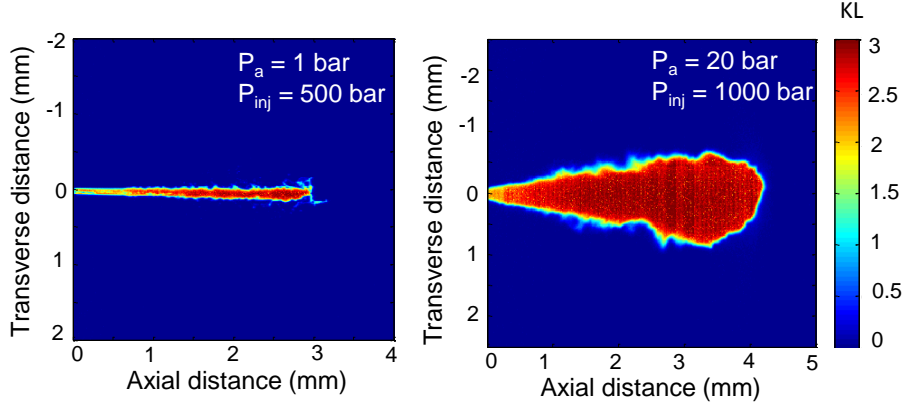
Figure 37: Instantaneous optical thickness distribution during starting transient.

of the control volume drawn in Figure 16. In order to find the instantaneous rate-of-momentum of the spray, $\dot{M}_f$, located at the exit of the nozzle, control volume analysis must be used to relate the measured reaction force to this quantity. Conservation of momentum in the axial direction, x, for the control volume in Figure 16 is shown in Eq. 32.

$$
\begin{aligned}
& i.\frac{\partial}{\partial t}\int \rho_a U_{x,a}dV_a + ii.\frac{\partial}{\partial t}\int \rho_f U_{x,f}dV_f \\
& +iii.\int \rho_a U_{x,a}(\bar{U}\cdot\bar{n}_{upper})dA_{upper} + \dot{M}_f+ \\
& iv.\int \rho_a U_{x,a}(\bar{U}\cdot\bar{n}_{side})dA_{side} + v.\int \rho_f U_{x,f}(\bar{U}\cdot\bar{n}_{side})dA_{side} \\
& +R_F + vi.\int pdA_{lower} + vii.\int pdA_{upper} = 0
\end{aligned}
\tag{32}
$$

Each term in Eq. 32 is preceded by a roman numeral to aid in identification for later discussion. Terms i. and ii. describe the time rate of change of air and liquid spray within the control volume. Term iii. describes air entering the top of the control volume while terms iv. and v. describe air and spray entering/leaving the sides of the control volume. Terms vi. and vii. are the force due to pressure across the bottom and top of the control volume respectively.

80

It is common to simply equate the reaction force, R_F, with the instantaneous rate-of-momentum of the spray, $\dot{M}_f$, because many terms are difficult quantify, especially the terms involving air. A typical liquid fuel density is approximately $700\,\mathrm{kg\,m^{-3}}$, which is more than two orders of magnitude greater than the air density, $1.2\,\mathrm{kg\,m^{-3}}$, at atmospheric pressure. Therefore, at atmospheric pressure, terms i., iii., and iv. are negligible and can be removed from the equation without a large penalty. However, under 60 bar ambient gas pressure the density of air is $71\,\mathrm{kg\,m^{-3}}$, such that terms i., iii., and iv. are likely no longer negligible.

As shown in Figure 38a, the rate-of-momentum profiles under elevated back pressure have different start- and end-of-injection transients when compared to measurements under atmospheric pressure. The decrease in rate-of-momentum during the steady portion of injection in Figure 38 can be fully explained by accounting for differences in the nozzle flow coefficients (shown later) and the reduced pressure drop across the nozzle orifice at elevated back pressure while the differences observed during the transients cannot. These differences in the rate-of-momentum profiles are suggested to be due to the increased density of the air, which increases by over an order of magnitude from 1.2 to $71\,\mathrm{kg\,m^{-3}}$. From Eq. 32, an increase in air density by an order of magnitude makes terms involving air density non-negligible. If terms i., iii., and iv. in Eq. 32 are neglected under elevated back pressure, the measured rate-of-momentum will not be the true value.

Because injection velocity is a common input to simulations, like the model in this thesis, the rate-of-momentum was converted to injection velocity by assuming a constant area contraction coefficient of 0.91 and a liquid fuel density of $699\,\mathrm{kg\,m^{-3}}$. Results at two different back pressures are shown in Figure 38b where time is relative to after the start of ramp-down (ASORD). The measurement under high back pressure (60 bar) shows a much longer end-of-injection transient compared to the atmospheric back pressure condition. Since we have no way of easily measuring many of the

terms in Eq. 32, we must equate the reaction force, R_F, with the instantaneous rate-of-momentum of the spray, $\dot{M}_f$. But, accurate measurement of the end-of-injection transient is of particular importance to this thesis. Therefore, the end-of-injection transient durations are taken as those measured at atmospheric back pressure.
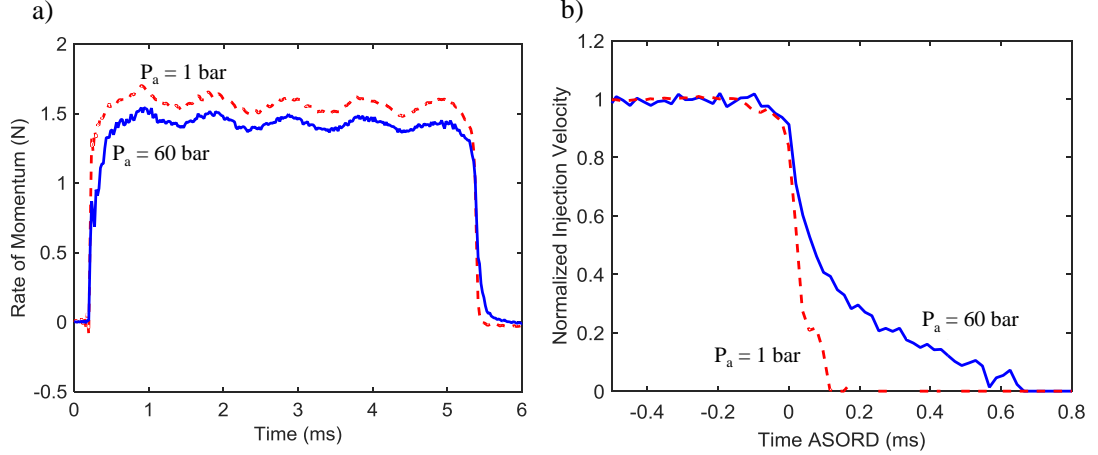
Figure 38: a) Measured rate-of-momentum at two different back pressures; b) measured injection velocities normalized by their steady-state values. Steady-state injection velocity = 542 m/s for P_a = 1 bar and 465 m/s for P_a = 60 bar.

4.2 Fuel Injector Nozzle Flow Characterization

Fuel injector nozzle flows are typically characterized by nozzle flow coefficients such as discharge, C_d, velocity, C_v, and area contraction, C_a. Both the rate-of-momentum and rate-of-injection need to be measured in order to find these nozzle flow coefficients. By measuring the rate-of-momentum for a single orifice and the total collected mass, m_{inj}, over N injections with the number of holes, n_{holes}, the individual nozzle-hole rate of injection may be found from

$$\dot{m}_f = C\sqrt{\dot{M}_f},$$ (33)

where C may be found from

$$C = \frac{m_{inj}}{N n_{holes} \int \sqrt{\dot{M}_f} dt}. \tag{34}$$

The effective velocity, U_{eff}, is the mean velocity of the fuel exiting the injector orifice, and can then be calculated as:

$$U_{eff} = \frac{\dot{M}_f}{\dot{m}_f}. \tag{35}$$

The theoretical velocity, U_{th}, of the fuel at the exit of the injector orifice may be found from the injection pressure, P_{inj}, ambient pressure, P_a, and the fuel density, ρ_f, with Bernoulli's equation:

$$U_{th} = \sqrt{\frac{2(P_{inj} - P_a)}{\rho_f}}. \tag{36}$$

From this analysis, the velocity coefficient can be defined as:

$$C_v = U_{eff}/U_{th}. \tag{37}$$

Physically, the velocity coefficient represents the loss in flow velocity due to viscous, turbulent, or cavitation effects. Similarly, the effective flow area, A_{eff}, can be defined as:

$$A_{eff} = \frac{\dot{m}_f{}^2}{\rho_f \dot{M}_f} \tag{38}$$

and the area contraction coefficient as:

$$C_a = A_{eff}/A_{geo}, \tag{39}$$

where A_{geo} is the geometrical area of the nozzle orifice. The area contraction coefficient is a term that incorporates the loss of flow area from cavitation or other orifice-flow effects. Finally, the discharge coefficient is defined as

$$C_d = C_v C_a \tag{40}$$

and represents the reduction in mass flow through the orifice compared to an ideal scenario. It should be noted that this analysis applies only to the quasi-steady portion of the injection duration.

Measurements of the nozzle flow coefficients have been conducted for the Spray A injector (#211020) used in this work for a range of back pressures (shown versus cavitation number, K). This injector had not been previously characterized by the ECN community whereas the Spray D injector (#209133) was previously characterized by CMT [97]. The results in Figure 39 show that some of the nozzle flow coefficients for this particular injector change dramatically for different back pressure conditions. The cavitation number, K, is used to display the different back pressure conditions on the abscissa in Figure 39 and is defined as $K = (P_{inj} - P_v)/(P_{inj} - P_a)$ [98]. Figure 39 suggests that this particular Spray A injector cavitates at atmospheric back pressure (K = 1) and transitions to less cavitating or non-cavitating by 30 bar (K = 1.02). Lopez and coworkers state that the rate-of-momentum is reduced under cavitating conditions but not as much as the mass flow rate, indicating an increase in effective velocities and thus an increase in velocity coefficients to values greater than unity [99]. These values will be used in the boundary conditions for modeling of the spray/jet.

Lastly, Table 5 compares the relative contribution of uncertainty in individual parameters to the total nozzle flow coefficient uncertainties. The parameters are such that they appear explicitly in each of the nozzle flow coefficient equations. The total uncertainty for the area contraction, velocity, and discharge coefficients are 1%, 7%, and 6% of their nominal value, respectively. The uncertainty in the velocity coefficient strongly depends on measured rate-of-momentum, thus proving the importance of understanding and reducing the uncertainties in the measurement. Conversely, the area contraction coefficient depends almost entirely on the measured orifice area,
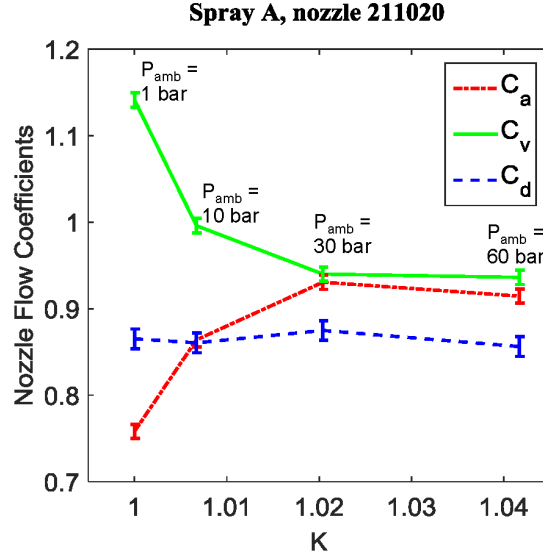
Figure 39: Nozzle flow coefficients for Spray A injector (#211020) as a function of cavitation number, K.

Table 5: Nozzle Flow Coefficient Relative Uncertainties

	Injection Pressure	Orifice Area	Rate-of-Momentum	Rate-of-Injection	Fuel Density
C_v	9%	-	91%	<<1%	<<1%
C_a	-	100%	<<1%	<<1%	<<1%

which stresses the need for accurate measurements of the nozzle orifices.

4.3 Injection Rate-Shaping Capabilities

Now that uncertainties in the rate-of-momentum measurement have been identified, quantified, and minimized with careful selection of hardware, there is a high level of confidence to accurately measure the injection rate profile, or *shape*. This knowledge was essential to verify that the injection rate shape was perturbed in a significant way, which will then allow the impacts of injection rate shape on combustion outcomes to be assessed.

Two end-of-injection transients (fast ramp-down (RD) and slow RD) were selected for each nozzle diameter, d_0, and injection pressure, P_{inj}. These two end-of-injection

transients represent the likely bounds of practical engine strategies. Shorter end-of-injection transients are not likely to be possible since engine manufacturers have already minimized this portion of the injection event to the best of their abilities. Longer end-of-injection transients than the one chosen here may be feasible but engine timescales and other potentially detrimental factors likely limit the end-of-injection transient to less than ~2 ms.

Rate-of-momentum and injection pressure measurements are shown in Figure 40. Note that the rate-of-momentum measurements lag behind the injection pressure measurements by ~1 ms. This is because the injection pressure sensor is located far upstream relative to the rate-of-momentum sensor and information takes a finite amount of time to propagate downstream. As previously discussed in Chapter 2, the newly developed injection rate-shaping system uses a discharging injector that opens at some point during injection to allow the pressure behind the experimental injector to rapidly decay. This rapid pressure drop causes a rapid decrease in the spray rate-of-momentum, creating the first phase of ramp-down for the slow RD profile. The first phase of ramp-down starts at approximately 3000 µs and ends around 4000 µs. The second phase of ramp-down is not controlled via pressure supplied to the injector, like the first-phase, but rather the injection is throttled by needle-closing. The needle closes very rapidly during this phase causing complete cessation of injection in approximately 100 µs. Unlike the slow RD profile, the fast RD profile is exclusively controlled by needle closing.

Normalized injection rate profiles are shown in Figure 41, where the injection velocity was obtained via the previously shown rate-of-momentum measurements. To convert the measured rate-of-momentum to velocity, the area contraction coefficient (measured to be 0.91 during steady injection) was assumed to be constant during ramp-down and liquid fuel (n-dodecane) density was determined to be $699 \, \mathrm{kg \, m^{-3}}$ [100]. Then, each profile was normalized by its steady injection velocity, U_0. The fast
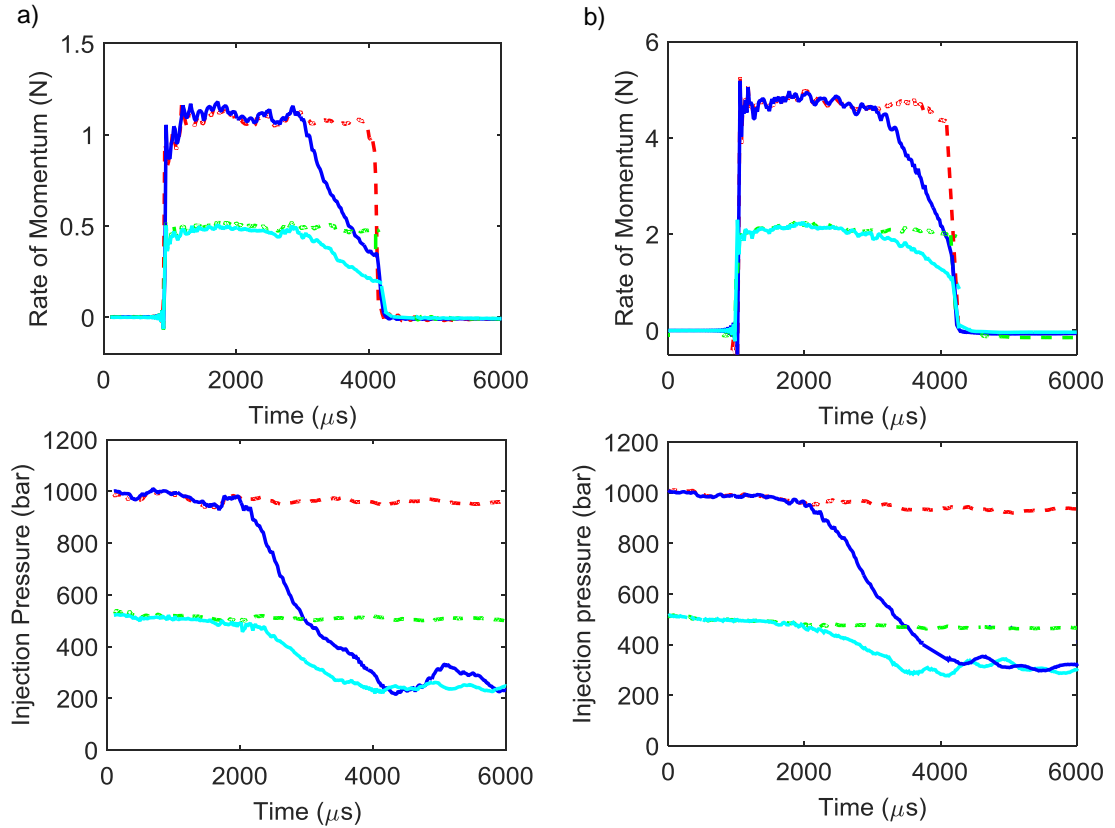
Figure 40: Rate-of-momentum (top) and fuel pressure (bottom) measurements for two different end-of-injection transients; a) Spray A nozzle #211020 - 90 μm orifice diameter and b) Spray D nozzle #209133 - 186 μm orifice diameter.

RD profile is nearly linear and has the same characteristic timescale of velocity decrease [101], $\alpha = U_0/(dU_0/dt) \approx 100$ μs, regardless of injection pressure and nozzle diameter. The normalized slow RD profiles are also nearly identical to one another but they are not linearly decreasing like the fast RD, i.e. there are two distinct slopes. Thus, it is difficult to quantify a single characteristic timescale of velocity decrease for the slow RD profile.
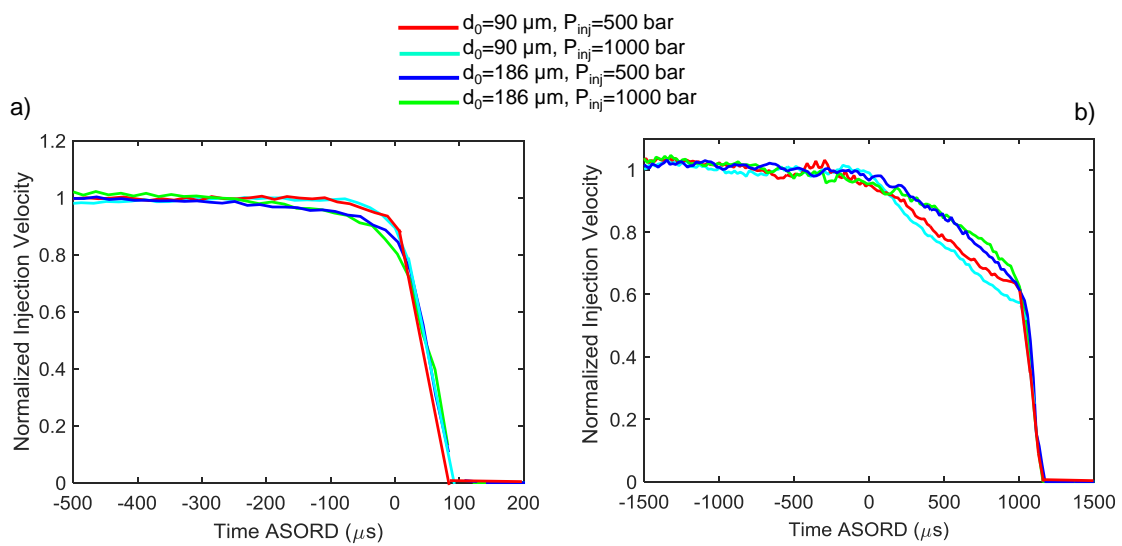
Figure 41: Normalized injection velocity profiles aligned by the end-of-injection transient for a) fast ramp-down profiles and b) slow ramp-down profiles. Steady injection velocities are 515 m/s and 330 m/s for injections pressures of 1000 bar and 500 bar, respectively.

CHAPTER V

COMBUSTION BEHAVIOR AFTER END-OF-INJECTION

Now that the flow of fuel through the injector orifice, both during steady injection and during transients, has been sufficiently characterized, the effects of end-of-injection transients on combustion observables can be assessed. Many of the experimental results presented in this section have been published in previous works by the author and will be shown here for posterity [52].

5.1   Interpretation of Signals

The ECN community has put forth many guidelines for measurement and image processing techniques regarding common diesel spray flame metrics, such as flame lift-off length, ignition delay, etc, but no such guidelines exist for combustion recession. Combustion recession presents unique measurement and image processing issues, which this section is designed to address.

5.1.1   OH* Chemiluminescence

A sequence of OH* chemiluminescence images is shown in Figure 42 that emphasizes the low intensity signal during combustion recession. The conditions for this figure are $T_a = 900$ K, $O_2 = 21\%$, $P_{inj} = 1000$ bar, $\rho_a = 22.8 \, \mathrm{kg \, m^{-3}}$, $d_0 = 90 \, \mu\mathrm{m}$ and fast RD profile. Each of the images shown has time, t, listed with respect to end-of-injection (EOI). The next section describes how the OH* chemiluminescence signal is discerned from the background using a thresholding technique.

Figure 43a shows the raw OH* chemiluminescence image at t = EOI + 0.37 ms but now with the intensity scaled such that the low combustion recession signal is emphasized. To minimize the noise in this image, the raw image is median filtered
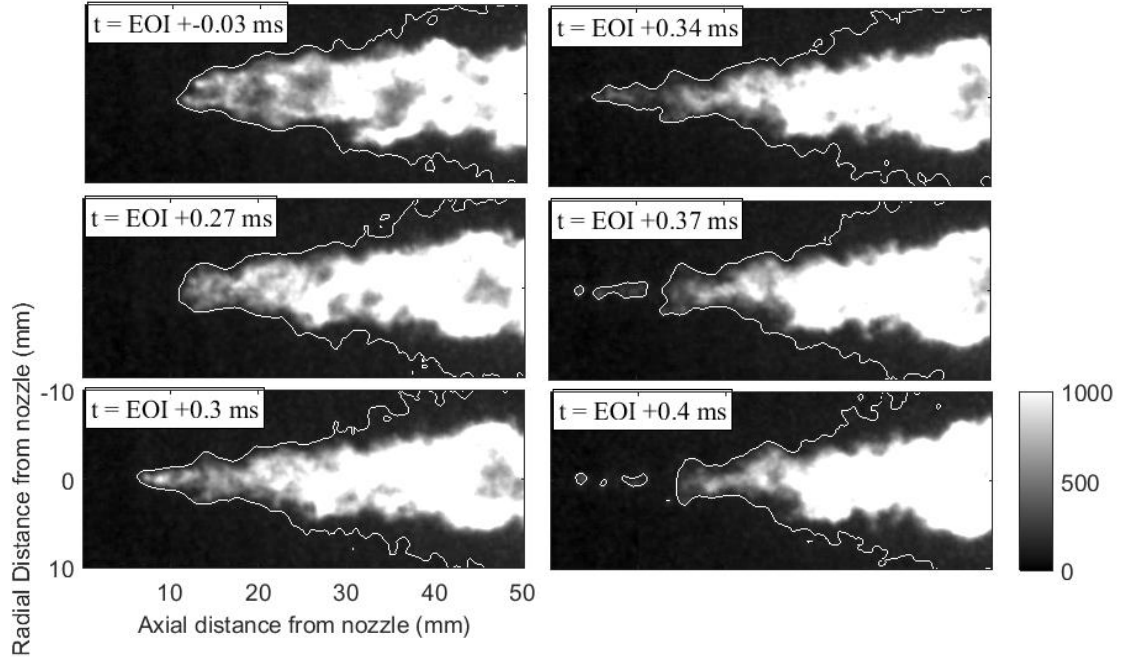
Figure 42: Sequence of OH* chemiluminescence images illustrating combustion recession behavior. Condition - $T_a = 900$ K, $O_2 = 21\%$, $P_{inj} = 1000$ bar, $\rho_a = 22.8\,\mathrm{kg\,m^{-3}}$, $d_0 = 90\,\mathrm{\mu m}$ and fast RD profile.

with an 8 x 8 filter in Figure 43b. Then, the boundary threshold was selected as 50% above the mean intensity in a 10 x 10 pixel array well outside of the reacting jet. This was done to ensure that the boundary threshold was sufficiently high to avoid the noisy background and yet low enough to capture the weak chemiluminescence signal during combustion recession. Further thoughts on this are given in Appendix C. The threshold was then applied and the resulting binarized image is shown in Figure 43c. Finally, the perimeter of this binarized image is overlaid onto the raw image in Figure 43d.

5.1.2 Schlieren

Next, image processing techniques for schlieren are outlined in detail and another sequence of images is shown in Figure 44. This sequence was obtained simultaneously with the OH* chemiluminescence images in Figure 42. Again, notice the white
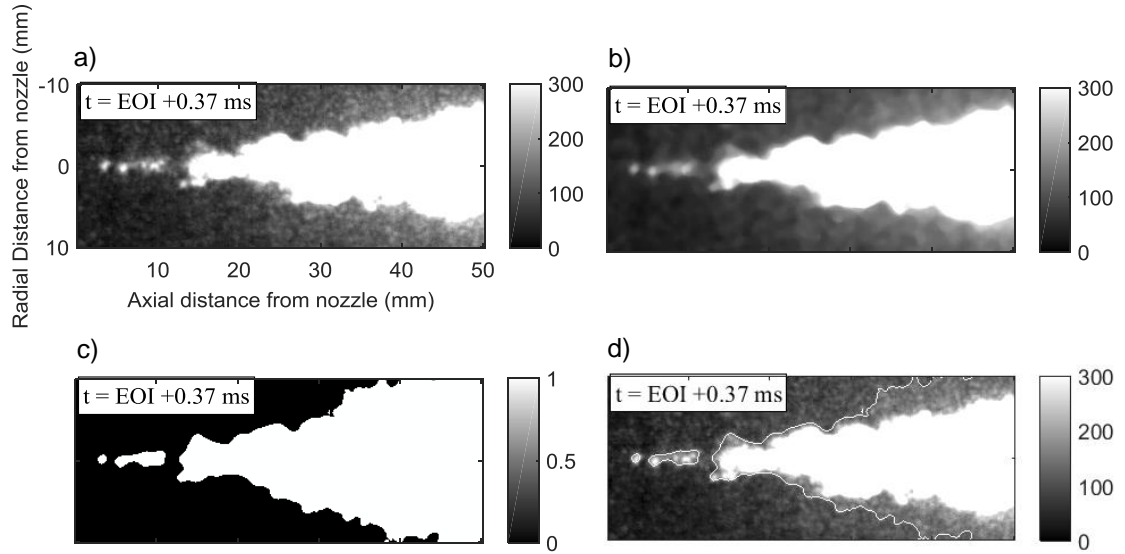
Figure 43: OH* chemiluminescence image illustrating boundary detection; a) raw image, b) median filtered with 8 x 8 filter, c) thresholded and binarized image, d) raw image with overlaid boundary. Condition - $T_a = 900$ K, $O_2 = 21\%$, $P_{inj} = 1000$ bar, $\rho_a = 22.8\,\mathrm{kg\,m^{-3}}$, $d_0 = 90\,\mu\mathrm{m}$ and fast RD profile.

boundary in each of the images, which is based on the morphological processing and thresholding techniques shown below in Figure 45.

To demonstrate the morphological processing techniques, a single instance in time was selected in Figure 45a. These techniques start by selecting a threshold to separate light from dark regions in Figure 45b (the threshold level will be described in more detail in the next section). Unfortunately though, significant index of refraction gradients still exist even though the spray chamber is designed to minimize temperature gradients at the windows and the schlieren optical arrangement has been optimized to reduce their effects. To help remove the unwanted background schlieren structures, a thresholded image before injection (see Figure 45c) that contains no spray but still retains these structures is used for background subtraction in Figure 45d. This technique also helps remove unwanted background structures that are there permanently, e.g. window/schlieren optics defects, dust, etc. Then, the image in Figure 45d undergoes a series of morphological operations resulting in the image presented in
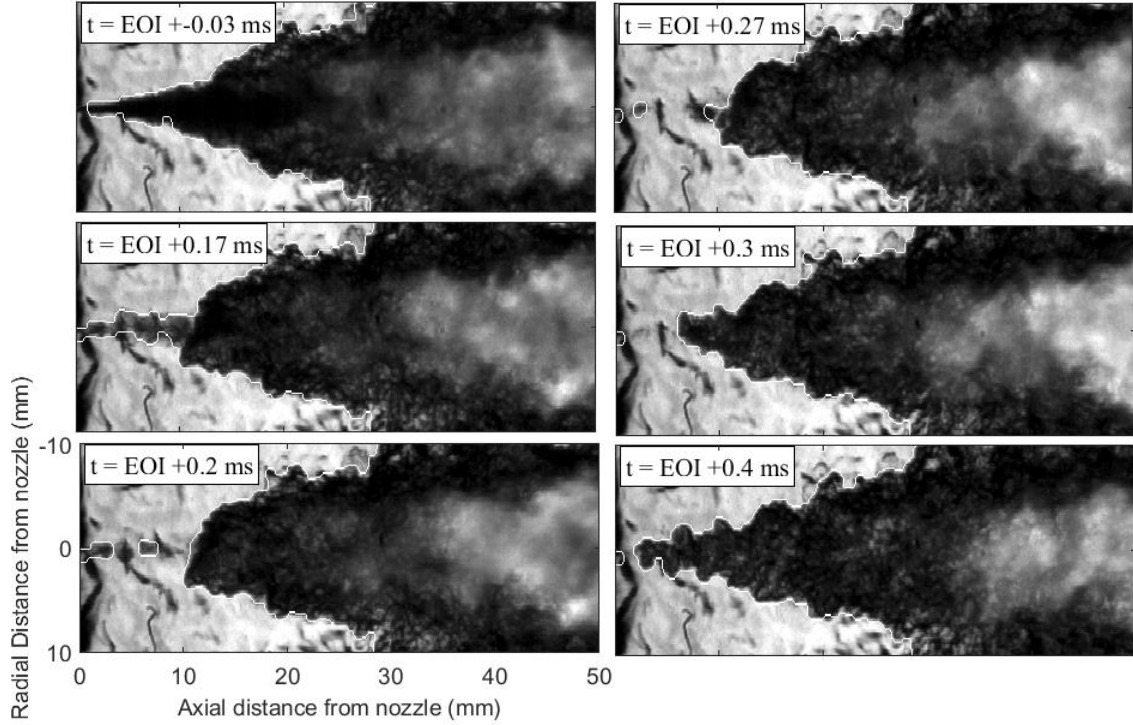
Figure 44: Sequence of schlieren images illustrating combustion recession behavior. Condition - $T_a = 900$ K, $O_2 = 21\%$, $P_{inj} = 1000$ bar, $\rho_a = 22.8\,\mathrm{kg\,m^{-3}}$, $d_0 = 90\,\mathrm{\mu m}$ and fast RD profile.

Figure 45e. The morphological processing begins by erosion with a 3 x 3 disk-shaped element, dilation with a 5 x 5 disk-shaped element, followed by closing with a 3 x 3 disk-shaped element. Lastly, all holes are filled. The boundary is then overlaid on top of the original schlieren image in Figure 45f.

The threshold technique for separating light from dark regions is illustrated in Figure 46. Two small 10 x 10 pixel regions are selected that represent the background (black box) and spray (white box) for all conditions tested. Then, the average of the pixels in these two regions are collected versus time with respect to end-of-injection. The ratio between the background and spray intensities can be leveraged to determine when the spray transitions from cold, unreacted fuel to hot combustion products. To illustrate this process, two different ambient conditions are shown in Figure 46. For the case that exhibits evidence of combustion recession in the OH* chemiluminescence
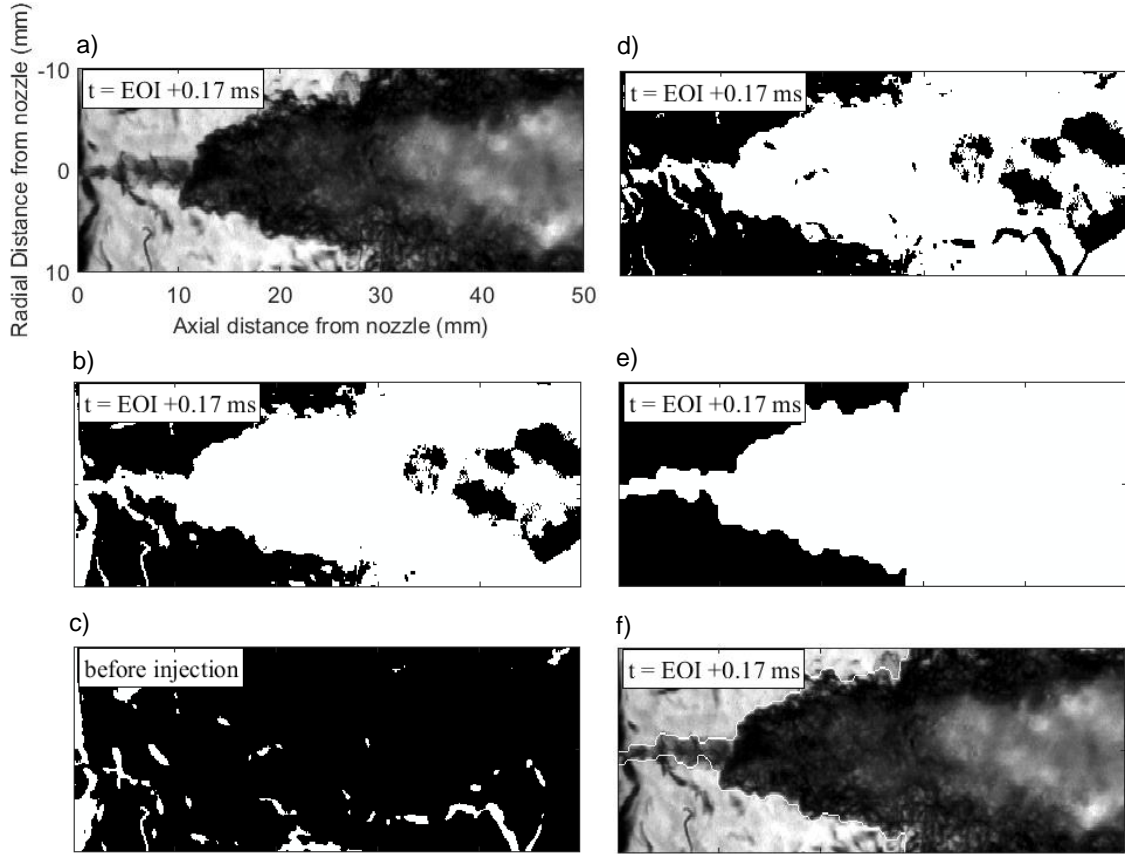
Figure 45: Schlieren image illustrating boundary detection; a) raw image, b) thresholded and binarized image, c) thresholded and binarized image before injection (to be used for background subtraction), d) background subtracted thresholded and binarized image, e) post-morphological processed image, f) raw image with overlaid boundary. Condition - $T_a = 900$ K, $O_2 = 21\%$, $P_{inj} = 1000$ bar, $\rho_a = 22.8\,\text{kg}\,\text{m}^{-3}$, $d_0 = 90\,\mu\text{m}$ and fast RD profile.

images (900 K, 21% O_2), the spray/background ratio increases shortly after end-of-injection. This is due to rapid vaporization of the spray and/or low-temperature heat release, which in turn lowers the local index of refraction gradients. Then, this ratio decreases back down to nearly the value it had prior to end-of-injection. This is evidence of high-temperature combustion products causing large index of refraction gradients. Moreover, the timing of this schlieren reappearance is nearly coincident with the timing of combustion recession in the OH* chemiluminescence images. For the condition that showed no evidence of combustion recession (800 K, 21% O_2) in the

OH* chemiluminescence images (not shown), the spray/background ratio increases indefinitely after end-of-injection indicating that mixtures upstream of the flame lift-off length have not undergone second-stage ignition and therefore no combustion products exist. Based on these observations, the threshold for separating light from dark regions is selected to be 60% of the spray/background ratio.
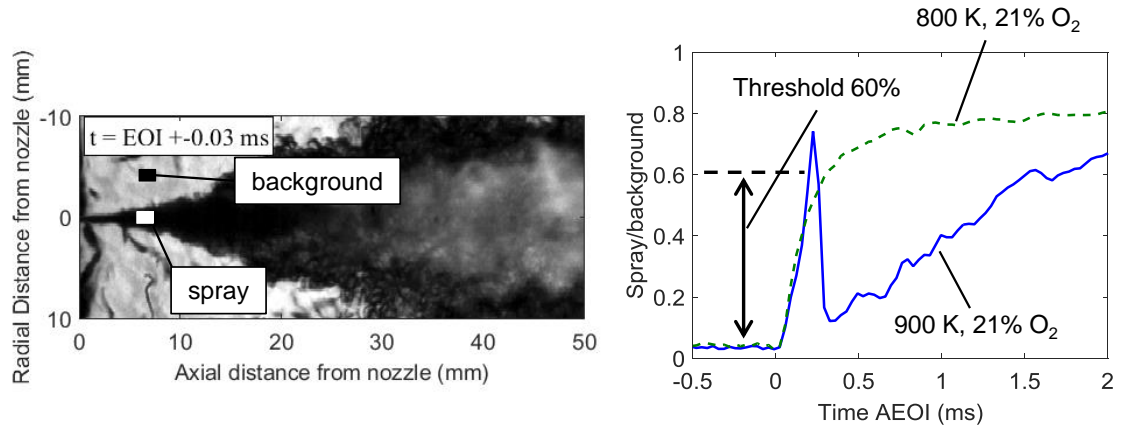
Figure 46: Illustration of threshold selection for separating light and dark regions in schlieren images.

5.1.3 Broadband Chemiluminescence

After ignition, soot luminosity creates a bright background that is non-uniform in space and time and complicates interpretation of the broadband chemiluminescence signal. To overcome this difficulty and improve signal-to-noise ratio, a dynamic background correction was performed. In Figure 47, the top image displays raw chemiluminescence/soot luminosity during quasi-steady state. The simultaneously acquired schlieren image was then used to define the boundary of the jet and to mask the broadband chemiluminescence/soot luminosity image. After applying the mask to the chemiluminescence/soot luminosity image, inward interpolation was performed to create an estimate of the background inside of the jet boundary, shown in the middle of Figure 47. Finally, the bottom image of Figure 47 was created by subtracting out this estimated background from the raw image at the top. Similar to the

94

procedure outlined in Chapter 2, a threshold of 30 counts again defined the border for second-stage ignition. Note that the quality of this methodology is dependent on the schlieren image and threshold for jet boundary detection, and uncertainties in the jet border can lead to inconsistencies in the estimated background level near the jet edge (see bottom right edge of center image in Figure 47). However, the method enables extraction of broadband chemiluminescence information for combustion recession that might otherwise be obscured with other background subtraction techniques. Unfortunately though, even with dynamic background correction, these images are unable to provide the very low light intensity of first-stage ignition as is commonly done prior to start of combustion. Lastly, this methodology does not remove other interference sources like Mie scatter from liquid droplets, which will be present in these images up to the point of end of injection.
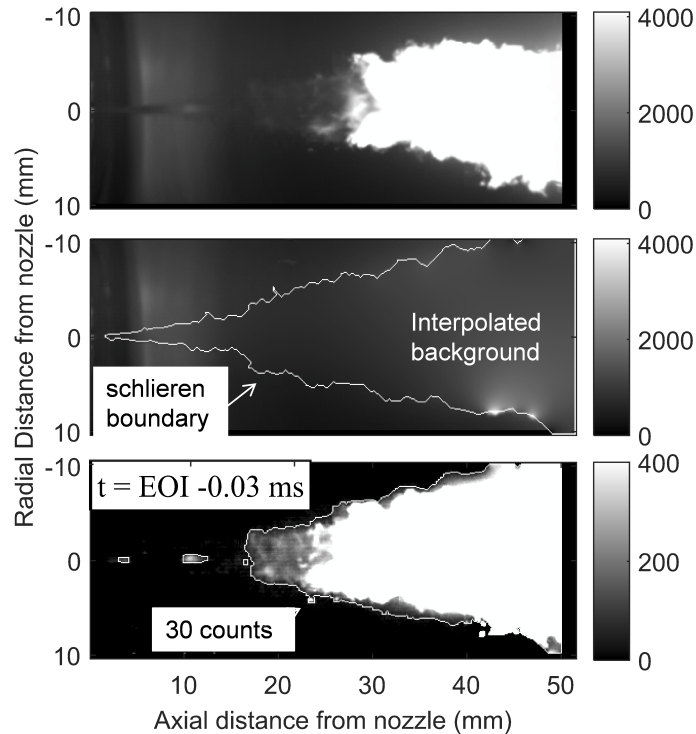
Figure 47: Dynamic background correction procedure. The top image is the raw broadband chemiluminescence/soot luminosity image, the middle is an estimated background image and the bottom image is after applying the background subtraction.

An example of a single combustion recession event is shown in Figure 48 to highlight the utility of the simultaneous diagnostics employed. This event is an example of partial combustion recession, where ignition occurs in pockets upstream of the flame lift-off length. This example is at the following condition: T_a = 900 K, O_2 = 15%, P_{inj} = 1000 bar, ρ_a = 22.8 kg m^{-3}, d_0 = 90 µm, and fast RD profile. The time evolution of the combustion recession process will be described and the reader is referred to Figure 48 (from left to right) for references to imaging of schlieren, OH* chemiluminescence, and broadband chemiluminescence/soot luminosity, respectively.

The first frame (t = EOI - 0.030 ms) of each image sequence in Figures 48 is just prior to the end-of-injection when fuel is still being injected. In addition to the intended signals, the broadband chemiluminescence/soot luminosity image also exhibits Mie scattering from the interaction between soot incandescence and liquid droplets up to ~14 mm from the nozzle. The instantaneous flame lift-off length is indicated by the chemiluminescence boundary ~16 mm downstream of the injector and by the rapid radial expansion in the schlieren image. No Mie scatter was measured in the broadband chemiluminescence/soot luminosity images 100 µs after end-of-injection (not shown). Kook et al. have shown that complete vaporization occurs in less than 100 µs after end-of-injection for the range of conditions in this work [102].

By t = EOI + 0.2 ms, portions of the jet in the schlieren image have begun to disappear, particularly just upstream of the flame lift-off length. Mixtures in this region have likely undergone first-stage ignition where the small amount of heat released during this phase of ignition brought local temperatures close to that of the ambient, hence the lack of refractive index gradients. Somewhat surprising is that even the core of the jet has disappeared, suggesting a nearly uniform radial distribution of reactivity. This disappearance is unlikely to be attributed to vaporization because even very fuel-lean gas-phase mixtures at the edges of a non-reacting jet, which are closer in composition and density to the ambient gases, are identifiable in the schlieren

images. Moreover, this region is expected to be reasonably fuel-rich and thus colder and denser than the ambient gases, which would exhibit substantial refractive index gradients. By t = EOI + 0.3 ms, the entire jet upstream of the flame lift-off length has disappeared and the lift-off length remains at the same axial location.

The flame lift-off length recedes to ∼12 mm from the nozzle by 0.47 ms after the end-of-injection in both the schlieren and OH* chemiluminescence images. At this time, a small ignition kernel is evident ∼7 mm downstream of the nozzle in the schlieren image. This kernel does not appear to register in either of the chemiluminescence images until shortly after when the kernel grows to appreciable size, suggesting that the schlieren imaging is more sensitive to the onset of second-stage ignition than chemiluminescence. Indeed, the schlieren signal requires only a mild density (temperature) gradient anywhere along the illumination path while the chemiluminescence signal requires sufficiently high local temperatures to electronically excite radical species and thus emit a photon. It is worth mentioning that all of the conditions in this work are not so dilute (all conditions are $O_2 \geq 10\%$) as to exhibit flameless combustion [103] and thus, chemiluminescence should be present for all mixtures that achieve complete second-stage ignition. Other reasons include the higher spatial resolution of the schlieren setup than either of the chemiluminescence setups. As time progresses past this point, schlieren imaging indicates that this separated region of hot combustion products merges with the slightly-recessed flame lift-off length to nearly fill the entire jet area. By t = 0.9 ms after the end of injection, soot-producing dribble is evident very close (∼5 mm) to the injector in the broadband chemiluminescence/soot luminosity image. Evidence that this signal is indeed soot is provided by the fact that the signal is bright (saturating the pixels), small, and short-lived (lasting only one frame).
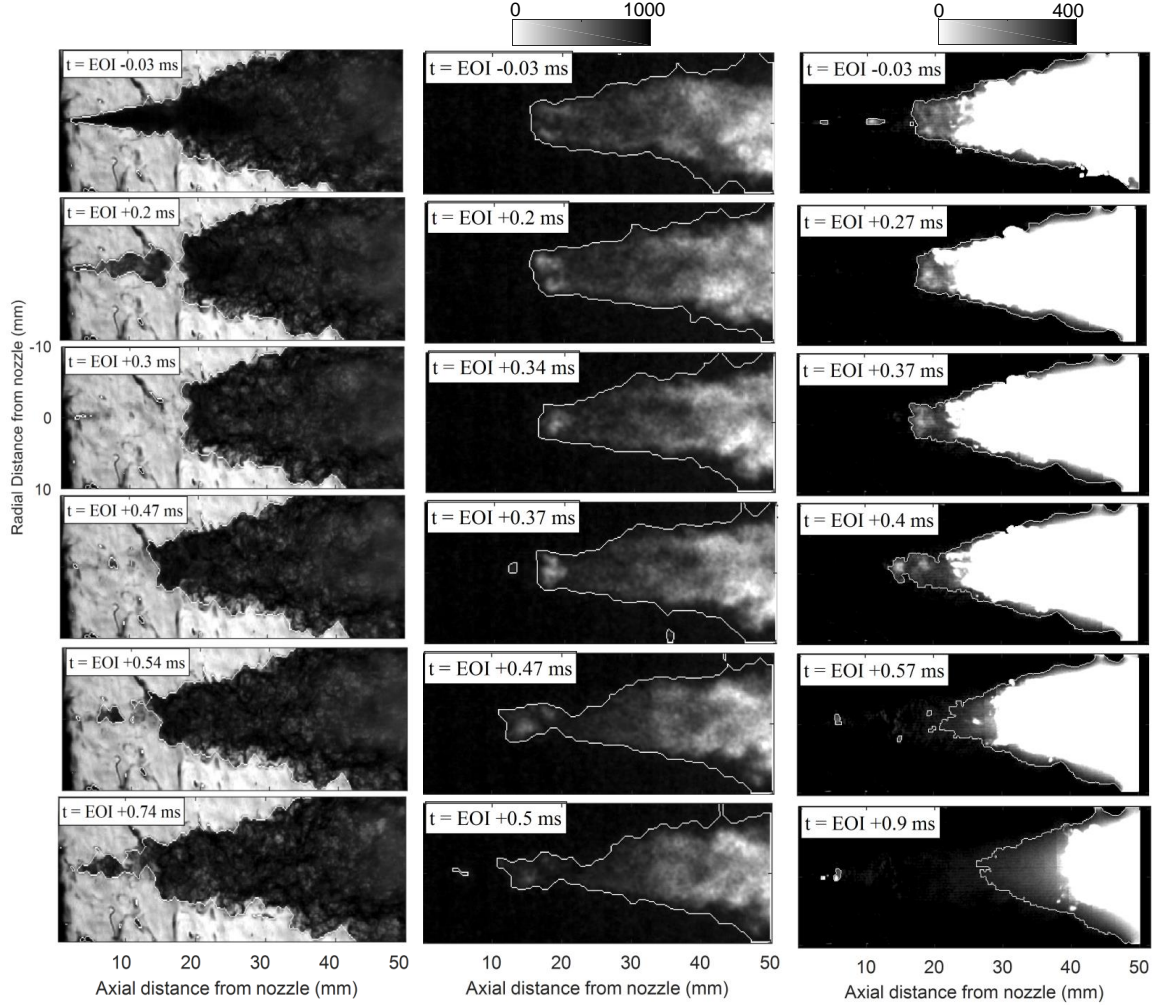
Figure 48: Sequence of schlieren, OH* chemiluminescence, and broadband chemiluminescence/soot luminosity images (left to right) demonstrating partial combustion recession. $T_a = 900$ K, $O_2 = 15\%$, $P_{inj} = 1000$ bar, $\rho_a = 22.8\,\mathrm{kg\,m^{-3}}$, $d_0 = 90\,\mu\mathrm{m}$, and fast RD profile.

5.2   Identification of Distinct Outcomes

5.2.1   Fast Ramp-Down

Essentially, OH* chemiluminescence, schlieren, broadband chemiluminescence and soot luminosity represent four different signals that can be used to decipher the physics of combustion recession. These signals are presented in Figure 49 where the first appearance of each signal at each axial location is shown with respect to end-of-injection. While each signal may persist at some axial location, a single value

is used to mark its first appearance at that axial location. Thus, the data are not multi-valued. This analysis was chosen instead of flame lift-off length analysis, where the upstream most position is found as a function of time, for several reasons. First, identification of separated ignition behaviors of combustion recession is more readily observed with the proposed analysis. Second, the proposed analysis enables a comparison of the overlap between the first appearance of schlieren and chemiluminescence signals, which can help differentiate between ignition and product mixing. Third, a more simple comparison with model predictions (shown later) is possible using the proposed analysis.

Also shown in Figure 49 are dashed lines that represent the location of the quasi-steady lifted flame. Note that the instantaneous lifted flame position is based on an ignition boundary threshold that is lower than the threshold used for the time-averaged flame lift-off length. Therefore, it may appear as though the jet does not ignite just upstream of the flame lift-off length but this is just an artifact of the threshold value for the steady-state flame lift-off length.

Figure 49 shows that by lowering the reactivity, combustion recession becomes less distinct and finally transitions to the absence of combustion recession altogether. The plots are grouped and labeled by the ambient temperature and oxygen concentration, with higher reactivity conditions (high temperature or oxygen concentration) on the left and lower reactivity conditions on the right. From these plots, qualitative interpretations of the observed combustion recession behavior were gathered using the following guidelines. If the appearance of the chemiluminescence signal showed a large, clear gap ($>2\,mm$) anywhere between the axial extents, then this condition was classified as partial combustion recession behavior. Alternatively, if there were no gaps and the chemiluminescence signal appeared continuous between the axial extents, then this condition was identified as complete combustion recession. Also, if there is no appearance of the chemiluminescence signal, then this condition

demonstrates the absence of combustion recession. Combustion recession will be characterized in a more quantitative manner, with a new metric, in a later section.

Decreasing ambient oxygen concentration from 21% to 10% at a constant ambient temperature of 900 K (upper row of plots in Figure 49), and decreasing ambient temperature from 900 K to 850 K at constant ambient oxygen concentration of 21% (left-most column of plots in Figure 49), have similar effects on the qualitative combustion recession behavior. The lack of chemiluminescence appearance at intermediate axial positions indicates separated pockets of ignition. Further lowering the temperature to 825 K or 800 K (lower row of plots in Figure 49), the lack of any chemiluminescence signal indicates the absence of combustion recession. While a schlieren signal is observed between 10 and 15 mm downstream of the injector for the 825 K condition, chemiluminescence is absent indicating that only a mild temperature gradient exists along the line-of-sight. Therefore, mixtures in this region have likely undergone partial oxidation but have not reached second-stage ignition. Soot-producing dribble is also observed for the 825 K and 800 K conditions and should not be considered part of combustion recession. Soot signals that are interpreted as stemming from dribble are labeled in each plot throughout Figure 49. These signals are interpreted as dribble since the signal appearance occurs at relatively long times after end-of-injection and/or after the observation of the combustion recession event.

Focusing attention on the overlap between schlieren and chemiluminescence signals for partial combustion recession events (900 K/15% O_2, 900 K/10% O_2, and 850 K/21% O_2), chemiluminescence signals show clear axial separation while schlieren imaging shows an eventual merging as time progresses. For instance, at 900 K and 15% O_2, no chemiluminescence is observed between 7 and 11 mm downstream from the nozzle while a schlieren signal is observed at later times. This is likely due to axial mixing of hot combustion products.
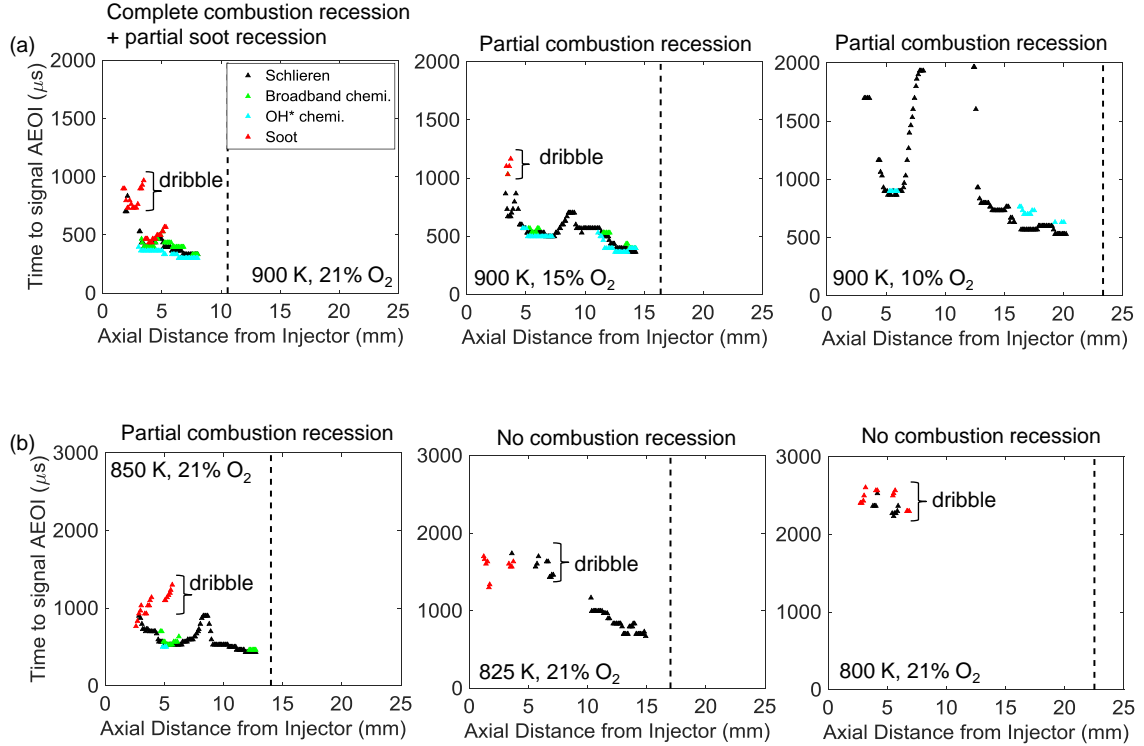
Figure 49: Experimental validation of distinct combustion recession behavior as conditions are transitioned from more reactive to less reactive (left to right). Times are measured after end-of-injection (AEOI) and the dotted line in each plot represents the flame lift-off location. $P_{inj} = 1000$ bar, $\rho_a = 22.8\,\mathrm{kg\,m^{-3}}$, $d_0 = 90\,\mu\mathrm{m}$, and fast RD profile.

5.2.2 Slow Ramp-Down

With control of the experimental ramp-down profile, measurements of combustion recession for the same conditions as shown in Figure 49 but with much longer ramp-down duration are given in Figure 50. The injection profile for these measurements is referred to as the "slow RD" profile in Figure 40a. As ambient oxygen concentration is reduced in Figure 50 (top row of plots), the behavior no longer transitions to partial combustion recession. Instead, near complete combustion recession is observed for all oxygen concentrations. For each case, combustion recession has been promoted with a longer end-of-injection transient. Similar behavior is observed as ambient temperature is reduced at constant oxygen concentration (lower row of plots). For example, at

850 K and 21% O_2 with fast ramp-down (Figure 49), combustion recession was found to be weak with separated ignition pockets while at the same conditions but with a much slower ramp-down (Figure 50), combustion recession became more prominent. However, at the lowest ambient temperature tested (800K) in Figure 50, the slow RD profile appears unable to promote complete combustion recession.
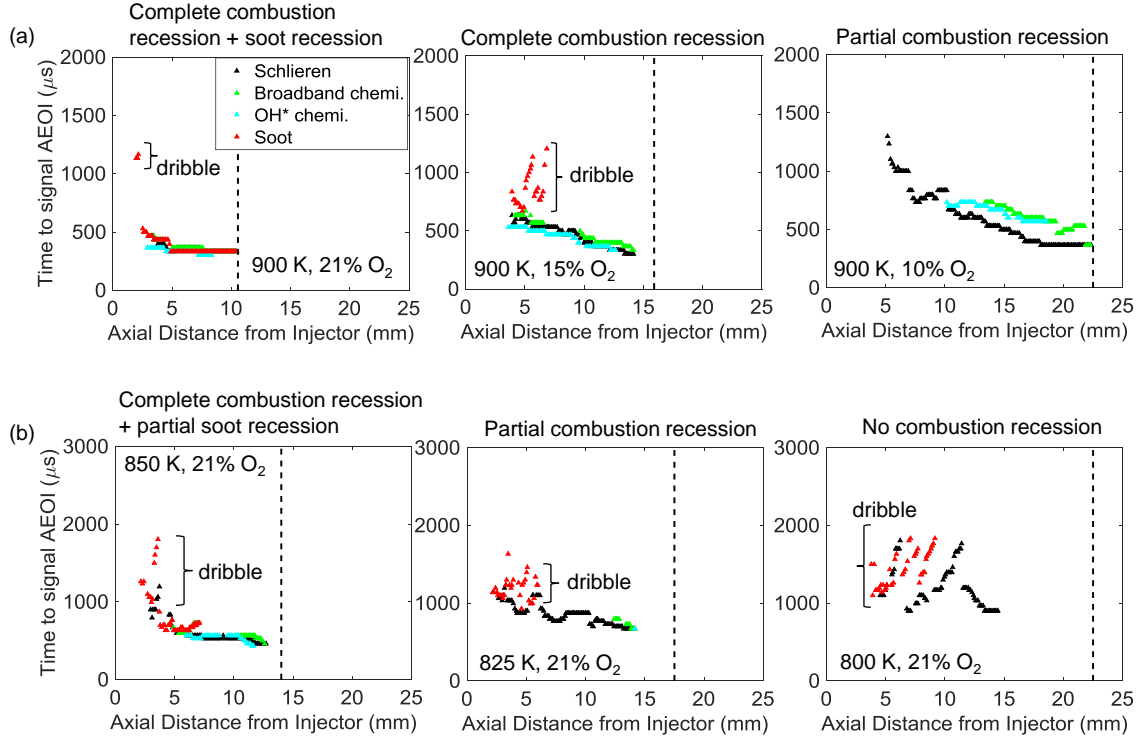
Figure 50: Experimental validation of distinct combustion recession behavior as conditions are transitioned from more reactive to less reactive (left to right). Times are measured after end-of-injection (AEOI) and the dotted line in each plot represents the flame lift-off location. $P_{inj} = 1000$ bar, $\rho_a = 22.8 \, \text{kg m}^{-3}$, $d_0 = 90 \, \mu\text{m}$, and slow RD profile.

5.3 Soot Observations

In addition to the schlieren and chemiluminescence signals, the experimental results in Figures 49 and 50 also provide a qualitative indication of soot. The number of markers for soot luminosity in each plot is not a measure of the amount of soot, however, but rather the markers are merely an indicator of when and where soot

is first formed (as indicated by a saturated luminosity signal that is substantially higher than measured chemiluminescence signals). Soot can appear in one or more distinct behaviors; it can spatially and temporally overlap with combustion recession, referred to as soot recession, and/or it can coincide with poorly-atomized fuel dribble following end-of-injection.

Before the soot observations in Figures 49 and 50 are addressed, validation is needed that the saturated luminosity signal is indeed an indicator of soot during the proposed soot recession event. Laser soot extinction measurements were conducted along the centerline of the spray at 5 mm downstream of the nozzle in Figure 51. Prior to the end of injection, the measured extinction (KL≈1.5) is due to liquid phase scattering. ECN measurements of liquid length have been reported around 10 mm from the nozzle, indicating that the beam is positioned (5 mm downstream of the nozzle) in a region of vaporizing droplets [57]. After end-of-injection, the measured KL quickly decreases as the probed volume contains only rapidly vaporizing droplets. Then, shortly thereafter, KL slightly increases for the 21% O_2 condition providing further evidence of soot recession. This can be compared with the 10% O_2 condition where no rise in KL (and hence no soot) is observed following end-of-injection, similar to what was observed in the luminosity imaging.

Now that the saturated luminosity signal is validated against a more quantitative diagnostic, the effects of ambient conditions and end-of-injection transients on soot near the nozzle is explored in Figures 49 and 50. At high reactivity conditions (900 K and 21% O_2) in Figure 49, soot recession is observed. For this condition, both soot and combustion complete their journey back towards the nozzle by 500 µs AEOI. Approximately 300 µs later, soot luminosity appears very close to the nozzle. This soot is suggested to be produced from poorly atomized fuel dribble following the end of injection.

For nearly all other conditions shown in Figure 49, soot recession does not occur

103
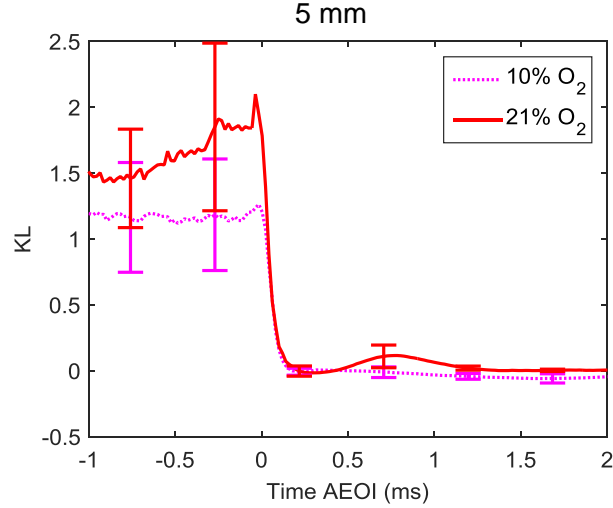
Figure 51: Validation of soot recession, as initially indicated by saturated luminosity, with laser soot extinction. Measurements were taken 5 mm downstream of the nozzle at the spray centerline. $T_a = 900$ K, $P_{inj} = 1000$ bar, $\rho_a = 22.8 \, \text{kg} \, \text{m}^{-3}$, $d_0 = 90 \, \mu\text{m}$, and fast RD profile.

but soot-producing dribble is still evident. Interestingly, no soot luminosity from dribble was observed at 900 K and 10% O_2 likely due to very slow soot formation kinetics for this low oxygen concentration. In this case, the dribbled fuel will mix with the ambient gases, evaporate, and then may form unburned hydrocarbons or soot precursors without forming mature soot.

Similar to combustion recession, it appears as though soot recession is also promoted with longer ramp-down duration. As seen in Figure 50 under 900 K and 21% O_2 ambient conditions, complete soot recession is evident by the overlap between soot and schlieren/chemiluminescence signals. Based on the understanding that a slow ramp-down process decreases the entrainment wave magnitude and reduces over-mixing compared to a fast end-of-injection transient, the slow RD injection profile appears to sustain rich enough fuel-air mixtures to form soot in the near-nozzle region. Similarly, under 850 K and 21% O_2 conditions, partial soot recession is now observed in addition to soot-producing dribble. Similar to the rapid end-of-injection case in Figure 49, no soot-producing dribble was observed for ambient conditions of

900 K and 10% O_2 in Figure 50. Lastly, only soot-producing dribble appears for all other ambient conditions in Figure 50.

From the results in Figures 49 and 50, it was determined that soot recession (and combustion recession) was promoted with a longer end-of-injection transient suggesting that there may be a trade-off between the consumption of near-nozzle unburned hydrocarbons and soot formation. Laser soot extinction measurements were performed at two axial locations, 8 and 40 mm downstream of the nozzle, to better address this concern in Figure 52. At 8 mm downstream of the nozzle, KL increases only slightly after end-of-injection for the slow RD profile compared to the fast RD profile. This result suggests that the promotion of soot recession with the slow RD profile increases near-nozzle soot by only a small amount. The impact of the slow RD profile on soot formation farther downstream of the nozzle (40 mm) is more drastic, however. Prior to end-of-injection, as well as the start of ramp-down for the slow RD profile (-1.1 ms AEOI), both measurements at 40 mm downstream of the nozzle indicate a KL of about one because the injection rate profiles are identical up until this point. After the start of ramp-down (-1.1 ms AEOI) for the slow RD profile, KL dramatically increases to approximately 2.5. KL likely increases during this period because the injection rate is slowly declining, increasing residence times of rich mixtures that will promote soot formation. These soot extinction results indicate that the slow RD profile produces a small amount of near-nozzle soot (due to soot recession) while soot formation in downstream portions of the jet can be rather high.

While limited quantitative soot data is available for these experiments, the saturated luminosity images (taken for all conditions) provide a wealth of qualitative information. Shown in Figure 53 are time histories of the soot length for a variety of conditions. Soot length is defined here as the axial distance from the nozzle to the first indication of soot, neglecting soot recession and sooting dribble. In other words, the soot length is only concerned with the soot behavior downstream of the lift-off
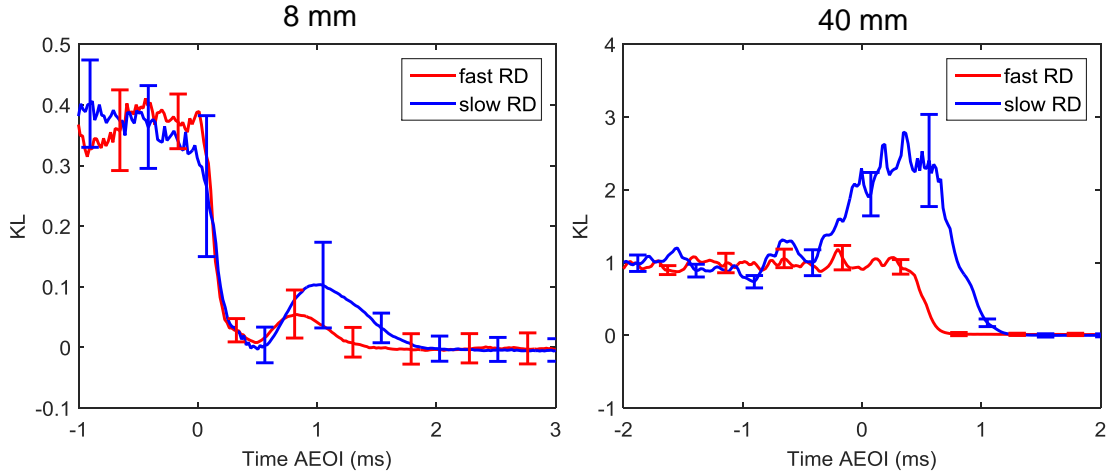
Figure 52: Laser soot extinction along the centerline of the spray. Measurements were taken 8 mm and 40 mm downstream of the nozzle at the spray centerline. $T_a = 900$ K, $O_2 = 15\%$, $P_{inj} = 1000$ bar, $\rho_a = 22.8\,\mathrm{kg\,m^{-3}}$, $d_0 = 90\,\mathrm{\mu m}$.

length.

A few observations regarding the soot length are worth noting. For nearly all of the conditions shown in Figure 53 the soot length slowly advances towards the nozzle prior to end-of-injection for the slow RD injection profile. The soot lengths for each ramp-down profile are nearly the same prior to the start-of-ramp-down for the slow RD profile, which begins at -1.1 ms AEOI. These results show that soot is formed closer to the nozzle as the injection velocity decreases during the first phase of ramp-down for the slow RD profile. Evidence of soot forming closer to the nozzle for a given condition suggests a greater level of soot because soot is generally formed at high equivalence ratios and that equivalence ratios are higher closer to the nozzle. Indeed, in Figure 52, KL increased dramatically at 40 mm downstream of the nozzle for the slow RD profile. Even for a case that is essentially non-sooting, 900 K/10% O_2/fast RD, the slow RD profile can create conditions that favor the formation of soot, suggesting that the end-of-injection transient is an important factor to consider for the formation of soot (and not just oxidation).
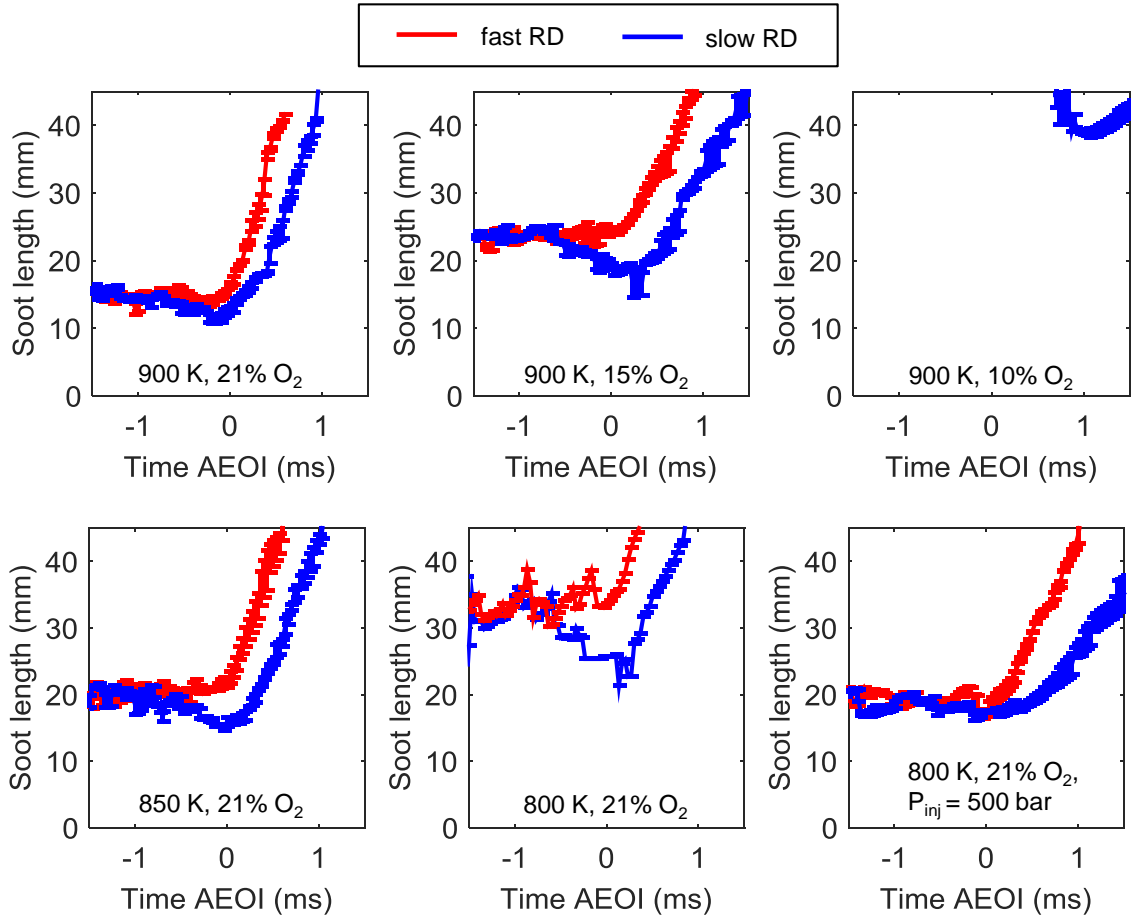
Figure 53: Soot length - axial distance from the nozzle to the first indication of soot (neglecting soot recession and sooting dribble). $P_{inj} = 1000$ bar, $\rho_a = 22.8 \, \text{kg m}^{-3}$, $d_0 = 90 \, \mu\text{m}$.

5.4 Flame Lift-off Behavior

Perhaps a more common way of analyzing the behavior of diesel spray flames is by tracking the instantaneous flame lift-off length with time, shown in Figure 54. This figure reveals an interesting comparison with the soot length results shown above in Figure 53. Prior to end-of-injection, the soot length responded very quickly to the change of injection velocity during the controlled, pressure-modulated phase of ramp-down whereas the flame lift-off length appears not to respond at all to this phase of ramp-down. The majority of the cases in Figure 53 show that the soot length decreases at nearly the same instant as the injection velocity begins to decrease at -1.1

ms AEOI. However, none of the corresponding cases in Figure 54 show that the FLOL responds in a similar fashion to the soot length. It isn't until after end-of-injection that the FLOL responds at all. Many researchers have coupled the observations of FLOL to sooting propensity, in that shorter FLOL generally leads to greater levels of soot, but these results suggest a decoupling as injection transients are brought into the picture.
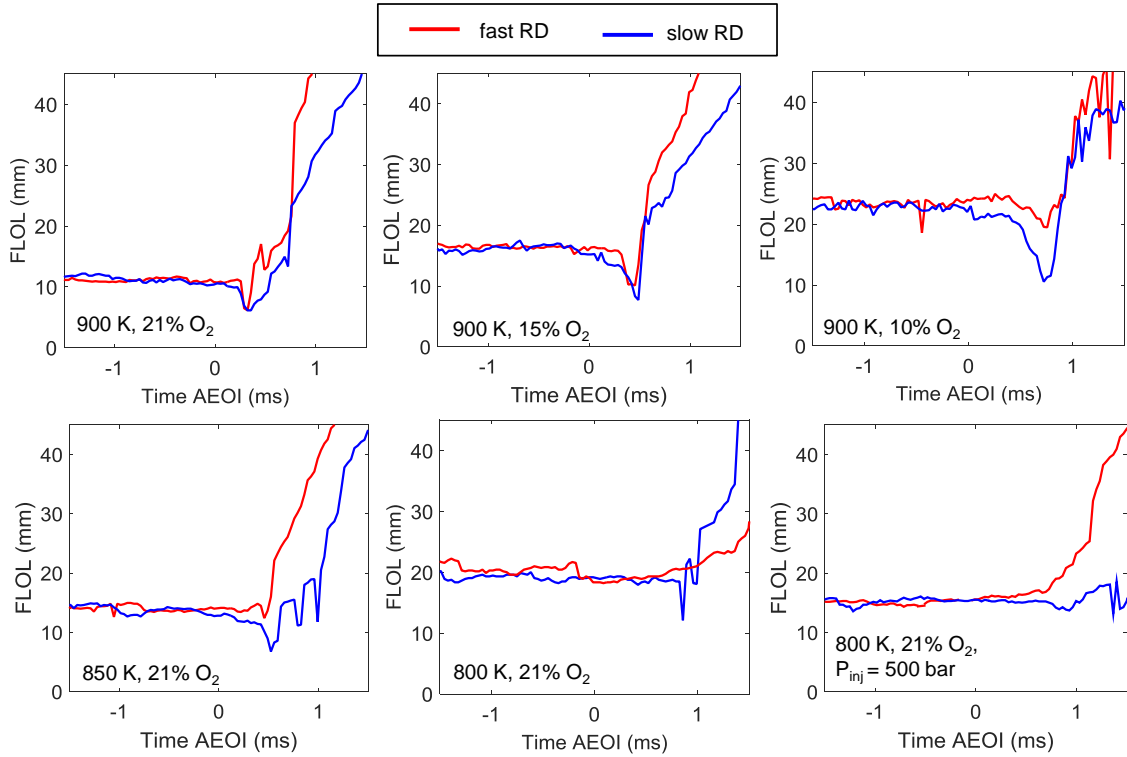
Figure 54: Time evolution of ensemble-averaged flame lift-off length (FLOL). $P_{inj} = 1000$ bar, $\rho_a = 22.8 \, \text{kg m}^{-3}$, $d_0 = 90 \, \mu\text{m}$.

If we subscribe to the idea that flame lift-off physics are dominated by autoignition processes, we would expect that the flame lift-off length adapts quickly to decreases of injection pressure. For instance, consider the 15% O_2 condition where the FLOL is approximately 16.5 mm prior to the ramp-down (the injection pressure is steady at 1000 bar). After the start of ramp-down, the injection pressure decreases to approximately 500 bar in 1.1 ms. Measurements at steady injection of 500 bar reveal that

FLOL=12.5 mm and if ignition processes are controlling flame lift-off, FLOL should decrease to approximately 12.5 mm by the end of the pressure-modulated phase of ramp-down. But, this behavior is not observed in Figure 54. These results may be further evidence that flame lift-off physics are heavily influenced by a combustion product reservoir that surrounds the core of the jet and stabilizes the reaction zone, originally proposed by Pickett et al. [35]. This finding has implications for control of the flame lift-off length via injection rate-shaping, assuming that this combustion metric is desirable to control. The long response times of the FLOL, longer than the imaging techniques were able to measure and longer than practical engine timescales, may limit the ability of injection rate-shaping strategies to control flame lift-off. However, much faster response times for soot length were observed, suggesting that injection rate-shaping indeed does have practical applications for control of emissions.

CHAPTER VI

REGRESSION, REDUCED-ORDER MODELING AND SCALING

The measurements and analysis in Chapter 5 identified distinct spray flame behavior following the end of injection. Particular attention was focused on the region upstream of the flame lift-off length. The above analysis has shown that the transition between combustion recession behavior can occur gradually as conditions are varied from more to less reactive. In this chapter, we will explore a new metric to quantify combustion recession and therefore define each regime. We will also explore the newly developed reduced-order model and compare its predictions with measurements. Lastly, the measurements and reduced-order model predictions will be used to develop a scaling approach for the prediction of combustion recession and its different regimes. Many of the experimental and numerical results presented in this section have been published in previous work by the author and will be shown here for posterity [52].

6.1 Combustion Recession Metric

Because the combustion recession process can appear as distinct pockets of ignition, a transient lift-off length analysis that follows the recession of the upstream-most ignition zone after EOI is not likely to yield a very meaningful descriptor of the process. Instead, combustion recession is quantified with a new parameter, R, which uses the OH* chemiluminescence boundary projected onto the axial dimension for all times after end-of-injection, as illustrated in Figure 55. At a condition of intermediate reactivity ($T_a = 900$ K, $O_2 = 15\%$, $\rho_a = 22.8\,\mathrm{kg\,m^{-3}}$, $P_{inj} = 1000$ bar, and $d_0 = 90\,\mathrm{\mu m}$) with a fast ramp-down injection profile, Figure 55 shows a snapshot in time at t =
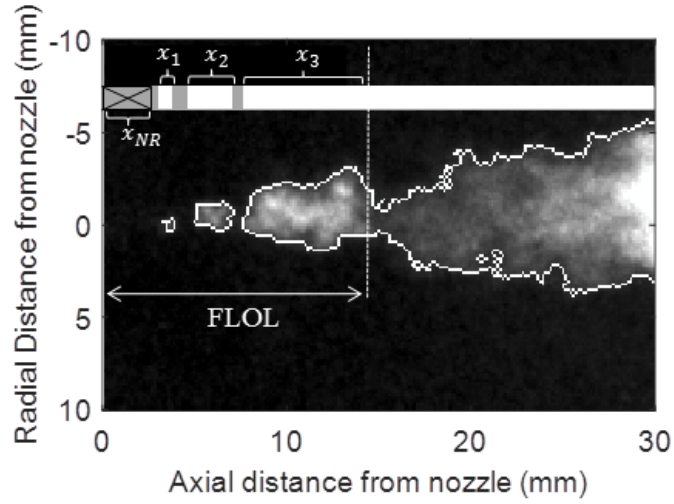
Figure 55: Illustration of combustion recession metric - line-of-sight integrated OH* signal is projected onto axial dimension. T_a = 900 K, O_2 = 15%, P_{inj} = 1000 bar, ρ_a = 22.8 kg m^{-3}, d_0 = 90 µm, fast RD profile.

EOI + 0.5 ms where distinct regions of the jet upstream of the FLOL never exhibit measurable chemiluminescence even for long times after the end of injection. This is an example of partial combustion recession, where localized regions are likely over-mixed beyond the point of ignition. Towards the top of Figure 55 is a colored bar that represents the chemiluminescence boundary projected onto the axial dimension. White regions denote measurable chemiluminescence at that axial position while gray indicates the absence of chemiluminescence. Within the first few millimeters from the nozzle exit, ignition pockets are difficult to experimentally observe. This is due to insufficient imaging resolution of the spray/jet in this region. This region, x_{NR}, is estimated to be approximately 3 mm in length from the nozzle exit. Without accounting for x_{NR}, R may be incorrectly skewed towards lower values.

For each injection, the projected boundary of chemiluminescence is collected for all times after the end of injection to create the combustion recession metric, R, which represents the ignited fraction upstream of the steady flame lift-off length after end-of-injection:

$$R = \frac{x_R}{FLOL - x_{NR}}. \tag{41}$$

The recessed flame length, x_R, is the summation of the axial length of all distinct ignition pockets, x_i.

$$x_R = \sum_{i=x_{NR}}^{FLOL} x_i. \tag{42}$$

The recessed flame length is normalized in this way to yield direct comparisons to other conditions that have longer or shorter steady flame lift-off lengths. Thus, each combustion recession regime (not including soot recession) is identified with the aid of R.

To provide an indication of combustion recession repeatability, i.e. shot-to-shot variation, the probability of ignition at each axial position is shown in Figure 56. Probabilities of the combustion recession process are shown for conditions that are varied from more reactive (21% O_2) to less reactive (10% O_2) at T_a = 915 K, ρ_a = 22.8 kg m^{-3}, P_{inj} = 1000 bar, and d_0 = 90 µm, with a fast ramp-down injection profile. The quasi-steady flame lift-off length is indicated with a dashed line. Twenty injections for each ambient oxygen concentration were used to obtain the probability of ignition at each axial position, along with the ensemble-averaged combustion recession metric, $\langle R \rangle$. At 21% O_2, $\langle R \rangle = 0.99 \pm 0.01$ and there is nearly 100% probability that an ignition pocket will appear everywhere upstream of the flame lift-off length after the end of injection. At 15% O_2, $\langle R \rangle = 0.91 \pm 0.09$ and ignition pocket probabilities drop down to a range of 60-95%, while at 10% O_2 $\langle R \rangle = 0.55 \pm 0.04$ and the range of probabilities is as low as 10-50%.

6.2 *Regression of Combustion Recession*

A standard least squares regression was performed for the ensemble average of the combustion recession metric, $\langle R \rangle$, shown in Eq. 43. Only a few important interactions,
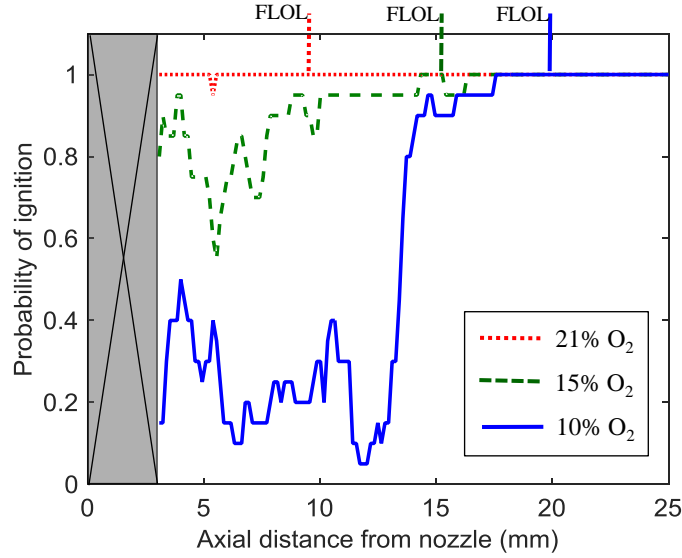
Figure 56: Combustion recession probabilities as ambient oxygen concentration is varied. $T_a = 915$ K, $P_{inj} = 1000$ bar, $\rho_a = 22.8\,\mathrm{kg\,m^{-3}}$, $d_0 = 90\,\mu\mathrm{m}$, fast RD profile.

namely $\rho_a * T_a, \rho_a * O_2, \rho_a * d_0$, were retained in the model due to their high t-ratio. As observed in Figure 57a, the actual-by-predicted plot shows reasonable agreement between the model and experimental data and is supported by an adjusted coefficient of determination value of 0.85. Shown in Figure 57b is a tornado plot of the sorted t-ratios indicating the most influential factors in the regression (from top to bottom). The most influential parameters are the ambient thermodynamic conditions, i.e. density, temperature, and oxygen concentration, followed by nozzle orifice diameter. These trends align well with the most influential parameters for attaining low-temperature combustion. The ramp-down profile also has a noticeable impact, suggesting that combustion recession can be controlled in the low-temperature combustion regime via injection rate-shaping. The injection pressure, however, does not appear to have a strong impact on combustion recession, which may be in part due to the low range of injection pressures explored in this work.

113

$$\langle R \rangle = -0.3618 - 0.1686\rho_a + 3.014 \times 10^{-4}T_a + 0.4576O_2 + 6.372 \times 10^{-4}d_0$$

$$+1.998 \times 10^{-4}\rho_a T_a + \begin{cases} -0.0437, & RD\text{``}fast\text{''} \\ 0.0437, & RD\text{``}slow\text{''} \end{cases} + 0.1054\rho_a O_2 \quad (43)$$

$$+8.772 \times 10^{-5}\rho_a d_0 - 1.228 \times 10^{-4}P_{inj}$$

Because the factor RD profile is categorical, the regression cannot be used for ramp-down profiles that are different than the two used here. Also, the regression provides little to no physical insight into the combustion recession process and is unable to predict the combustion recession behavior for injectors that have a naturally slower, linear ramp-down. Multi-hole, commercial injectors for example, have demonstrated linear ramp-down profiles that last anywhere up to $\sim$400 µs [102].

The analysis and scaling methodology in the next section aims to correlate steady injection combustion observations (e.g., the flame lift-off length) and end-of-injection observations to combustion recession outcomes over a wide range of operating conditions, the results of which have potential to be applied to a wider class of injectors and injection strategies than those tested in this work. This scaling methodology will also extend current understanding of the controlling physics regarding combustion recession.

6.3 Reduced-Order Modeling of Combustion Recession

To better understand the interplay of the end-of-injection transient, the entrainment wave, and combustion recession, the mixing model of Musculus and Kattke [41] is employed. Since the normalized injection velocity profiles were nearly identical to one another, regardless of injection pressure and nozzle orifice diameter, each profile (fast and slow) is modeled in Figure 58 with only the most salient features of the measured injection velocity thereby neglecting the small-scale oscillations. This simplification will aid the analysis and scaling development, shown in a later section.
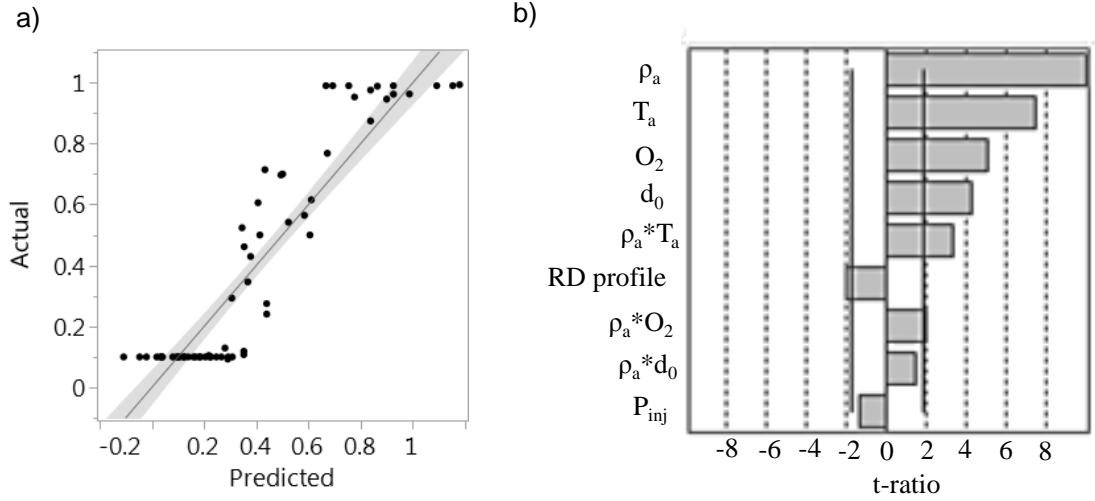
Figure 57: a) Actual-by-predicted plot for linear regression of ensemble averaged combustion recession metric, $\langle R \rangle$, using data from test matrix in Table 2; b) sorted parameter t-ratios for linear regression.

Figure 59 shows model-predicted vapor penetration curves overlaid on the $T_a = 900$ K, $O_2 = 15\%$, $P_{inj} = 1000$ bar, $\rho_a = 22.8\,\mathrm{kg\,m^{-3}}$, $d_0 = 90\,\mathrm{\mu m}$ condition in Figures 49 and 50. This overlay demonstrates the transit history of fuel parcels leaving the injector during the ramp-down period. Each penetration curve (shown as dashed magenta lines) has a time listed next to it that marks the release of the fuel parcel from the nozzle relative to the end of injection.

With the fast RD profile (Figure 59a), the model predicts that fuel parcels exiting the nozzle $-80\,\mathrm{\mu s}$ after end-of-injection penetrate past the flame lift-off location, FLOL, before combustion recession begins at $400\,\mathrm{\mu s}$ and therefore do not appear to participate directly in combustion recession. This is not to say that these fuel parcels' contribution to combustion recession is negligible. These fuel parcels could and likely undergo first-stage ignition upstream of the FLOL, releasing heat and creating a pool of reactive radicals, laying the groundwork for second-stage ignition of subsequent fuel parcels. Rather, these fuel parcels themselves do not reach second-stage ignition upstream of the FLOL and thus do not participate directly during the combustion
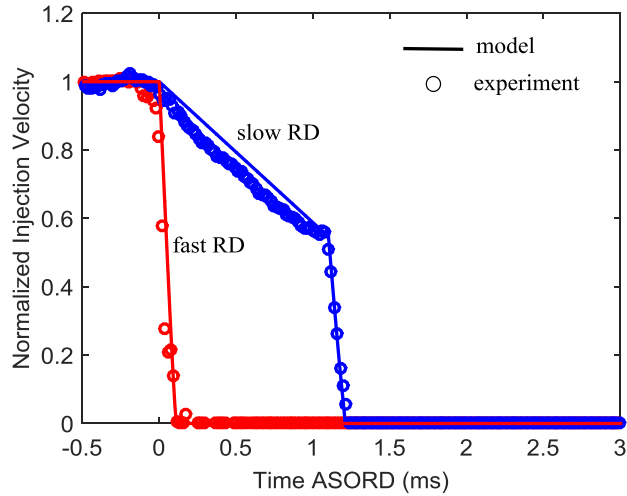
Figure 58: Measured normalized injection velocity profiles from Figure 41 along with input profiles to the model.

recession event. While this thesis contains no direct measurements to show that first-stage ignition does indeed precede combustion recession, due to the lack of a suitable diagnostic, the coupling between first-stage ignition and combustion recession has been demonstrated in the work by Skeen and coworkers [64].

Penetration curves for fuel parcels that exit the nozzle between $-80\,\mu s$ and $-40\,\mu s$ after the end of injection intersect with the chemiluminescence signals indicating that fuel injected during these times participates directly in combustion recession. However, fuel parcels that exit between $-40\,\mu s$ and $-25\,\mu s$ do not seem to ignite, indicated by the lack of chemiluminescence between 7 and 12 mm downstream of the nozzle. Overall though, the majority of fuel parcels released during the ramp-down process do not penetrate past the flame lift-off location and thus could participate in combustion recession. This could also mean that for conditions with no combustion recession, the majority of fuel injected during the ramp-down process ends up as unburned hydrocarbons. Predictions of unburned hydrocarbons will be shown in a later section.

Dissimilar to the fast RD profile, the penetration curves in Figure 59b for the slow

116

RD profile show that some of the fuel injected prior to needle-closing, between $-150\,\mu\mathrm{s}$ and $-100\,\mu\mathrm{s}$, participates directly in combustion recession. Recall that for the slow RD profile, the first-phase of ramp-down was controlled via pressure-modulation and the second phase was due to needle-closing while for the fast RD profile, the entire ramp-down was exclusively due to needle-closing. Even for the slow RD profile, most of the fuel that participates directly in combustion recession is injected during the needle-closing phase of ramp-down (between 0 and $-100\,\mu\mathrm{s}$ AEOI). This suggests that the more rapid, needle-closing phase of ramp-down is likely to control the behavior of combustion recession, rather than the slower, pressure-modulated phase.
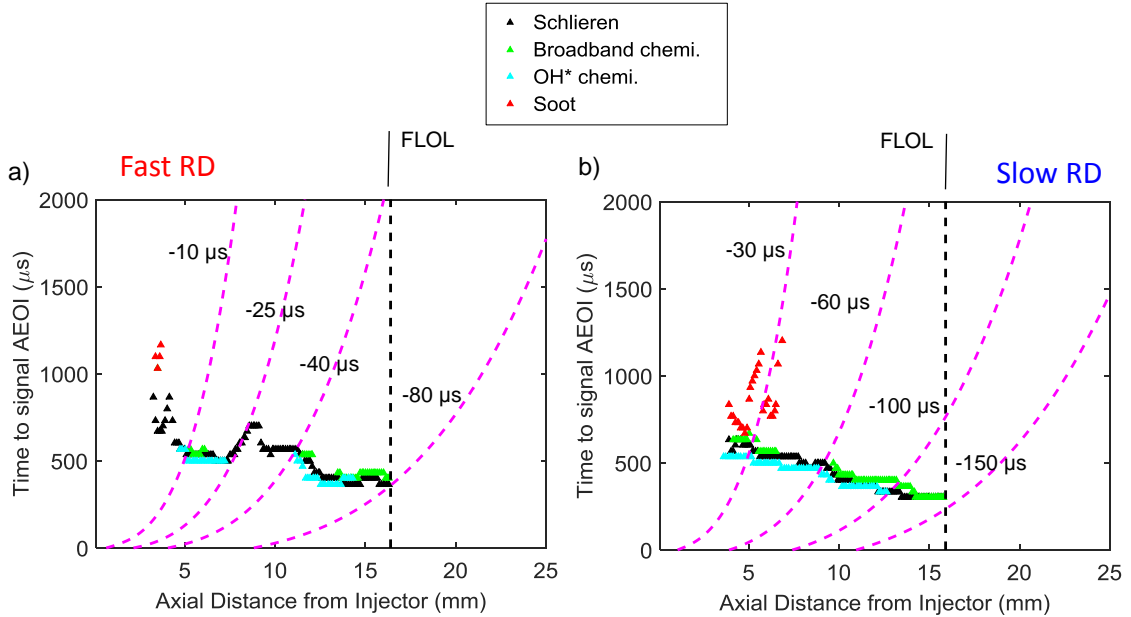
Figure 59: Vapor penetration predictions overlaid on combustion recession data for a) fast ramp-down profile and b) slow ramp-down profile. $T_a = 900$ K, $O_2 = 15\%$, $P_{inj} = 1000$ bar, $\rho_a = 22.8\,\mathrm{kg\,m^{-3}}$, $d_0 = 90\,\mu\mathrm{m}$.

The mixing model of Musculus and Kattke [41] is limited, however, with regard to understanding the effects of end-of-injection and the entrainment wave on combustion recession. To improve understanding of the complex interplay between these phenomena, the model proposed in this thesis couples chemical reactions to the mixing predictions. A brief validation of this model for predictions of combustion recession

is shown in Figure 60 where the combustion recession metric is compared with experimental measurements. Since the experimental data is projected onto the axial dimension, the 1-D modeling results and 1-D projected experimental data are well suited for comparison. In Figure 60, conditions were selected such that $\langle R \rangle$ transitions between high and low for each factor. The combustion recession metric was calculated in the same way for the 1-D model as for the experimental measurements, but using predictions of second-stage ignition. Second-stage ignition was identified as the instance in time and the location in space where the predicted local temperature rose above a particular threshold. In Figure 60, two different thresholds, threshold 1 = 1500 K and threshold 2 = 1400 K, are selected to evaluate the sensitivity of this definition on the validation. Based on these results, the model appears to perform very well, regardless of the particular definition used for defining regions of second-stage ignition although the agreement is better for threshold 2 = 1400 K.

Two cases were selected in Figure 61 that demonstrate the range of combustion recession behavior, for which temperature profiles at select instances in time show the coupling between end-of-injection processes and reacting mixtures. In Figure 61a, ambient temperatures are high (900 K) such that combustion recession is likely. Indeed, end-of-injection processes initiate combustion recession at 500 µs after end-of-injection and combustion recession completes its journey back towards the nozzle by 570 µs. End-of-injection processes also bring fuel-rich mixtures downstream of the FLOL, located at 11 mm downstream of the nozzle, towards stoichiometric conditions and thus combustion temperatures rise. Further entrainment with increasing time leans out these mixtures and lowers their temperature. At a lower ambient temperature (800K), compared to the previous case, no combustion recession is evident in Figure 61b, even for long times after end-of-injection. However, at the last time instance shown, near-nozzle mixtures have reached a temperature slightly higher than the ambient, ∼835 K, indicating that first-stage ignition has occurred to some degree.
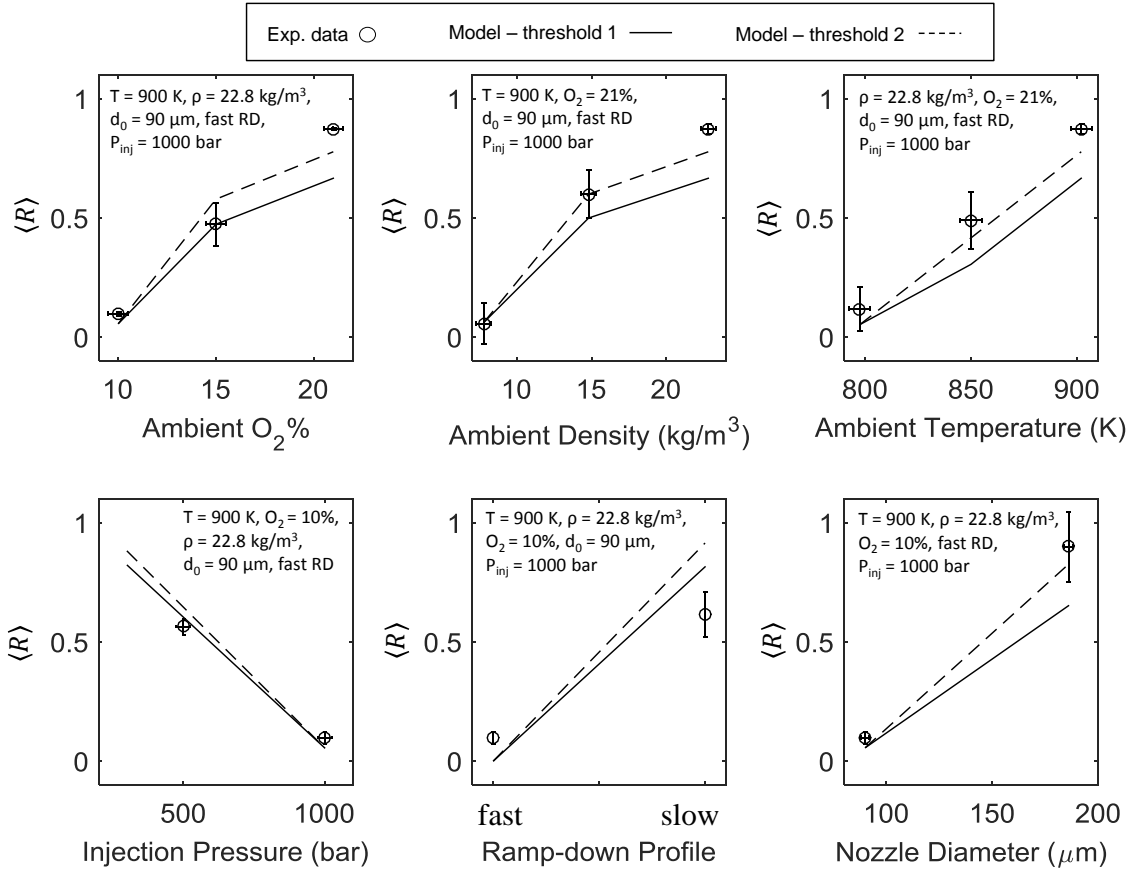
Figure 60: Validation of reduced-order model predictions for select cases such that $\langle R \rangle$ transitions between high and low for each factor.

Also note that the only effect of end-of-injection processes downstream of the FLOL, located at 22 mm downstream of the nozzle, is lowering of mixture temperatures. Since fuel-ambient mixtures are much leaner at 22 mm than 11 mm, the enhanced entrainment merely lowers the ratio below that of stoichiometric and thus combustion temperatures decrease.

6.3.1 Effect of End-of-Injection Transients

Now that model predictions of combustion recession transition behavior are validated, the model is used to further explore the effect of ramp-down duration. Observations from the experimental results in Figure 50 reveal that combustion recession was promoted with a longer ramp-down duration. For the time being, the focus will only
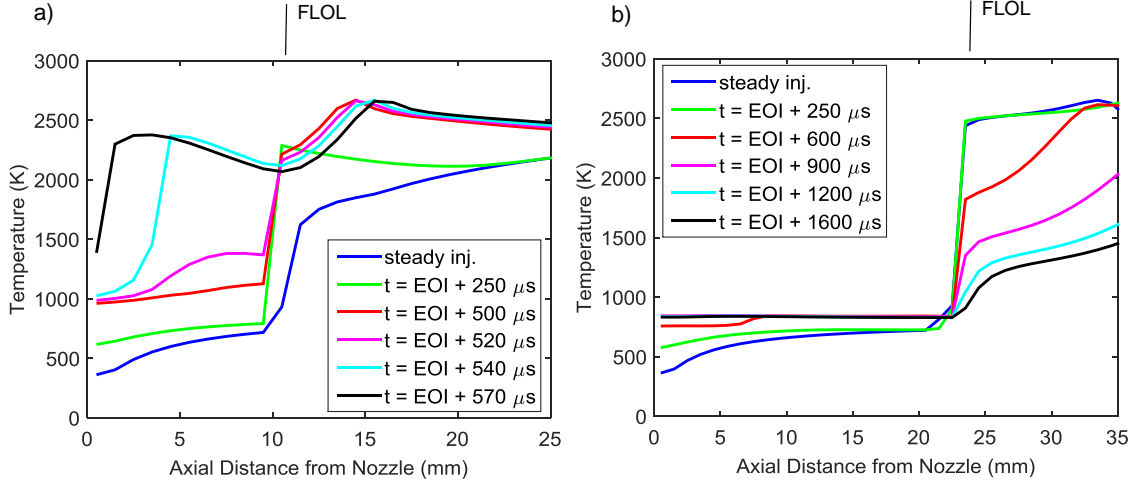
Figure 61: Combustion behavior after end-of-injection for conditions that exhibit a) complete combustion recession - $T_a = 900$ K and b) no combustion recession - $T_a = 800$ K. Other conditions are as follows: $O_2 = 21\%$, $P_{inj} = 1000$ bar, $\rho_a = 22.8 \, \text{kg m}^{-3}$, $d_0 = 90 \, \mu\text{m}$, fast RD profile.

be on a linear decrease of velocity, as opposed to the experiments with a two-phase ramp-down.

Figure 62b demonstrates that the model predicts promotion of combustion recession with longer ramp-down duration, as evidenced by the transition to complete ignition of upstream mixtures with increasing ramp-down duration. In the figure, positions where the 'time to ignition' approaches infinity indicate the absence of ignition. The conditions for this study are $T_a = 900$ K, $O_2 = 15\%$, $P_{inj} = 1000$ bar, $\rho_a = 22.8 \, \text{kg m}^{-3}$, and $d_0 = 90 \, \mu\text{m}$. In Figure 62b, very rapid end-of-injection transients (short ramp-down durations) exhibit either partial combustion recession or its absence. For example, a 50 µs ramp-down duration shows no sign of combustion recession, while a 75 µs ramp-down exhibits partial combustion recession. The model predicts complete combustion recession back towards the nozzle by ~500 µs AEOI for ramp-down durations greater than 100 µs. The model prediction for 100 µs RD is in reasonable agreement with the experimental result in Figure 49 (900 K, 15% O2), which also has a measured ramp-down duration of approximately 100 µs. While

there is some uncertainty in the experimentally measured ramp-down duration and the reduced-order model simplifies the physics considerably, the model does a good job at capturing the time required for combustion recession as well as the behavior, i.e. partial vs. complete.
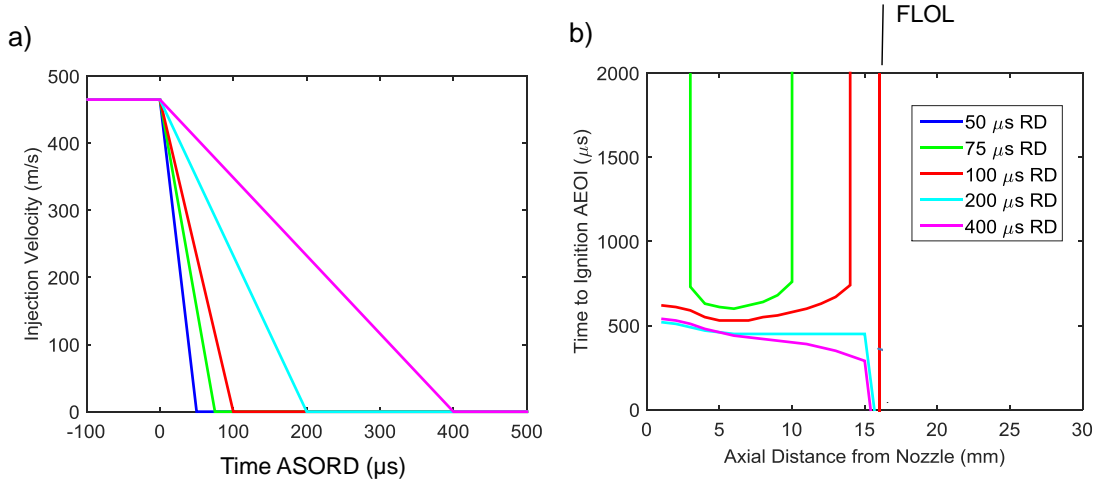
Figure 62: a) Injection velocity profile inputs to model and b) model predictions of the transition between combustion recession behavior by varying the ramp-down duration (RD). The conditions are as follows: $T_a = 900$ K, $O_2 = 15\%$, $P_{inj} = 1000$ bar, $\rho_a = 22.8 \, \text{kg m}^{-3}$, and $d_0 = 90 \, \mu\text{m}$.

6.3.1.1 Lagrangian Analysis

It was shown in Figure 59 that perhaps much of the fuel injected during the end-of-injection transient remains upstream of the FLOL and could directly participate in combustion recession. Lagrangian tracking of fuel parcels injected during the end-of-injection transient, or ramp-down, is implemented using the method of Yeung and Pope [104]. To summarize their method, Lagrangian tracking is achieved by numerically integrating each parcel's equation of motion,

$$\frac{\partial x^+(y,t)}{\partial t} = U^+(y,t), \tag{44}$$

where $x^+(y,t)$ and $U^+(y,t)$ denote the position and velocity at time t of the fluid parcel that originates from position y at time $t = 0$. The model is solved from an

121

Eulerian perspective, so the Lagrangian velocity $U^+(y,t)$ must be obtained from the Eulerian velocity $U(x,t)$ by

$$U^+(y,t) = U(x^+(y,t),t). \tag{45}$$

Each parcel's equation of motion is then solved using a second-order Runge-Kutta method. First, let t_j and t_{j+1} be successive time steps, where $t_{j+1} = t_j + \Delta t$. Then, to find an estimate x^* of the future position $x^+(t_{j+1})$ of the fluid parcel, a predictor step is used and is as follows,

$$x^* = x^+(t_j) + \Delta t U^+(t_j). \tag{46}$$

The corrector step then gives a better approximation,

$$x^+(t_{j+1}) = x^+(t_j) + 1/2\Delta t[U^+(t_j) + U(x^*,t_{j+1})]. \tag{47}$$

Note that to determine the fluid parcel velocity $U^+(t_j)$ and $U(x*,t_{j+1})$, interpolation from the Eulerian velocity field $U(x,t)$ is performed, which can be a significant source of uncertainty.

Two different ramp-down durations are investigated using this Lagrangian tracking method: 50 μs RD and 400 μs RD, which represent the extrema of ramp-down durations explored in Figure 62. Lagrangian tracking, or trajectories, are shown for a single fuel parcel released from the nozzle 75% between the start of ramp-down and the end of injection. Fuel parcels released before or after this point, but still during ramp-down, follow similar trajectories. Here, equivalence ratio, ϕ, is used in the non-reacting sense (similar to mixture fraction) and is defined as,

$$\phi = \phi_s \frac{\rho_f X_f}{\rho_a(1 - X_f)}, \tag{48}$$

where ϕ_s the stoichiometric mass ratio. Note that X_f is not altered by combustion in the model formulation, as outlined in Chapter 2 of this thesis.

Compared to the equivalence ratio trajectory for steady injection, a fuel parcel released during the very rapid 50 μs ramp-down follows a steeper trajectory, indicating higher entrainment. This fuel parcel is brought towards conditions that favor ignition in a shorter distance compared to a steady injection. For instance, the most reactive equivalence ratio (also known as the most reactive mixture fraction) is approximately 1.68 and it takes 7 mm to bring a fuel parcel to this equivalence ratio while it takes 24 mm at steady injection conditions.

A less rapid end-of-injection transient (400 μs RD) also shows a steeper equivalence ratio trajectory compared to steady injection. However, this trajectory is less steep compared to the 50 μs RD, indicating that entrainment has been limited. This fuel parcel is brought to the most reactive equivalence ratio at 10 mm downstream of the nozzle, which is between that of the more rapid ramp-down case and steady injection.
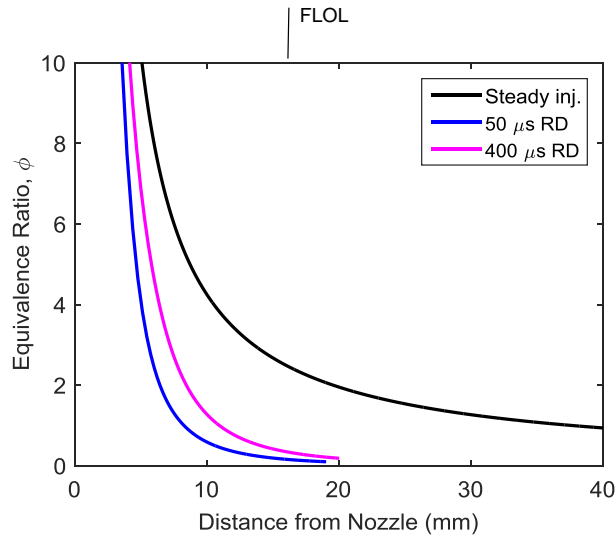
Figure 63: Equivalence ratio - Lagrangian tracking of fuel parcel released 75% between the start and end of ramp-down (38 μs ASORD for the 50 μs RD profile and 300 μs ASORD for the 400 μs RD profiles). a) 50 μs ramp-down profile and b) 400 μs ramp-down profile. The conditions are the same as in Figure 62.

The trajectory of each fuel parcel can be further understood by analyzing the species' evolution, shown in Figure 64. From the knowledge that the rapid 50 μs RD

profile brought the fuel parcel to the most reactive equivalence ratio in the shortest distance, it is expected that first-stage ignition would occur more upstream than for the slower 400 µs RD case. Indeed, first-stage ignition occurs at 8 mm for the 50 µs RD profile while it occurs at 9 mm for the 400 µs RD profile, as evidenced by the rapid creation and subsequent destruction of KHP. Heat release causes temperatures to rise during this phase of ignition to approximately 895 K and low-temperature kinetic pathways start to shift towards intermediate-temperature pathways.

As kinetic pathways shift towards the intermediate-temperature regime, heat release rates taper off and mixture temperatures rise more slowly. Immediately following first-stage ignition, radical pools of H_2O_2 and CH_2O are quickly formed. These radical pools persist until mixture temperatures reach closer to 1000 K, where H_2O_2 and CH_2O are quickly consumed, indicating the onset of second-stage ignition at 10 mm and 11 mm for the 400 µs RD and 50 µs RD cases, respectively. However, temperatures remain low (<1100 K) for the 50 µs RD profile suggesting failure of complete second-stage ignition. This is due to the fact that the fuel-air mixture is very lean, $\phi = 0.45$ (near the ignitable limit), at the onset of second-stage ignition at 11 mm from the nozzle exit. This fuel-air mixture has been *over-mixed*, resulting in a failed second-stage ignition. While complete, high-temperature ignition did not occur for this fuel-air mixture, unburned hydrocarbon (UHC) emissions appear to be low, < 1% of its initial value. On the other hand, CO emissions remain high because the mixture temperature only reaches 1100 K, well below the oxidation temperature of ~1500 K where $CO \Rightarrow CO_2$ at stoichiometric or lean conditions.

The effect of a more rapid ramp-down and enhanced entrainment is that first-stage ignition is reached at closer axial positions relative to the nozzle compared to less rapid ramp-down profiles. However, the dwell between first- and second-stage ignition is prolonged in space, e.g., from 8 mm to 11 mm for the 50 µs RD profile compared with 9 mm to 10 mm for the 400 µs RD profile. From closed homogeneous

reactor calculations, the dwell between first- and stage-ignition is longer in time for leaner mixtures. This is exactly the case for the 50 µs RD profile, where equivalence ratios are between 1.0 and 0.45 during the dwell between first- and second-stage ignition. In contradistinction, equivalence ratios are richer during the dwell, between 1.7 and 1.3, for the 400 µs RD profile. From this analysis, the impact of mixing on the dwell to first-stage ignition appears to be small but the impact on the dwell between first- and second-stage ignition appears to be significant. Below, the time evolution of an igniting fuel-air mixture with and without mixing is further investigated.
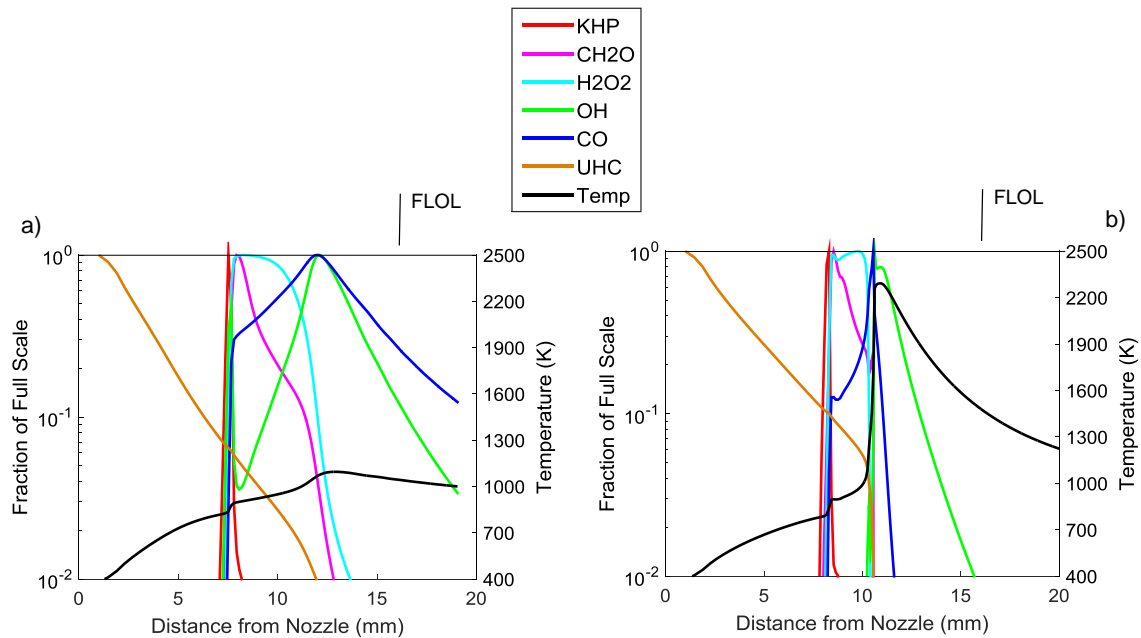
Figure 64: Species and temperature - Lagrangian tracking of fuel parcel released 75% between the start and end of ramp-down (38 µs ASORD for the 50 µs RD profile and 300 µs ASORD for the 400 µs RD profiles). The conditions are the same as in Figure 62.

Figure 65a is the same as Figure 64a except for the abscissa, which has been changed from a position coordinate to a time coordinate. The case in Figure 65a represents the effect of mixing on ignition processes while the closed homogeneous reactor simulation in Figure 65b represents a case without mixing. For the case without mixing, the mixture is initialized at its most reactive mixture fraction ($\phi = 1.68$) for which

the corresponding adiabatic mixture temperature is 811 K. This case may be thought of as the lower limit of the total ignition delay, without the added physical delay of mixing. Comparing the two cases, mixing appears to prolong every stage of ignition but the effect is much more pronounced for the dwell between first- and second-stage ignition. A competition between ignition and mixing processes appears to control the evolution of fuel injected during ramp-down, and thus combustion recession. Next, the competition between ignition and mixing timescales will be investigated.
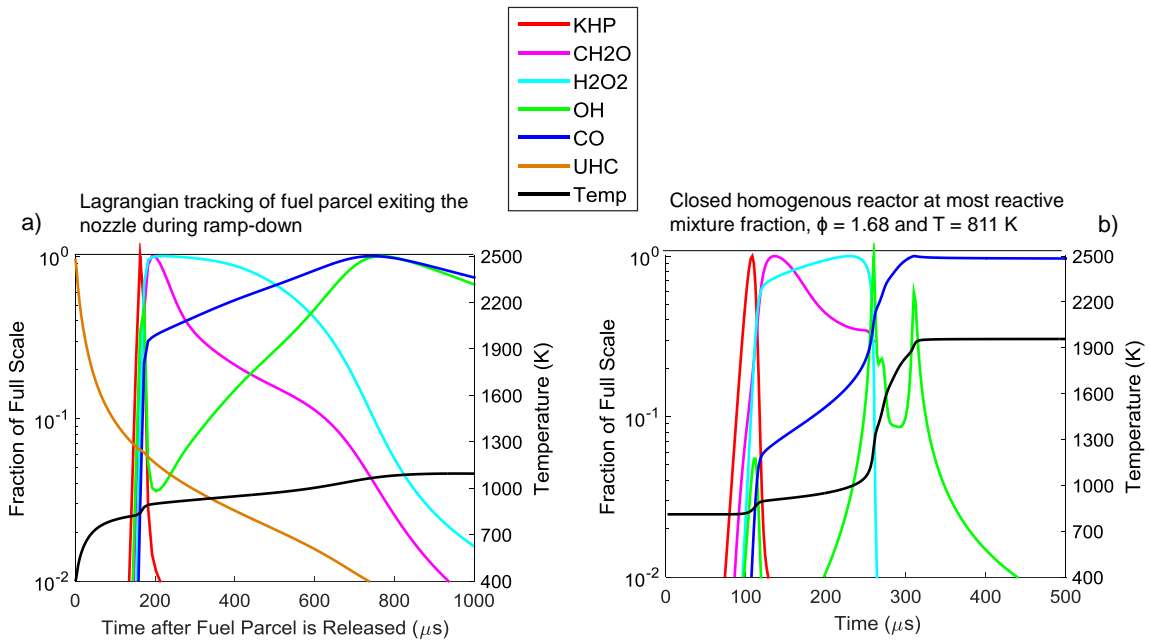
Figure 65: Comparison between time evolution of igniting mixtures a) with and b) without the added physical delay of mixing. a) Species and temperature - Lagrangian tracking of fuel parcel released 75% between the start and end of ramp-down (38 µs ASORD for the 50 µs RD profile. b) closed homogeneous reactor simulation of the most reactive mixture.

6.3.1.2   Timescale Analysis

The thesis presents a model that is essentially a transient plug flow reactor with entrainment, meaning that the local Damköhler number, Da, which can be defined as the ratio of the local residence time, τ_{res}, to the local (and instantaneous) ignition delay, τ_{ign}, can be used to better understand the role of coupled mixing-chemistry

processes on the outcome of combustion recession:

$$Da(x,t) = \frac{\tau_{res}(x,t)}{\tau_{ign}(x,t)} = \frac{\int_0^x \frac{dx}{U(x,t)}}{\tau_{ign}(x,t)}. \tag{49}$$

The quantities x, t, and U are the axial coordinate, the time coordinate and the cross-sectionally averaged axial velocity, respectively. The instantaneous ignition delay is the time delay to second-stage ignition for a particular mixture, wherever it is along its path to ignition. The mixture could contain radicals and will thus have a shorter instantaneous ignition delay than if the delay were based solely, for instance, on equivalence ratio. This instantaneous ignition delay will be zero if the mixture has already reached ignition. Since the model provides local temperatures and species information, the local (and instantaneous) ignition delay was found by "freezing" the mixture and reaction state within the specified computational cell volume at a given time, and then allowing the mixture to react to completion, as if no further mixing occurs. This procedure was performed for each location in space and instance in time. With this definition of ignition delay, local Damköhler numbers that approach infinity indicate a region of ignition. While this calculation is expensive, the cost is much lower with the reduced-order model than it would be for higher dimensional simulations, while still providing useful information about the competition between time scales that are thought to control combustion recession.

For this analysis, a condition is selected that exhibits no evidence of combustion recession: $T_a = 800$ K, $O_2 = 21\%$, $P_{inj} = 1000$ bar, $\rho_a = 22.8\,\mathrm{kg\,m^{-3}}$, $d_0 = 90\,\mathrm{\mu m}$, fast RD profile. In Figure 66, Da initially increases with time after the start of ramp-down between the nozzle exit and FLOL but then quickly decreases in a small region just upstream of the FLOL. Decreasing Da implies that ignition becomes increasingly difficult with time. From Figure 66, the location that is least likely to experience ignition, as evidenced by the local minimum at the last time instance shown, appears 19 mm downstream from the nozzle, labeled as δ. This position in space may be
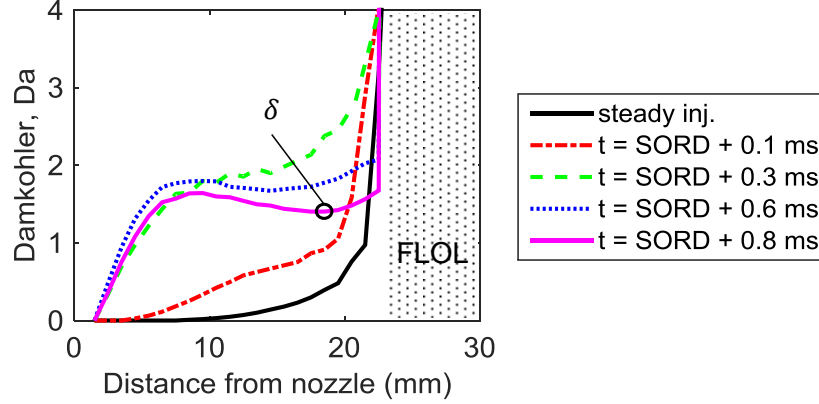
Figure 66: Time evolution of local Damköhler number, Da. Condition: no combustion recession example - $T_a = 800$ K, $O_2 = 21\%$, $P_{inj} = 1000$ bar, $\rho_a = 22.8\,\mathrm{kg\,m^{-3}}$, $d_0 = 90\,\mathrm{\mu m}$, fast RD profile. Hatched region is downstream of the FLOL and out of the area of interest for combustion recession.

viewed as a limiting location of ignition for this condition. In experiments, combustion recession may be inhibited by the competition between mixing and ignition timescales at this location.

Da can then be broken down into its constituents to better understand the competition between timescales that make up Da and the source of the limiting location for ignition. After the start of ramp-down, the local ignition delay in Figure 67a generally decreases until approximately 0.3 ms after the start of ramp-down. This is due to these mixtures becoming more fuel lean, approaching the most reactive equivalence ratio (approximately unity for this condition). After this point in time, the ignition delay rapidly increases at exactly the limiting location for ignition, δ. The local residence time in Figure 67b, however, increases in a nearly uniform fashion indicating that the limiting location for ignition, δ, is not dominated by changes in residence time after end-of-injection.

Upon inspection of the mixing field in Figure 68, three important observations are made that will form the foundation for the scaling approach in this thesis. First, an inflection point, γ, occurs approximately 16 mm downstream of the nozzle and 0.1 ms after the start of ramp-down (SORD). Second, the timing at which the inflection point
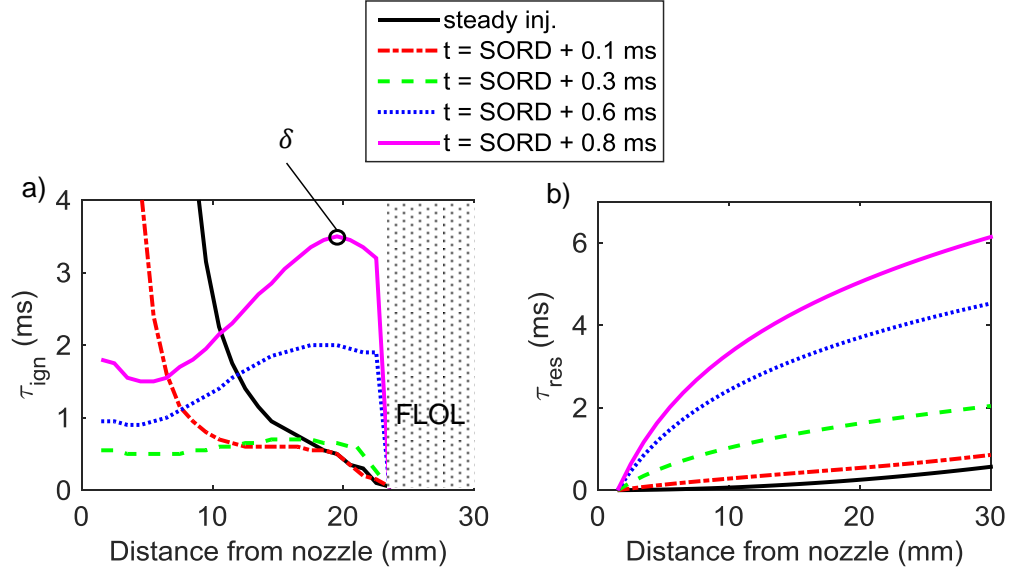
Figure 67: Time evolution of a) local ignition delay; b) local residence time. Condition: no combustion recession example - $T_a = 800$ K, $O_2 = 21\%$, $P_{inj} = 1000$ bar, $\rho_a = 22.8 \, \text{kg m}^{-3}$, $d_0 = 90 \, \mu\text{m}$, fast RD profile. Hatched region is downstream of the FLOL and out of the area of interest for combustion recession.

first arises coincides with the linear ramp-down duration, or characteristic timescale of velocity decrease, $\alpha = 100 \, \mu\text{s}$, suggested by Boree et al. [101]. The characteristic timescale of velocity decrease is defined as,

$$\alpha = U_0/(dU_0/dt), \tag{50}$$

where U_0 represents the injection velocity at the nozzle during steady injection [101]. Evidence that the timing of the inflection point coincides with the linear ramp-down duration, or characteristic timescale of velocity decrease, α, is shown in Figure 69. In the figure, equivalence ratio predictions during steady injection and at the timing for which the inflection point first arises are shown for three different linear ramp-down durations. Notice that the timing of the inflection point corresponds with the linear ramp-down duration. Lastly, in Figures 68 and 69, the limiting location for ignition, δ, occurs slightly downstream of the inflection point, at the head of the entrainment wave, when the inflection point first arises. Since calculation of the limiting location for ignition is computationally intensive, perhaps the relationship between the limiting
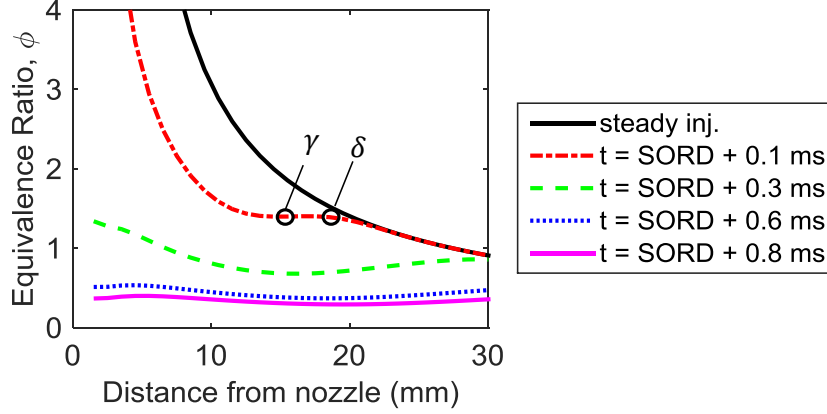
Figure 68: Time evolution of mixing field. Condition: no combustion recession example - $T_a = 800$ K, $O_2 = 21\%$, $P_{inj} = 1000$ bar, $\rho_a = 22.8\,\mathrm{kg\,m^{-3}}$, $d_0 = 90\,\mu\mathrm{m}$, fast RD profile.

location for ignition, δ, and the inflection point, γ, can be exploited. This is fortuitous because calculation of the mixing field, and hence γ, is less computationally intensive. Moreover, an analytical solution, to some extent, exists for the mixing field [40].

Since combustion recession is defined as the consumption of fuel-air mixtures upstream of the FLOL, correlating FLOL to this limiting location of ignition could provide a simple way to scale combustion recession. For instance, if the limiting location for ignition occurs upstream of the FLOL, then combustion recession is less likely. This was observed in Figure 66. Likewise, if the limiting location for ignition occurs downstream of the FLOL, then combustion recession is more likely. The results of this scaling have the potential to be applied to a wider class of injectors and injection strategies than those experimentally tested in this work. This scaling could also enhance understanding of the controlling physics regarding combustion recession.

6.4 Scaling Combustion Recession

The challenge of this scaling equates to finding an analytical expression for δ, the limiting location for ignition, as a function of boundary conditions and/or common jet metrics. To find an analytical expression for the limiting location of ignition, δ,
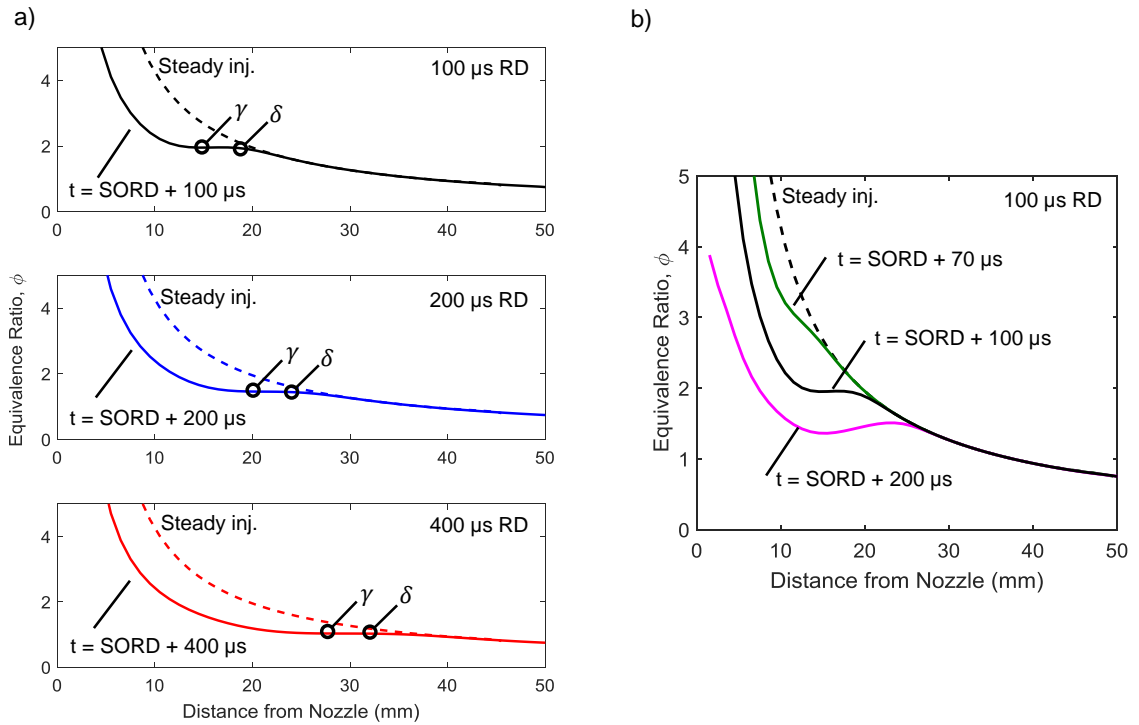
Figure 69: a) Evidence that the timing of the inflection point, γ, coincides with the linear ramp-down duration, or characteristic timescale of velocity decrease, α; b) Additional time instances during ramp-down for the $100\,\mu s$ RD profile. Condition: no combustion recession example - $T_a = 800$ K, 21% O_2, $P_{inj} = 1000$ bar, $\rho_a = 22.8\,\mathrm{kg\,m^{-3}}$, $d_0 = 90\,\mu m$, fast RD profile.

we start by assuming that a diesel spray is analogous to a dense turbulent gas jet, similar to Musculus [40]. He derived a transport equation for the axial momentum flux within the jet as follows,

$$\frac{\partial \dot{M}}{\partial t} = -2 \cot \theta/2 \sqrt{\frac{\beta}{\pi \rho_a}} \frac{\sqrt{\dot{M}}}{x'} \frac{\partial \dot{M}}{\partial x}, \tag{51}$$

where $\dot{M}, \theta, \beta, \rho_a$, and x' represent the axial momentum flux, full spreading angle, transition parameter, ambient density, and axial distance from the nozzle virtual origin, respectively. By using the method of characteristics, Musculus obtains an explicit equation for $\sqrt{\dot{M}}$ that is valid within the transient region, i.e.,

$$x'^2 - 4 \cot \theta/2 \sqrt{\frac{\beta}{\pi \rho_a}} \sqrt{\dot{M}_0} t < (x_0)^2, \tag{52}$$

where time, t, is with respect to the start-of-ramp-down. The transient region represents portions of the jet that depart from steady injection behavior and this region grows according to the propagation of the entrainment wave. This equation can then be used to determine the position of the limiting location for ignition, δ, by substituting δ for x' and α for t. Since δ occurs downstream of the inflection point, γ, at the head of the entrainment wave, the furthest axial extent of the transient region, x', is identically the location of δ. Also, the time after start-of-ramp-down, t, for which the inflection point, γ, appears is identically the characteristic timescale of velocity decrease, α. Assuming that the distance between the virtual origin and the nozzle exit, x_0, is small and that $(x_0)^2$ is even smaller, the position of the limiting location for ignition can be estimated with the following,

$$\delta \approx \sqrt{4 \cot \theta/2 \sqrt{\frac{\beta}{\pi \rho_a}} \sqrt{\dot{M}_0} \alpha}. \tag{53}$$

To account for the jet being a different density than the ambient fluid, the momentum diameter, $d_m = \sqrt{\rho_f/\rho_a} d_{eff}$, is used in the axial momentum flux at the nozzle

exit during steady injection, $\dot{M}_0 = \pi/4\rho_f d_m^2 U_{eff}^2$. Note that the effective injection velocity during steady injection, $U_{eff} = C_v U_0$, and effective nozzle orifice diameter, $d_{eff} = \sqrt{C_a}d_0$, make use of the velocity, C_v, and area contraction, C_a, coefficients respectively. Then, substitution into Eq. 53 reveals the following,

$$\delta \approx \sqrt{2\cot\theta/2\sqrt{\frac{\beta\rho_f}{\rho_a}}d_{eff}U_{eff}\alpha}. \tag{54}$$

Effectively, Eq. 54 estimates the limiting location for ignition, δ, as a function of common jet metrics and/or boundary conditions, and its relative position to the FLOL is used to develop a correlation for the likelihood of combustion recession. That is, the likelihood of combustion recession is directly proportional to the relative scaling of the FLOL and the limiting location for ignition at a given operating condition.

To provide a more intuitive meaning, the characteristic length scales, δ and FLOL, can be converted to characteristic time scales by dividing each by the effective injection velocity. The quantity $FLOL/U_{eff}$ is a joint mixing-chemistry timescale required for ignition during the steady portion of injection. The quantity,

$$\delta/U_{eff} \approx \sqrt{2\cot\theta/2\sqrt{\frac{\beta\rho_f}{\rho_a}}d_{eff}\alpha/U_{eff}} \tag{55}$$

is a joint mixing-chemistry timescale for ignition after the end-of-injection. Thus, the proportionality between the two timescales is used to predict the likelihood of combustion recession, shown in the next section.

Note that while calculation of α is straightforward for the fast ramp-down profile (α_{fastRD}=100 μs) shown in Figure 41a, the same is not true for the slow ramp-down profile because of the two distinct slopes. Thus, an equivalent α is found using the procedure outlined below.

From the normalized injection velocities in Figure 41b, the slow RD profile decreases injection velocity to approximately 65% of its steady value during the first
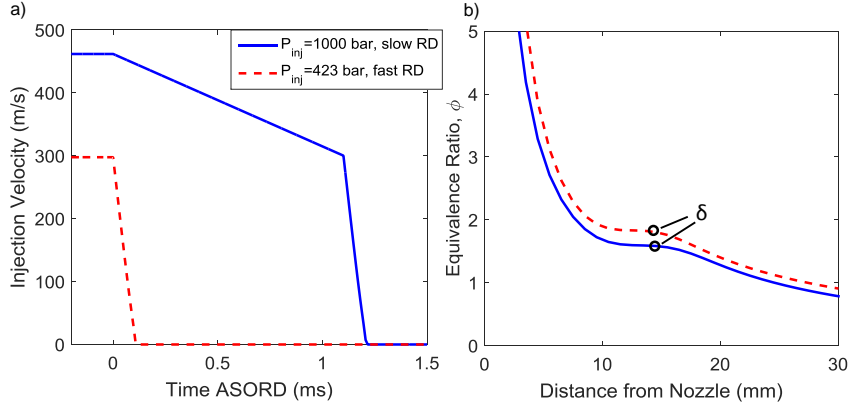
Figure 70: Methodology for finding an equivalent α for the slow RD injection profiles. a) Injection velocity at 60 bar ambient pressure b) equivalence ratio distribution at the time instance of when the inflection point appears.

phase of ramp-down, which lasts approximately $1100\,\mu s$. The second phase of ramp-down is very rapid, decreasing the injection velocity to zero in approximately $100\,\mu s$. Using this knowledge, the 1000 bar, slow RD profile is modeled in Figure 70a with only the most salient features of the measured injection velocity. δ can then be located in Figure 70b. In terms of the position of δ (14 mm downstream of the nozzle), the 1000 bar, slow RD profile is identical to a lower injection pressure of 423 bar but with a fast ramp-down profile. This is because an injection pressure of 423 bar produces an injection velocity that is 65% of 1000 bar. Clearly, the second phase of ramp-down dominates the position of δ.

From this result, U_{eff} could be replaced by 65% of its steady value for any of the slow RD profiles, along with α=$100\,\mu s$, in Eq. 55 to yield an equivalent timescale δ/U_{eff}. However, the only parameter that is designed to encapsulate the end-of-injection transient is α; all other parameters involve steady injection quantities or ambient conditions. Therefore, for the slow RD profile, $\alpha_{slowRD} = \alpha_{fastRD}/0.65$ while U_{eff} will remain its steady value prior to ramp-down. This procedure is recommended for ramp-down profiles that are not single slope, linear ramp-down profiles.
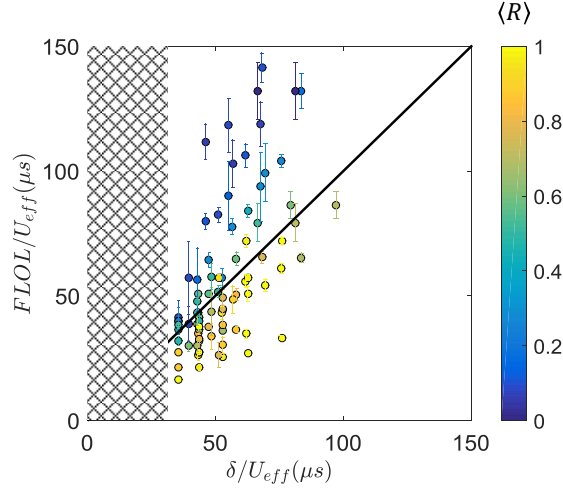
Figure 71: Experimental validation of combustion recession scaling using data from test matrix in Table 2. The hatched region indicates conditions outside of interest for practical diesel engine applications.

6.4.1 Experimental Validation

From Figure 71, the experimental data appear to follow the proposed linear scaling reasonably well. That is, experimental observations of complete combustion recession (high $\langle R \rangle$) largely lie below the linear proportionality boundary, while conditions with partial or no/weak combustion recession (low $\langle R \rangle$) largely lie above the boundary. Note that the horizontal (δ/U_{eff}) error bar length for each data point is smaller than the width of the symbol and has been omitted for clarity.

To aid in the interpretation of the scaling results and to include measurements of soot recession, the data will be classified into 4 distinct regimes: i) complete combustion recession, ii) partial combustion recession, iii) no/weak combustion recession, and iv) soot recession. Because R varies from shot to shot, the range for each regime was decided upon using the following logic. On average, the difference between the minimum and maximum instantaneous values of R for each $\langle R \rangle$ is approximately 0.3, shown in Figure 72, suggesting that each regime comprise a third of the spectrum. Defining each regime in this way provides at least a semi-quantitative description of the combustion recession nature. Thus, the ensemble average of the combustion

135
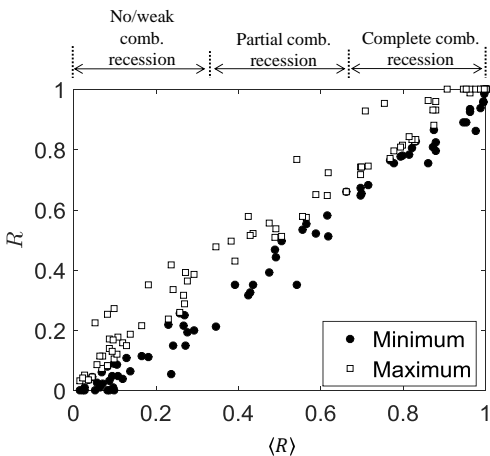
Figure 72: Individual combustion recession metric, R, versus its ensemble average, $\langle R \rangle$, using data from test matrix in Table 2.

recession metric, $\langle R \rangle$, was chosen to be evenly divided into three regimes: i) complete combustion recession for $0.66 < \langle R \rangle \leq 1$, ii) partial combustion recession for $0.33 \leq \langle R \rangle \leq 0.66$, and iii) no/weak combustion recession for $0 \leq \langle R \rangle < 0.33$ (see Figure 72). Note that all of the data for the conditions shown in Table 2 were used to construct Figure 72, so that this regime classification is comprehensive.

Interestingly, from the knowledge that the range for each $\langle R \rangle$ is approximately 0.3, one can conclude that the repeatability of each test condition is high. In other words, fluctuations in the boundary conditions of the experiment are low. Presumably, if the data were more sensitive to shot-to-shot deviation, complete combustion recession might happen in one shot and no combustion recession might happen in another. This is not the case, however, based on the relatively low range of R for each $\langle R \rangle$.

Although uncertainty in the measured flame lift-off length and/or boundary conditions causes a slight overlap between observed combustion recession regimes in Figure 73a, interpretation of the data is much easier compared to Figure 71. The diagram presented in Figure 73b is intended to complement Figure 73a, providing a simple conceptual map for each regime. Essentially, for long end-of-injection ignition time scales relative to steady injection ignition timescales, soot recession will occur.
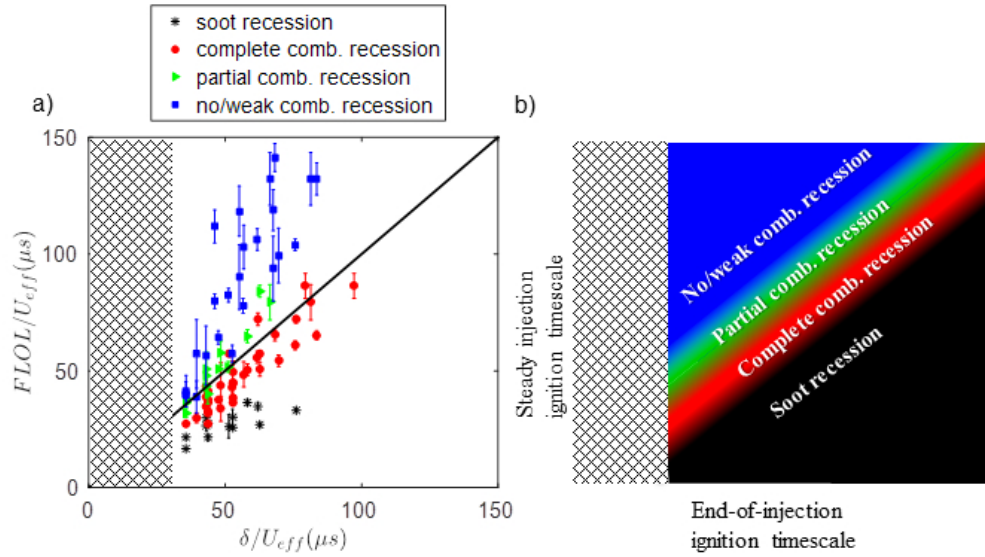
Figure 73: a) Combustion recession regime diagram with experimental data; b) conceptual diagram - hatched region indicates conditions outside of interest for practical diesel engine applications.

Soot recession spatially and temporally overlaps with combustion recession and is the result of igniting rich mixtures. As end-of-injection ignition time scales become relatively shorter, igniting mixtures are leaner such that soot is not formed and thus complete combustion recession is observed. Continuing on to relatively shorter end-of-injection ignition timescales, combustion recession becomes less pronounced with only pockets of ignition observed upstream of the flame lift-off length, referred to as partial combustion recession. Finally, if end-of-injection ignition timescales are sufficiently short, combustion recession will not occur and result in increased UHC emissions (shown later in Figure 75).

6.4.2 Reduced-Order Model Predictions

To further explore this combustion recession scaling at conditions beyond the experimental test matrix, the reduced-order model presented in this thesis was utilized. Reduced-order modeling enables a wide range of conditions to be explored,

which would have been otherwise cost-prohibitive with a more complex modeling approach. Moreover, as will be shown and discussed, by retaining only select physics, the reduced-order model will enable a better understanding of the key processes driving combustion recession. For these simulations, chemical mechanisms from Cai et al. [83] and Yao et al. [105] were used. Also, since the model explores conditions outside of the experimental test matrix and requires FLOL as an input, the correlation from Benajes et al. is used [81]:

$$FLOL = 1.45e10T_a^{-3.89}\rho_a^1 d_0^{0.34} U_0^{0.54} Z_{st}^{-1}. \tag{56}$$

A comprehensive set of simulated conditions that supports the proposed combustion recession scaling is demonstrated in Figure 74. Points were selected to provide an even distribution of data within the range of interest for practical diesel engine applications without an excessive number of simulations. Each point was assigned a desired $FLOL/U_{eff}$ and δ/U_{eff}, but many combinations of ambient temperature, ambient density, ramp-down duration, etc., are possible to achieve the desired point. Thus, each desired point is essentially a constrained nonlinear multivariable problem. The constraints on conditions are as follows - ambient temperature: 850-1000 K, ambient density: 7.8-22.8 $\mathrm{kg\,m^{-3}}$, ambient oxygen concentration: 10-21%, injection pressure: 500-1500 bar, nozzle orifice diameter: 90-180 µm, and single-slope, linear ramp-down profile α: 100-1000 µs. The interior-point algorithm was selected to minimize each constrained nonlinear multivariable function with a random initial point within the bounds of the constraints. A total of 75 simulations were performed, with finer resolution along the proposed boundary between complete and partial combustion recession. Lastly, calculation of the combustion metric, R, for the model results was performed in the same way as described previously for the experiments, but using predictions of second-stage ignition. Second-stage ignition was identified as the instance in time and the location in space where the predicted local temperature rose

138
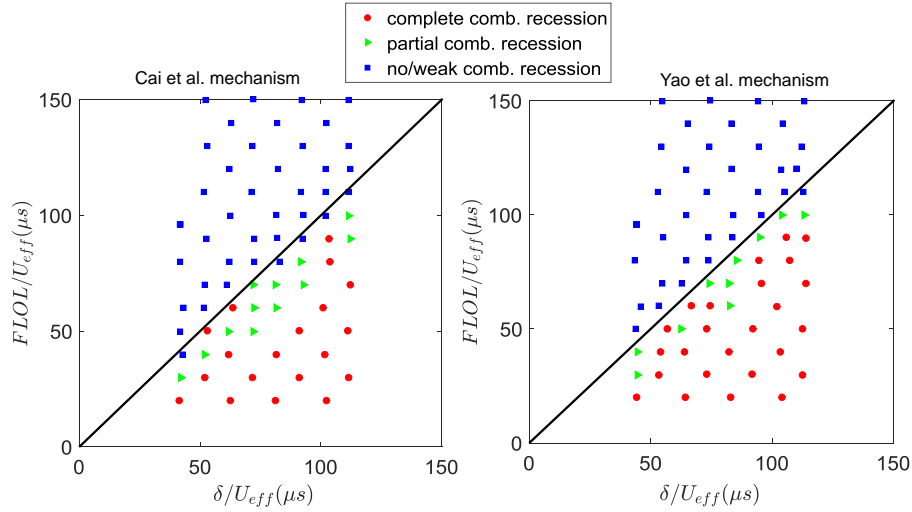
Figure 74: Model predictions of combustion recession using the chemical mechanisms of Cai et al. [83] and Yao et al. [105].

above 1500 K.

Regardless of the chemical mechanism used, the model captures the trends with respect to the proposed scaling. Along the boundaries, however, the outcome of combustion recession appears to be sensitive to the mechanism employed. While some sensitivity is apparent, the predicted outcome varies only between adjacent regimes, e.g. the Cai et al. mechanism predicts partial combustion recession while the Yao et al. mechanism predicts complete combustion recession at $FLOL/U_{eff}$ =90 µs and δ/U_{eff}=110 µs. For these simulations, no condition was found where complete combustion recession was predicted with one mechanism and no combustion recession with the other.

6.4.2.1 Unburned Hydrocarbons and Carbon Monoxide

Because UHCs are challenging to measure, predictions of UHC emissions normalized by the total injected mass, m_{inj}, are shown in Figure 75a. UHC emissions include all hydrocarbons in the chemical mechanism including partially oxidized species, i.e. aldehydes. From the figure, excessive UHC emissions are correlated with the absence of combustion recession, where UHC predictions near 10-15% of the total injected

139
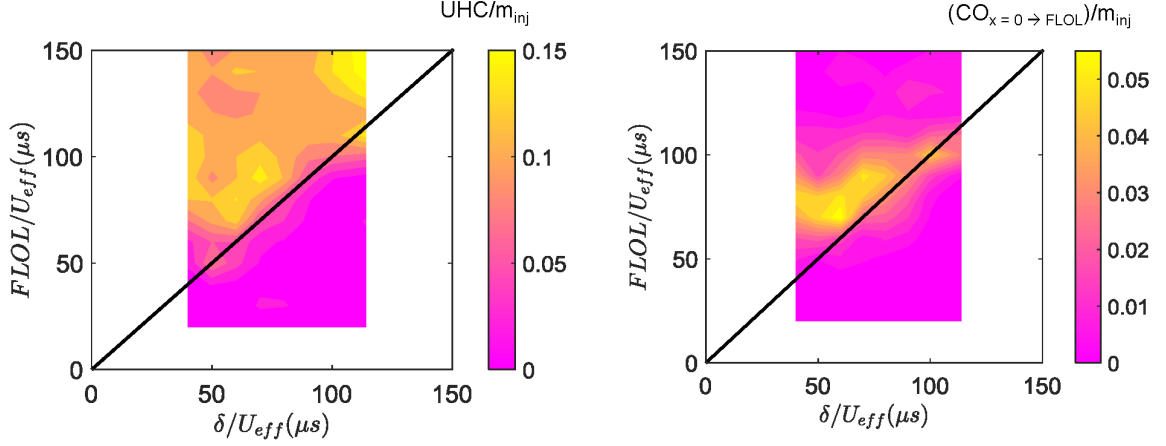
Figure 75: Model predictions of the normalized unburned hydrocarbon (UHC) and carbon monoxide (CO) emissions using the Cai et al. [21] chemical mechanism.

mass are shown in these regions. Previous work from Musculus and coworkers has shown a strong correlation between excessive unburned hydrocarbons and positive ignition dwell [10], but this study suggests that ignition dwell alone is not a robust parameter for correlation. This is because all of the conditions in this study are negative ignition dwell and yet similar excessive unburned hydrocarbons are predicted. Based on this work, the likelihood of combustion recession is a more robust parameter for correlation to unburned hydrocarbons. Indeed, for the positive ignition dwell conditions studied by Musculus and coworkers, combustion recession was never observed. While many LTC strategies often feature a positive ignition dwell, new low-emissions concepts are emerging that exhibit a negative ignition dwell, e.g. Leaner Lifted Flame Combustion (LLFC) [106], which may also suffer from excessive UHC.

Measurements of CO are also challenging; hence, model predictions of normalized CO are shown in Figure 75b. This figure demonstrates that near-nozzle CO, between the nozzle exit (x=0) and the flame lift-off length (x=FLOL), is primarily produced in a region that correlates with the boundary between partial and no/weak combustion recession. In this region of the diagram, near-nozzle mixtures only partially ignite leaving high levels of both CO and UHC. Towards the no/weak combustion recession

140
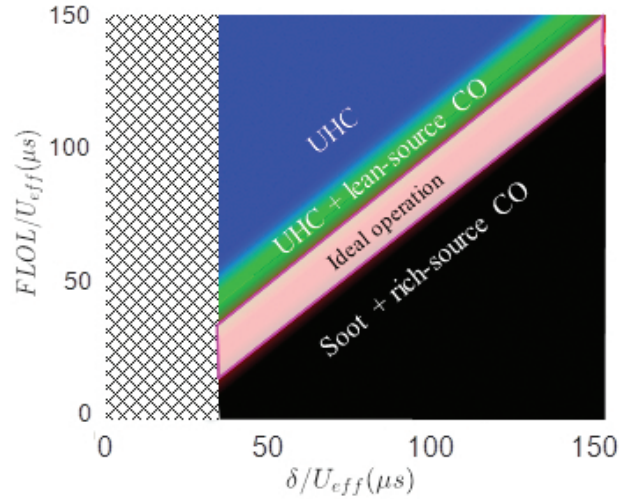
Figure 76: Conceptual diagram of excessive emissions regions and an ideal region of operation.

regime near-nozzle mixtures do not ignite at all, leaving only high levels of UHC.

A conceptual diagram is presented in Figure 76 that highlights regions of excessive emissions and a region of ideal operation. This region of ideal operation presumes that the user has control over the end-of-injection transient given a particular operating condition. The diagram, as a whole, may also apply to shorter injection durations where the ignition dwell becomes positive. While a steady FLOL does not exist for such transient conditions, FLOL may be replaced with a correlation in terms of the boundary conditions, such as Eq. 56. Shorter injection durations likely do not influence the outcome of combustion recession but they will change the fraction of UHC/m_{inj} because m_{inj} will be smaller for shorter injections. Evidence supporting the claim that injection duration does not influence the outcome of combustion recession is shown in Figure 78 and is discussed later.

6.4.3 Discussion

A subtlety of this scaling and of the physical understanding of the scaling parameters involved is that autoignition processes are assumed to dominate flame lift-off stabilization and combustion recession. This assumption for flame lift-off stabilization is supported by Pickett et al., who found evidence of detached second-stage ignition kernels and a cool flame upstream of the FLOL [34]. By stating that the scaling parameter, $FLOL/U_{eff}$, is the timescale for ignition in steady sprays assumes that the initial ignition location and FLOL are identical. Indeed, the initial ignition location tracks well with FLOL for many fuels, where it is often very close to the FLOL, or it is slightly downstream [107]. The assumption that ignition processes drive combustion recession is supported by the existence of the partial combustion recession regime, where rather than a connected flame sheet propagating back towards the nozzle after end-of-injection, distinct pockets of ignition were observed to appear. This assumption is also supported by the fact that the model only considers ignition processes and yet the model results largely match those of the experiments.

Also implicit to the model is the assumption that the spray is mixing-controlled, and not atomization-controlled, even after end-of-injection. To date, there is no direct supporting evidence for this assumption to hold after end-of-injection. Presumably, spray breakup processes become slower as the injection velocity declines, which might support the formation of large-scale droplets that could control fuel-air ratios in the near-nozzle region and hence combustion recession. However, this thesis found that there is significant temporal separation between complete vaporization of liquid and the appearance of combustion recession, suggesting that there is no interaction between the two. Hence, the vaporization mixing-controlled assumption, which enables the parallel to dense turbulent gas-jets, also appears to be reasonable after end-of-injection. However, soot-producing dribble is evidence that large individual droplets

are present and that at least some portion of the end-of-injection transient is atomization controlled.

6.4.4 Applicability of Scaling

Because the proposed scaling relates ignition timescales during steady injection to ignition timescales after end-of-injection, it is expected that this scaling (and regime diagram) is largely fuel independent. The same chemical processes, i.e. ignition, that govern the steady-state flame lift-off length are likely the same that govern combustion recession. This is fortuitous because correlations for steady-state flame lift-off length as a function of different fuels are more readily available in the literature. Moreover, steady-state flame lift-off length is a simpler metric to measure than combustion recession.

To test the dependency of the proposed scaling on fuel properties, combustion recession data from Primary Reference Fuel (PRF) blends of n-heptane and 0-80% isooctane are shown in Figure 77. This data has been developed through a collaboration with CMT - Motores Térmicos. They performed high-speed imaging of schlieren and broadband chemiluminescence but not OH* chemiluminescence, which was used to more reliably measure combustion recession in this thesis. Hence, only qualitative indications of combustion recession from this fuel-blend dataset are available. The conditions explored are the following: T_a = 800-1000 K, O_2 = 15-21%, P_{inj} = 500-1500 bar, d_0 = 90 µm, ρ_a = 22.8 kg m^{-3}. While the dataset is not comprehensive and only qualitative indications of combustion recession are available, Figure 77 shows no evidence that suggests failure of the proposed scaling.

The fuel independence of the regime diagram may not be true for certain fuels, however. For example, Lequien et al. found that with a particular synthetic fuel that has a very low cetane number of 17, the FLOL stabilized at a position far upstream, approximately 15 mm, from its initial ignition location suggesting that
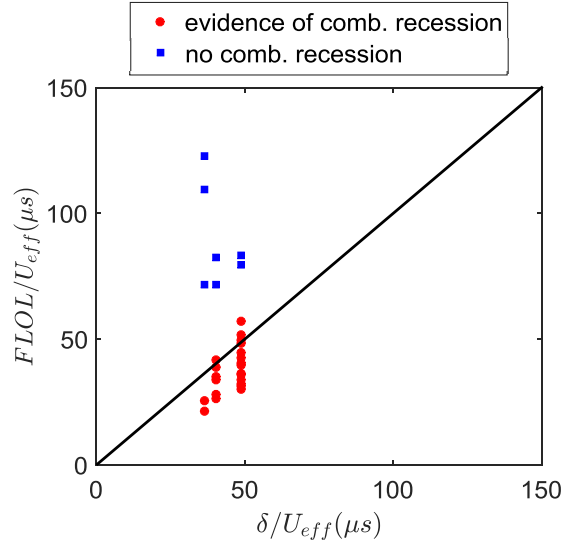
Figure 77: Data courtesy of CMT - Motores Térmicos. PRF blends of n-heptane and 0-80% isooctane, T_a = 800-1000 K, O_2 = 15-21%, P_{inj} = 500-1500 bar, d_0 = 90 µm, ρ_a = 22.8 kg m^{-3}.

flame propagation processes may play an important role under some conditions [108].

Another consideration is the impact of injection duration on the proposed scaling and regime diagram. With regard to combustion recession, the main differences between short and long injections are likely the relative effects of head vortex dynamics and other transient effects from the start-of-injection or ramp-up duration. For short injections head vortex dynamics and other transient effects from the start-of-injection will encompass a larger fraction of the total jet volume compared to longer injections. The transient effects from the start of injection are likely concentrated in the head region, however, and the head is relatively far downstream by the time of autoignition. This means that the only way the head can influence near-nozzle mixtures is through propagation of information upstream (temperature, pressure, radicals, etc.). Since ignition processes appear to dominate combustion recession behavior, there is little to no propagation of information upstream, meaning that the expected impact of injection duration on the proposed scaling and regime diagram is minimal. There will also be no steady flame lift-off length but this can be remedied by replacing

FLOL with a correlation in terms of the boundary conditions, like that in Eq. 56. Experimental evidence supporting these ideas is given in Figure 78 where a long and short injection are shown for a given condition: $T_a = 950$ K, $O_2 = 21\%$, $P_{inj} = 1500$ bar, $\rho_a = 22.8\,\mathrm{kg\,m^{-3}}$, $d_0 = 90\,\mathrm{\mu m}$, fast RD profile. Notice that both injections experience complete combustion recession by 0.27 ms after end-of-injection, regardless of the injection duration.

One final consideration is the effect of injection timing on the proposed scaling and regime diagram. As injection timing is advanced or retarded, compression heating or cooling will occur that can have an impact on the ignition kinetics that drive combustion recession. The effect of injection timing on combustion recession is likely dependent on which scenario to consider: early or late injection. If the injection timing is early enough such that combustion recession is developing as the cylinder gases compress, combustion recession should be accelerated or promoted. However, combustion recession may be inhibited if the injection timing is sufficiently late such that in-cylinder gases are expanding as combustion recession is developing. It is important to keep these two scenarios in mind for practical application of the proposed scaling and regime diagram.
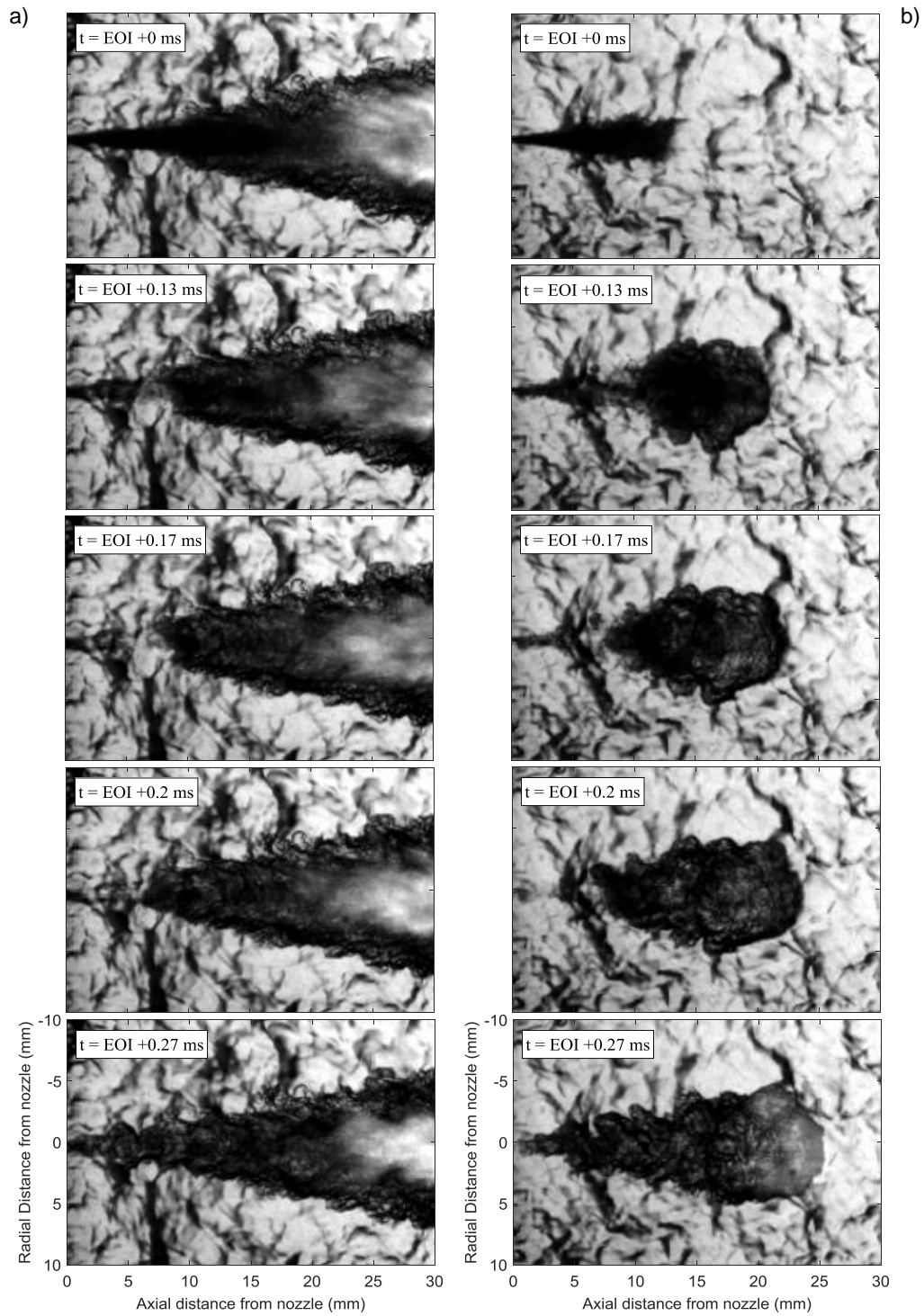
Figure 78: Impact of injection duration on combustion recession outcome with a) long injection duration, $t_{inj} = 3.5$ ms and b) short injection duration, $t_{inj} = 0.2$ ms. The conditions are as follows: $T_a = 950$ K, $O_2 = 21\%$, $P_{inj} = 1500$ bar, $\rho_a = 22.8 \, \text{kg} \, \text{m}^{-3}$, $d_0 = 90 \, \mu\text{m}$, fast RD profile.

CHAPTER VII

CONCLUSIONS AND RECOMMENDATIONS FOR FUTURE WORK

7.1 *Conclusions and Contributions*

This chapter aims to summarize the main conclusions and important contributions of this thesis. Recommendations for future work will also be provided.

7.1.1 Experimental Facilities

In Chapter 2, the experimental facilities were detailed. Characterization of the temperature distribution within the optical spray chamber was performed for a wide range of chamber pressures and temperatures. These measurements provided valuable boundary conditions for use as model inputs and enabled meaningful comparisons of important spray and combustion observables between experiments and model predictions.

First introduced in Chapter 2 but fully explored in Chapter 4 was the development of a measurement technique to quantify the transient injection rate. This technique is less susceptible to measurement artifacts than the commonly used long-tube method. Both precision and systematic uncertainties were identified, quantified, and minimized accordingly. Recommendations from this work include the use of an Integrated-Electronics-Piezo-Electric (IEPE) sensor with low acceleration sensitivity and high resonant frequency to minimize the unwanted effects of noise and measurement artifacts. Within the scope of quantifying injection transients, this work also recommends that measurements be conducted at atmospheric back-pressure rather

than elevated back-pressures. At elevated back-pressures, the end-of-injection transient appears artificially longer compared to lower back-pressures. This is caused by improperly relating the reaction force, as measured by the sensor, to the rate-of-momentum at the nozzle exit. Control volume analysis is required to properly relate these two quantities but there are many difficult to quantify terms at elevated back-pressures. However, these terms are negligible at atmospheric back-pressure such that simply equating the measured reaction force to the rate-of-momentum is much more reasonable.

Lastly, a significant contribution of this thesis is the development of a fully-flexible injection rate-shaping system, outlined in Chapter 2 and fully characterized in Chapter 4. This system is capable of creating different injection rate shapes more quickly and easily than commercial Hydraulic-Electronic-Unit-Injector (HEUI) systems and may be used as a platform for future investigations on the effect of fuel injection rate-shaping in diesel engines. Results using this system are then used to objectively evaluate the potential of end-of-injection rate-shaping to minimize unburned hydrocarbon (UHC) and carbon monoxide (CO) emissions for low-temperature combustion (LTC) strategies. Two end-of-injection rate shapes were used in this thesis: a rapid end-of-injection transient that is single-slope and linear and lasts $\sim 100\,\mu s$ - termed *fast RD*, and a less rapid, two-slope end-of-injection transient that lasts $\sim 1100\,\mu s$ - termed *slow RD*.

7.1.2 Combustion Recession Database

In Chapter 5, three high-speed, line-of-sight optical diagnostics were simultaneously evaluated to study end-of-injection effects on combustion and soot recession. OH* chemiluminescence imaging proved to be more reliable for measurement of combustion recession than broadband imaging because broadband suffers from interference due to background reflections that are caused by intense soot luminosity. However,

broadband imaging was useful for qualitative indications of soot that allowed identification of soot recession and burning dribble. Schlieren imaging was useful to visualize the transition from liquid spray to vapor/first-stage ignition and then to second-stage ignition. These simultaneous diagnostics worked in tandem to discern ignition from product mixing and from soot during combustion.

This thesis is the first work to systematically identify the exact conditions for which combustion and soot recession are expected. From the measurements in Chapter 5, four distinct behaviors of the spray flame following end-of-injection were identified: *soot recession*, *complete combustion recession*, *partial combustion recession*, and *no/weak combustion recession*. Also from these measurements, a database was developed that can aid the design of multiple injection strategies. Subsequent injections could encounter one of three scenarios: they could penetrate into i) combustion products, ii) partially reacted species or iii) very lean unreacted fuel-air mixtures, and the particular scenario is dependent on the timing and existence of combustion recession.

In Chapter 6, regression of the measurements from a two-level, six factor full-factorial design of experiments revealed that the most influential parameters regarding combustion recession are the ambient thermodynamic conditions followed by the injection rate shape and injection parameters. Combustion recession was found to be promoted with higher ambient temperatures, higher ambient oxygen concentrations, higher ambient densities, longer end-of-injection transients, lower injection pressures, and larger nozzle orifice diameters. Similar trends were observed for soot recession.

7.1.3 Reduced-Order Model

The development of a new reduced-order model was first presented in Chapter 2 and validated against existing experimental data in Chapter 3. This model aimed to capture only the key physics that drive combustion recession and hence highlight the significance of certain processes. The model was able to predict ignition delay as

a function of ambient temperature and oxygen concentration with similar accuracy to higher fidelity models in the literature. In Chapter 6, model predictions of the transition between combustion recession behavior as each factor in the design of experiments was varied revealed good agreement with experiments.

Key insights for capturing combustion recession computationally are mainly derived from the good agreement between the reduced-order model predictions and experiments in Chapter 6 but some insights stem from the experiments themselves. The model only considers ignition and yet the model results largely match those of the experiments, suggesting that ignition processes dominate combustion recession. The existence of the *partial combustion recession* regime is further evidence supporting the idea that ignition processes dominate combustion recession, where rather than a connected flame sheet propagating back towards the nozzle after end-of-injection, distinct pockets of ignition were observed to appear. From the knowledge that ignition processes are so important to capturing combustion recession, the accuracy of the chemical mechanism is paramount. Perhaps accuracy of the chemical mechanism is more important than the effects of turbulence-chemistry (TCI) interaction, since the model neglects TCI and yet the predictions are in reasonable agreement with experiments. Details of the spray break-up process also appear to be negligible since the gas-jet approximation proved to be reasonably successful for predictions of combustion recession. Lastly, from the experiments, large-scale vortical structures are visible during combustion recession suggesting that a Large Eddy Simulation (LES) may better predict local pockets of ignition than a Reynolds-Averaged Navier-Stokes (RANS) approach.

Chapter 6 revealed that overall the majority of fuel parcels injected during either the fast RD profile or during the second phase of ramp-down for the slow RD profile remain upstream of the flame lift off length (FLOL) and could participate directly in combustion recession. These fuel parcels experience more rapid leaning compared to

150

steady injection. Longer end-of-injection transients limit the rapid leaning effect by limiting entrainment and thus fuel parcels are less likely to experience over mixing and excessive UHC/CO emissions formation.

7.1.4 Scaling

Rather than rely solely on regression for predictions of combustion recession, a first-principles based approach was used to develop a scaling law for combustion recession that is applicable to a wider class of injectors and injection strategies than those tested experimentally. The coupling between end-of-injection mixing and near-nozzle ignition/soot formation timescales, thought to control combustion/soot recession, was analyzed in Chapter 6 with a definition for the local Damköhler, which is defined to be the ratio of local residence time to local (and instantaneous) ignition delay. From this analysis, a limiting location of ignition was identified and linked to the FLOL to develop both an end-of-injection mixing timescale and a steady injection ignition timescale. The proportionality between the two timescales was used to predict the likelihood of combustion and soot recession. For long end-of-injection ignition time scales relative to steady injection ignition timescales, *soot recession* will occur. *Soot recession* spatially and temporally overlaps with combustion recession and is the result of igniting rich mixtures. As end-of-injection ignition time scales become relatively shorter, igniting mixtures are leaner such that soot is not formed and thus *complete combustion recession* is observed. Continuing on to relatively shorter end-of-injection ignition timescales, combustion recession becomes less pronounced with only pockets of ignition observed upstream of the FLOL, referred to as *partial combustion recession*. Finally, if end-of-injection ignition timescales are sufficiently short, combustion recession will not occur.

Based on this work, the likelihood of combustion recession is a more robust parameter for correlation to UHC and CO emissions than ignition dwell. The literature

shows excessive UHC for positive ignition dwell but the results in this thesis are all negative ignition dwell and yet similarly excessive unburned hydrocarbons are predicted.

Also shown in Chapter 6 are evidence that supports the applicability of the proposed scaling to situations beyond those fully explored in this thesis. Qualitative measurements of combustion recession using Primary Reference Fuel (PRF) blends of n-heptane and 0-80% isooctane over a wide range of conditions (data courtesy of CMT - Motores Térmicos) reveal that the proposed scaling approach may also work for many other fuels. This is likely due to the fact that the chemical processes which govern flame lift-off are the same that govern combustion recession. Other brief measurements show little to no dependence of combustion recession on injection duration, suggesting that this scaling approach may also apply to shorter injections and even positive ignition dwell conditions. While a steady FLOL does not exist for such transient conditions, FLOL could simply be replaced with a correlation in terms of the boundary conditions.

7.1.5   On the Use of Injection Rate-Shaping

Ideally, future fuel systems may offer opportunities to directly control the end-of-injection transient and the combustion/soot recession processes discussed. Given a particular operating condition, the end-of-injection transient should be sufficiently rapid to prevent soot formation in the near-nozzle region and yet slow enough to allow second-stage ignition for consumption of UHC/CO. If an engine operates over a range of conditions, the end-of-injection transient may need to be continuously variable to remain in this perhaps small window of ideal operation. This places a large demand on the injection system to be capable of varying the end-of-injection transient for simultaneous control of combustion and soot recession. However, quantitative measurements of near-nozzle soot using point-based laser soot extinction revealed

that perhaps only a small amount of soot was formed during soot recession and that this soot quickly oxidizes, suggesting that soot recession may not be that important.

The trade-off between near-nozzle UHC/CO and total soot, not just near-nozzle soot, likely depends on the *shape* of the end-of-injection transient. This thesis investigated a two-slope shape where the first slope was pressure-controlled and shallow while the second slope was needle-controlled and quite rapid. This two-slope shape promoted combustion recession (consumption of near-nozzle UHC/CO) but quantitative measurements of soot formed far downstream of the FLOL showed a dramatic increase in soot during the slow, pressure-controlled portion of ramp down. Essentially, the slow, first phase of ramp-down can negatively impact soot formation far downstream and the rapid, second phase has the tendency to negatively impact combustion recession. The ideal shape is likely an appropriately-sized single-slope, linear ramp-down or a rapid first phase to inhibit downstream soot formation followed by a shallow second phase to promote combustion recession.

7.2   Recommendations for Future Work

From a practical perspective, pressure modulation of the injection rate shape appears cumbersome and perhaps not versatile enough to support the demands of future diesel engines. Pressure modulation is not the only method to control the injection rate shape though. More advanced, direct-actuated injectors have the capability to control the needle position, which may be used to tailor the flow rate in a desired way. These piezo-based injectors have near-complete flexibility to control the injection rate shape, which may offer a more robust platform to optimize the end-of-injection transient for simultaneous reductions in UHC/CO and soot.

While the point-based, quantitative measurements of soot and the 2D images of qualitative soot luminosity were helpful in understanding near-nozzle soot, limited information was gained about soot downstream of the FLOL. The quantitative,
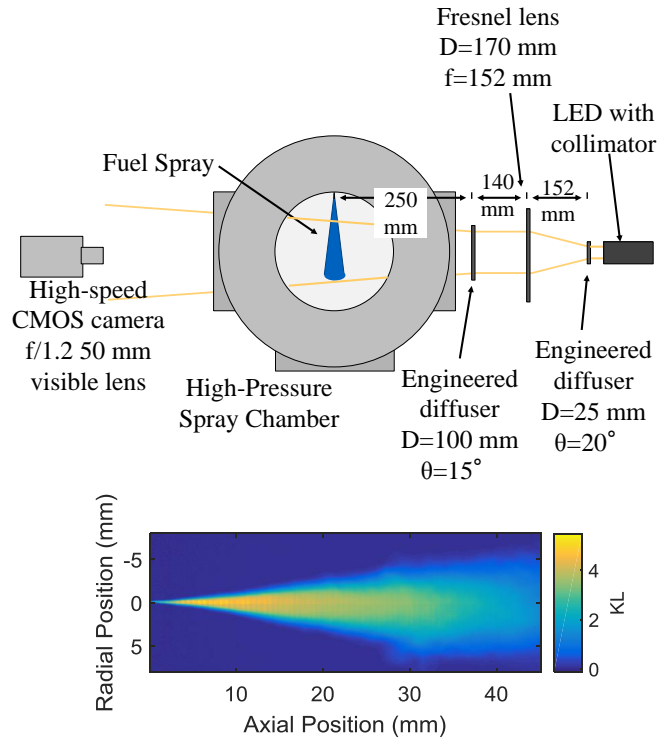
Figure 79: Schematic of measurement setup and a sample of the measured extinction, KL, due to liquid-phase scattering at non-vaporizing conditions.

point-based technique used in this thesis was extremely time-consuming, and thus, a quantitative, 2D soot diagnostic would be immensely helpful for studying the effects of end-of-injection on soot throughout the entire spray flame. Researchers at Sandia National Laboratories have recently developed and outlined a new line-of-sight imaging technique to quantitatively measure 2D maps of time-resolved soot [109]. This technique relies on extinction of light as it passes through the soot cloud and is an improvement on previous attempts that suffered from significant beam-steering. Preliminary measurements using this technique are provided here, albeit for non-vaporizing conditions that focused on extinction due to liquid scattering as opposed to soot absorption. Because this technique has already been constructed and undergone preliminary testing, extension towards conditions that form soot would require minimal effort.

This technique could also be used to image near-nozzle burning dribble and quantify the soot impacts of this phenomenon. While burning dribble was observed in this thesis, the camera resolution and exposure duration were not optimized to make any solid conclusions about the amount of soot produced.

Other recommendations for future work include improvements to the reduced-order model. Perhaps a sub-model to account for dribble is an obvious choice but dribble has yet to be fully characterized. Kastengren et al. have shown that dribble appears more prominent at lower injection pressures [110], but the mass or number and size of dribble has yet to be quantified. Another interesting improvement to the model could be a spatially variable or transient spreading angle. Pickett et al. have shown that the near-field spreading angle is smaller than that of the far-field [80] but the location of this transition and details on differences between the two angles as a function of operating conditions are unknown. Since end-of-injection entrainment is determined in part by the model spreading angle, the impact of a variable spreading angle on combustion recession would be interesting to assess. Jung et al. demonstrated that for multi-hole injectors the spreading angle can be quite transient, suggesting complicated internal nozzle flows [111] for which the impacts on combustion recession would also be interesting to explore. If interest lies in downstream portions of jet, particularly at the head and during reacting conditions, modification of the entrainment rate for reacting conditions and a jet head model may prove useful.

Lastly, other ideas include using combustion and soot recession as a platform for additional model validation studies. These phenomena provide a wealth of information to compare modeling approaches that perhaps more convincingly demonstrates the coupling between turbulent mixing and chemistry than the standard metrics such as ignition delay and flame lift off length.

APPENDIX A

COMBUSTION RECESSION DATABASE

A.1 Combustion Recession Database

The ensemble-averaged combustion recession metric, $\langle R \rangle$, for each condition listed in Table 2 is shown below in Table 6. Uncertainties, σ, at 95% confidence interval are also provided for $\langle R \rangle$ as well as the flame lift-off length, FLOL.

Table 6: Combustion Recession Database

T_a	P_{inj}	O_2	α	d_0	ρ_a	$FLOL$	σ_{FLOL}	$\langle R \rangle$	$\sigma_{\langle R \rangle}$
(K)	(bar)	$(\%)$	(μs)	(μm)	(kg/m^3)	(mm)	(mm)	(dim)	(dim)
902	500	0.15	100	90	22.8	12.4	0.53	0.83	0.11
902	500	0.15	150	90	22.8	12.9	0.67	0.66	0.13
902	1000	0.15	100	90	22.8	16.5	0.92	0.47	0.24
902	1000	0.15	150	90	22.8	16.5	0.53	0.70	0.14
902	1000	0.12	100	90	22.8	18.9	0.54	0.39	0.11
902	1000	0.12	150	90	22.8	18.9	0.25	0.80	0.05
902	500	0.12	100	90	22.8	15.4	1.87	0.71	0.09
902	500	0.12	150	90	22.8	15.8	0.56	0.83	0.01
902	500	0.10	100	90	22.8	18.0	2.69	0.56	0.03
902	500	0.10	150	90	22.8	17.6	1.68	0.77	0.01
902	1000	0.10	100	90	22.8	21.4	3.52	0.10	0.03
902	1000	0.10	150	90	22.8	21.4	1.34	0.62	0.09
902	1000	0.21	100	90	22.8	11.1	0.27	0.87	0.02
902	1000	0.21	150	90	22.8	11.1	0.67	0.96	0.08

156

902	500	0.21	100	90	22.8	9.3	0.80	0.95	0.16
902	500	0.21	150	90	22.8	9.1	0.19	0.96	0.11
798	500	0.21	100	90	22.8	15.5	0.49	0.50	0.05
798	500	0.21	150	90	22.8	15.4	0.95	1.00	0.35
798	1000	0.21	100	90	22.8	20.7	0.94	0.12	0.09
798	500	0.15	100	90	22.8	20.2	4.52	0.16	0.15
798	500	0.15	150	90	22.8	20.5	1.33	0.27	0.15
850	500	0.21	100	90	22.8	10.7	0.78	0.70	0.06
850	500	0.21	150	90	22.8	10.8	1.16	0.88	0.24
850	1000	0.21	150	90	22.8	14.2	0.15	0.71	0.28
850	1000	0.15	150	90	22.8	17.0	0.00	0.82	0.04
850	500	0.15	100	90	22.8	13.8	0.09	0.62	0.31
850	500	0.15	150	90	22.8	13.7	0.22	0.86	0.30
850	500	0.12	100	90	22.8	17.0	0.56	0.49	0.14
850	500	0.12	150	90	22.8	16.0	2.68	0.78	0.06
850	1000	0.12	100	90	22.8	20.8	2.75	0.26	0.01
850	1000	0.12	150	90	22.8	20.8	2.13	0.49	0.06
899	500	0.21	100	90	14.8	13.7	0.14	0.79	0.05
899	500	0.21	150	90	14.8	13.3	0.47	0.88	0.16
899	1000	0.21	100	90	14.8	15.7	1.12	0.60	0.25
899	1000	0.21	150	90	14.8	17.7	2.80	0.87	0.18
899	1000	0.15	100	90	14.8	20.3	3.65	0.07	0.02
899	1000	0.15	150	90	14.8	23.0	5.04	0.70	0.13
899	500	0.15	100	90	14.8	18.5	0.33	0.56	0.07
899	500	0.15	150	90	14.8	18.3	0.91	0.81	0.08
899	500	0.12	100	90	14.8	23.4	1.05	0.27	0.06
899	500	0.12	150	90	14.8	23.6	0.99	0.59	0.19

899	1000	0.12	100	90	14.8	30.0	7.70	0.09	0.16
899	1000	0.12	150	90	14.8	30.3	2.72	0.50	0.02
902	500	0.21	100	90	7.8	33.4	5.12	0.13	0.06
902	500	0.21	150	90	7.8	34.7	5.12	0.29	0.39
902	1000	0.21	100	90	7.8	42.3	1.68	0.10	0.05
902	1000	0.21	150	90	7.8	41.2	1.68	0.29	0.27
902	1000	0.15	100	90	7.8	59.2	3.74	0.06	0.09
902	500	0.15	100	90	7.8	43.8	3.97	0.08	0.00
902	500	0.15	150	90	7.8	44.0	3.25	0.07	0.13
915	1000	0.21	100	90	22.8	8.6	0.13	0.99	0.01
915	1000	0.15	100	90	22.8	14.2	0.39	0.91	0.09
915	1000	0.15	150	90	22.8	14.2	0.35	0.99	0.01
915	1000	0.10	100	90	22.8	19.8	0.55	0.54	0.04
915	1000	0.10	150	90	22.8	19.6	0.38	0.99	0.01
803	1000	0.21	100	186	22.8	26.9	1.20	0.50	0.08
803	1000	0.21	150	186	22.8	26.4	1.59	1.00	0.09
803	500	0.21	100	186	22.8	20.0	0.92	1.00	0.04
803	500	0.21	150	186	22.8	21.8	0.68	1.00	0.03
803	500	0.10	100	186	22.8	38.0	1.66	0.11	0.04
803	500	0.10	150	186	22.8	37.2	0.94	0.27	0.04
803	1000	0.10	100	186	22.8	42.9	1.54	0.09	0.02
803	1000	0.10	150	186	22.8	43.8	1.32	0.43	0.06
900	1000	0.21	100	186	22.8	13.6	2.55	0.76	0.30
900	1000	0.21	150	186	22.8	13.9	0.45	0.99	0.01
900	500	0.21	100	186	22.8	12.4	0.62	1.00	0.08
900	500	0.21	150	186	22.8	11.8	0.29	1.00	0.00
900	500	0.10	100	186	22.8	25.6	0.95	0.98	0.04

900	500	0.10	150	186	22.8	25.6	0.54	1.00	0.00
900	1000	0.10	100	186	22.8	29.8	0.67	0.95	0.03
900	1000	0.10	150	186	22.8	29.8	0.67	0.99	0.02
852	1000	0.21	100	186	14.8	25.5	2.84	0.90	0.29
852	1000	0.21	150	186	14.8	28.5	1.28	1.00	0.00
852	500	0.21	100	186	14.8	23.8	0.94	0.75	0.22
852	500	0.21	150	186	14.8	23.8	0.72	0.68	0.39
852	500	0.10	100	186	14.8	51.5	2.18	0.10	0.06
852	500	0.10	150	186	14.8	48.1	2.50	0.18	0.07
852	1000	0.10	100	186	14.8	54.1	4.92	0.05	0.07
852	1000	0.10	150	186	14.8	52.2	6.15	0.28	0.16
900	500	0.21	100	186	7.8	32.0	2.00	0.61	0.00
900	500	0.21	150	186	7.8	32.0	2.00	0.70	0.00
900	1000	0.21	100	186	7.8	42.0	4.00	0.52	0.00
900	1000	0.21	150	186	7.8	42.0	4.00	0.71	0.00
900	1000	0.10	100	186	7.8	70.0	6.00	0.10	0.00
900	1000	0.10	150	186	7.8	70.0	6.00	0.10	0.00
900	500	0.10	100	186	7.8	65.0	6.00	0.10	0.00
900	500	0.10	150	186	7.8	65.0	6.00	0.46	0.00

APPENDIX B

REDUCED-ORDER MODEL CODE

B.1   Reduced-Order Model Code

```matlab
%% inputs
D0 = 90*1e-6; % [m] nozzle diameter
injpress = 1500*1e5; % [Pa] injection pressure
ambtemp = 900; % [K]
rho_a = 22.8; % [Pa]
o2frac = 15*1/100; % [dim]
lengthoframpdown = 100*1e-6;
rho_f= 699; % [kg/m^3] fuel density
total_length = 0.10; % [m] Domain size
dx = 1e-3; % [m] CV widths
Ca = 1; % [dim] area contraction coefficient
Cd = 0.89; % [dim] discharge coefficient
ambpress = rho_a*287*ambtemp;
injvel = Cd/Ca*sqrt(2*(injpress - ambpress)/rho_f);
roi_vel = [0 injvel injvel 0 0];
roi_time = [0 50e-6 3e-3 3e-3+lengthoframpdown 8.0e-3];
InjParams = [roi_vel;roi_time];
theta = 23; % [deg] Spray spreading full-angle
velocity_profile = 0; % "0" for uniform and "1" for Abramovich real jet
adjust_theta = 1; % flag to alter theta uniform velocity profile
fueltemp = 363; % [K]
tend = 8e-3; % [s] simulation end time
CFL = 0.5; %Courant-Friedrichs-Lewy condition
InjType = 'interpolate'; %injection type
```

```matlab
fuel = importPhase('n_dodecane_mech.cti'); %gas-phase chemistry ...
    mechanism
ambient = importPhase('n_dodecane_mech.cti'); %gas-phase chemistry ...
    mechanism
react = importPhase('n_dodecane_mech.cti'); %gas-phase chemistry ...
    mechanism
diffflame = importPhase('n_dodecane_mech.cti'); %gas-phase chemistry ...
    mechanism
limtype = 'upwind'; %type of flux limiter
diffflameswitch = 1; %'1' to turn on diffusion flame reactor, '0' to ...
    turn it off
FLOL = ...
    1.45e10*ambtemp^(-3.74)*rho_a^(-1)*(D0*1e6)^0.34*injvel^(0.54)*...
     (o2frac*100*0.0627/21)^(-1); %[mm] flame lift-off length input


%% parameters (may need adjustment depending on mechanism)
A0 = Ca*pi/4*D0^2; % [m^2] nozzle area
u00 = injvel;
n2frac = 1 - o2frac; %N2 mole fraction
%(2*moles of carbon + moles of hydrogen/2)/(2*%O2)*MWfuel/MWair
stoich = (2*8 + 16/2)/(2*o2frac)*(14*2*n2frac + ...
    16*2*o2frac)/(8*12+16*1); %stoichiometry
Siebers = 0.683; %spreading angle correction factor for Siebers
if velocity_profile == 0 && adjust_theta == 1
     theta=atan(tand(theta)*Siebers)*180/pi; % [degrees] Siebers ...
        angle for uniform velocity calc.
end
Df = sqrt(Ca)*D0;
x0=Df/2/tand(theta/2); % [m] theoretical jet point origin
x = [dx/2:dx:total_length]; % coordinates of CV centers, relative to ...
    nozzle exit
A = [A0 pi*(tand(theta/2)*(x(1:end-1)+x0)).^2]; % area at CV centers
```

161

```matlab
V = A*dx; % CV Volumes (treat as cylinders
% endofinj = injmass/(rho_f*u00*A0) + lengthoframpup/2; % [s] end of ...
    injection
dt = CFL*dx/u00; %time step based on CFL condition
nt = tend/dt; %number of time steps
setstring = strcat('N2:',num2str(n2frac),',O2:',num2str(o2frac));
set(fuel,'T',fueltemp,'P',ambpress,'X','NXC12H26:1');
set(ambient,'T',ambtemp,'P',ambpress,'X',setstring);
set(react,'T',ambtemp,'P',ambpress,'X',setstring);
set(diffflame,'T',ambtemp,'P',ambpress,'X',setstring);
io2 = speciesIndex(react,'O2');
in2 = speciesIndex(react,'N2');
ic12h26 = speciesIndex(react,'NXC12H26');
nsp = nSpecies(react);
Unoz = InjVel(InjType,InjParams,0); % velocity at nozzle


% calculate alpha, beta, and gamma of the velocity distribution
alpha = ones(size(A))*1.5;   % Initialize alpha with fully-developed ...
    profile
i=2;
while(i)                     % previous alpha not yet steady
    r = rho_f/rho_a;         % density ratio
    P = [6*(A(i)/A0-1) -(7+18*r) -(2+33*r) -20*r -4*r]; % 4th order ...
        polynomial coefficients
    alpha(i) = max(roots(P));   % largest polynomial root is alpha
    if alpha(i)<1.5
        alpha(i) = 1.5;             % fully developed jet reached, so ...
            end loop
        i=0;
    else
        i=i+1;                      % fully developed jet not yet ...
            reached, so continue loop
```

```matlab
    end
end

beta = 6*(alpha+1).*(alpha+2)./(3*alpha+2)./(2*alpha+1); % ...
    integrated velocity profile factor
gamma = (alpha+1).*(alpha+2)./alpha.^2; % for converting from ...
    centerline to average velocity
beta(1) = 1;
gamma(1) = 1;
if velocity_profile==0  % if uniform velocity profile is used
    beta = ones(size(beta));
    gamma = ones(size(gamma));
    alpha = ones(size(alpha))*1e99;
end

%% initial conditions
rho = rho_a*ones(2,length(x));
T = ambtemp*ones(2,length(x));
u = zeros(2,length(x));
mf = zeros(2,length(x));
M = zeros(2,length(x));
Xf = zeros(2,length(x));
ma = [rho_a*V;rho_a*V];
marate = zeros(2,length(x));
mfrate = zeros(2,length(x));
Y = zeros(nsp,2,length(x));
for a = 1:length(x)
    Y(:,:,a) = massFractions(ambient)*ones(1,2);
end
enthalpy = enthalpy_mass(ambient)*ones(2,length(x));
% therm_diff = 0.05/(rho_a*cp_mass(ambient))*ones(2,length(x));
% spec_diff = zeros(2,length(x));
```

```matlab
%% initialize saved variables
stopsave = 5;
Tsave = zeros(round(nt/stopsave),length(x));
Ysave = zeros(nsp,round(nt/stopsave),length(x));
mfsave = zeros(round(nt/stopsave),length(x));
masave = zeros(round(nt/stopsave),length(x));
maratesave = zeros(round(nt/stopsave),length(x));
usave = zeros(round(nt/stopsave),length(x));
rhosave = zeros(round(nt/stopsave),length(x));
Xfsave = zeros(round(nt/stopsave),length(x));
Tsave(:,1) = fueltemp;
Ysave(ic12h26,:,1) = 1;
masave(:,1) = 0;
usave(:,1) = u00;
vaporpen = zeros(round(nt/stopsave),1);
enthalpysave = zeros(round(nt/stopsave),length(x));
% therm_diffusionsave = zeros(nt/stopsave,length(x));
% spec_diffusionsave = zeros(nsp,nt/stopsave,length(x));
therm_advectionsave = zeros(round(nt/stopsave),length(x));
spec_advectionsave = zeros(nsp,round(nt/stopsave),length(x));
HRR = zeros(1,length(x));
HRRsave = zeros(round(nt/stopsave),length(x));
% spec_diffusion = zeros(nsp,1,length(x));
% therm_diffusion = zeros(1,length(x));
spec_advection = zeros(nsp,1,length(x));
therm_advection = zeros(1,length(x));

j = 1;
i = 1;
time = 0;
stop = 3;
```

```matlab
%% load latest time step from previous run
% load('try.mat');
% T(1,:) = Tsave(find(Tsave(:,1) == 1000,1,'last'),:);
% Y(:,1,:) = Ysave(:,find(Tsave(:,1) == 1000,1,'last'),:);
% cp(1,:) = cpsave(find(Tsave(:,1) == 1000,1,'last'),:);
% cv(1,:) = cvsave(find(Tsave(:,1) == 1000,1,'last'),:);
% u(1,:) = usave(find(Tsave(:,1) == 1000,1,'last'),:);
% Xf(1,:) = Xfsave(find(Tsave(:,1) == 1000,1,'last'),:);
% rho(1,:) = rhosave(find(Tsave(:,1) == 1000,1,'last'),:);
% enthalpy(1,:) = enthalpysave(find(Tsave(:,1) == 1000,1,'last'),:);
% thermal_diff(1,:) = thermal_diffsave(find(Tsave(:,1) == ...
    1000,1,'last'),:);
% spec_diff(1,:) = spec_diffsave(find(Tsave(:,1) == 1000,1,'last'),:);
% i = length(time)+1;

%% main iteration
while time(end) < tend
    dtmax = 10e-6;
    umax = max([max(u(1,:)) Unoz 1]);
    dt = min([dtmax CFL*dx/umax]);
    Unoz = InjVel(InjType,InjParams,time(end));
    % boundary conditions at nozzle
    mf(1,1) = Unoz*rho_f*A0*dt;
    M(1,1) = Unoz^2*rho_f*A0*dt;
    u(1,1) = Unoz;
    u(2,1) = Unoz;
    rho(1,1) = rho_f;
    rho(2,1) = rho(1,1);
    Xf(1,1) = 1;
    Xf(2,1) = Xf(1,1);
    ma(1,1) = 0;
```

```matlab
    marate(1,1) = 0;
    if Unoz == 0
        T(1,1) = T(1,2);
    else
        T(1,1) = fueltemp;
    end
    T(2,1) = T(1,1);
    enthalpy(1,1) = enthalpy_mass(fuel);
%     spec_diff(1,1) = 0;
%     therm_diff(1,1) = 0.05/(rho_f*cp_mass(fuel));
    enthalpy(2,1) = enthalpy(1,1);
%     spec_diff(2,1) = spec_diff(1,1);
%     therm_diff(2,1) = therm_diff(1,1);
    Y(ic12h26,1,1) = 1;
    Y(in2,1,1) = 0;
    Y(io2,1,1) = 0;
    Y(ic12h26,2,1) = Y(ic12h26,1,1);
    Y(in2,2,1) = Y(in2,1,1);
    Y(io2,2,1) = Y(io2,1,1);

    for n = 2:stop
        % mass transport
        if n==2
            congrad1 = 0;
            congrad2 = (Xf(1,n)*u(1,n)*A(n)*beta(n) - ...
                Xf(1,n-1)*u(1,n-1)*A(n-1)*beta(n-1))/...
                (Xf(1,n+1)*u(1,n+1)*A(n+1)*beta(n+1) - ...
                Xf(1,n-1)*u(1,n-1)*A(n-1)*beta(n-1) + 1e-99);
        elseif n==length(x)
            congrad1 = (Xf(1,n-1)*u(1,n-1)*A(n-1)*beta(n-1) - ...
                Xf(1,n-2)*u(1,n-2)*A(n-2)*beta(n-2))/...
                (Xf(1,n)*u(1,n)*A(n)*beta(n) - ...
```

```matlab
            Xf(1,n-1)*u(1,n-1)*A(n-1)*beta(n-1) + 1e-99);
        congrad2 = 0;
    else
        congrad1 = (Xf(1,n-1)*u(1,n-1)*A(n-1)*beta(n-1) - ...
            Xf(1,n-2)*u(1,n-2)*A(n-2)*beta(n-2))/...
            (Xf(1,n)*u(1,n)*A(n)*beta(n) - ...
            Xf(1,n-1)*u(1,n-1)*A(n-1)*beta(n-1) + 1e-99);
        congrad2 = (Xf(1,n)*u(1,n)*A(n)*beta(n) - ...
            Xf(1,n-1)*u(1,n-1)*A(n-1)*beta(n-1))/...
            (Xf(1,n+1)*u(1,n+1)*A(n+1)*beta(n+1) - ...
            Xf(1,n-1)*u(1,n-1)*A(n-1)*beta(n-1) + 1e-99);
    end
    [limiter1,limiter2] = LimiterTypes(limtype,congrad1,congrad2);
    F1 = rho_f*Xf(1,n-1)*u(1,n-1)*A(n-1)*beta(n-1) + ...
        (1 - CFL)/2*(rho_f*Xf(1,n)*u(1,n)*A(n)*beta(n) - ...
        rho_f*Xf(1,n-1)*u(1,n-1)*A(n-1)*beta(n-1))*limiter1;
    F2 = rho_f*Xf(1,n)*u(1,n)*A(n)*beta(n) + ...
        (1 - CFL)/2*(rho_f*Xf(1,n+1)*u(1,n+1)*A(n+1)*beta(n+1) - ...
        rho_f*Xf(1,n)*u(1,n)*A(n)*beta(n))*limiter2;
    mf(2,n) = rho_f*Xf(1,n)*V(n) + (F1 - F2)*dt;


    % momentum transport
    if n==2
        congrad1 = 0;
        congrad2 = (rho(1,n)*u(1,n)^2*A(n)*beta(n) - ...
            rho(1,n-1)*u(1,n-1)^2*A(n-1)*beta(n-1))/...
            (rho(1,n+1)*u(1,n+1)^2*A(n+1)*beta(n+1) - ...
            rho(1,n-1)*u(1,n-1)^2*A(n-1)*beta(n-1) + 1e-99);

    elseif n==length(x)
        congrad1 = (rho(1,n-1)*u(1,n-1)^2*A(n-1)*beta(n-1) - ...
            rho(1,n-2)*u(1,n-2)^2*A(n-2)*beta(n-2))/...
```

```matlab
            (rho(1,n)*u(1,n)^2*A(n)*beta(n) - ...
                rho(1,n-1)*u(1,n-1)^2*A(n-1)*beta(n-1) + 1e-99);
        congrad2 = 0;
    else
        congrad1 = (rho(1,n-1)*u(1,n-1)^2*A(n-1)*beta(n-1) - ...
            rho(1,n-2)*u(1,n-2)^2*A(n-2)*beta(n-2))/...
            (rho(1,n)*u(1,n)^2*A(n)*beta(n) - ...
            rho(1,n-1)*u(1,n-1)^2*A(n-1)*beta(n-1) + 1e-99);
        congrad2 = (rho(1,n)*u(1,n)^2*A(n)*beta(n) - ...
            rho(1,n-1)*u(1,n-1)^2*A(n-1)*beta(n-1))/...
            (rho(1,n+1)*u(1,n+1)^2*A(n+1)*beta(n+1) - ...
            rho(1,n-1)*u(1,n-1)^2*A(n-1)*beta(n-1) + 1e-99);
    end
    [limiter1,limiter2] = LimiterTypes(limtype,congrad1,congrad2);
    F1 = rho(1,n-1)*u(1,n-1)^2*A(n-1)*beta(n-1) + ...
        (1 - CFL)/2*(rho(1,n)*u(1,n)^2*A(n)*beta(n) - ...
        rho(1,n-1)*u(1,n-1)^2*A(n-1)*beta(n-1))*limiter1;
    F2 = rho(1,n)*u(1,n)^2*A(n)*beta(n) + ...
        (1 - CFL)/2*(rho(1,n+1)*u(1,n+1)^2*A(n+1)*beta(n+1) - ...
        rho(1,n)*u(1,n)^2*A(n)*beta(n))*limiter2;
    M(2,n) = rho(1,n)*V(n)*u(1,n) + (F1 - F2)*dt;


    Xf(2,n) = mf(2,n)/rho_f/V(n);
    rho(2,n) = rho_f*Xf(2,n) + rho_a*(1 - Xf(2,n));
    u(2,n) = M(2,n)/(rho(2,n)*V(n));
    ma(2,n) = rho_a*(1 - Xf(2,n))*V(n);
    mfrate(2,n) = rho_f*Xf(2,n)*u(2,n)*A(n) - ...
        rho_f*Xf(2,n-1)*u(2,n-1)*A(n-1);


    %find entrainment and use in species and energy equation
    marate(2,n) = (A(n)*u(2,n) - A(n-1)*u(2,n-1))*rho_a;
```

```matlab
%diffusion flame reactor
if diffflameswitch ==1
igndelay = 1e6;
if ~isempty(find(Tsave>1500))
    [rowign colign] = ind2sub(size(Tsave),(find(Tsave>1500)));
    igndelay = time(min(rowign));
end
if n>=FLOL && time(end)>igndelay
Cmoletotal = 0;
Hmoletotal = 0;
Omoletotal = 0;
Nmoletotal = 0;
for specnumber = 1:nSpecies(react)
    specname = speciesName(react,specnumber);
    Cnum = nAtoms(react,specnumber,elementIndex(react,'C'));
    Hnum = nAtoms(react,specnumber,elementIndex(react,'H'));
    Onum = nAtoms(react,specnumber,elementIndex(react,'O'));
    Nnum = nAtoms(react,specnumber,elementIndex(react,'N'));
    Cmole = Cnum*moleFraction(react,specname);
    Hmole = Hnum*moleFraction(react,specname);
    Omole = Onum*moleFraction(react,specname);
    Nmole = Nnum*moleFraction(react,specname);
    Cmoletotal = Cmoletotal + Cmole;
    Hmoletotal = Hmoletotal + Hmole;
    Omoletotal = Omoletotal + Omole;
    Nmoletotal = Nmoletotal + Nmole;
end
ambientmole = (Hmoletotal/2 + 2*Cmoletotal - ...
    Omoletotal)/(2*o2frac);
if ambientmole>0
    diffreact = meanMolarMass(react)/...
        (meanMolarMass(ambient)*ambientmole+meanMolarMass(react));
```

169

```matlab
        diffamb = meanMolarMass(ambient)/...
            (meanMolarMass(ambient)*ambientmole+meanMolarMass(react));
        diffflameEnthalpy = (diffamb*enthalpy_mass(ambient)+...
            diffreact*enthalpy_mass(react))/(diffamb+diffreact);
        diffflameSpecies = (diffamb*massFractions(ambient)+...
            diffreact*massFractions(react))/(diffamb+diffreact);
        set(diffflame,'H',diffflameEnthalpy,'P',...
            ambpress,'Y',diffflameSpecies);
        equilibrate(diffflame,'HP');
    end
    end
end

% species transport
if n==2
    congrad1 = 0;
    congrad2 = (rho(1,n)*Y(:,1,n)*u(1,n)*A(n) - ...
        rho(1,n-1)*Y(:,1,n-1)*u(1,n-1)*A(n-1))./...
        (rho(1,n+1)*Y(:,1,n+1)*u(1,n+1)*A(n+1) - ...
        rho(1,n-1)*Y(:,1,n-1)*u(1,n-1)*A(n-1) + 1e-99);
elseif n==length(x)
    congrad1 = (rho(1,n-1)*Y(:,1,n-1)*u(1,n-1)*A(n-1) - ...
        rho(1,n-2)*Y(:,1,n-2)*u(1,n-2)*A(n-2))./...
        (rho(1,n)*Y(:,1,n)*u(1,n)*A(n) - ...
        rho(1,n-1)*Y(:,1,n-1)*u(1,n-1)*A(n-1) + 1e-99);
    congrad2 = 0;
else
    congrad1 = (rho(1,n-1)*Y(:,1,n-1)*u(1,n-1)*A(n-1) - ...
        rho(1,n-2)*Y(:,1,n-2)*u(1,n-2)*A(n-2))./...
        (rho(1,n)*Y(:,1,n)*u(1,n)*A(n) - ...
        rho(1,n-1)*Y(:,1,n-1)*u(1,n-1)*A(n-1) + 1e-99);
    congrad2 = (rho(1,n)*Y(:,1,n)*u(1,n)*A(n) - ...
```

```matlab
            rho(1,n-1)*Y(:,1,n-1)*u(1,n-1)*A(n-1))./...
            (rho(1,n+1)*Y(:,1,n+1)*u(1,n+1)*A(n+1) - ...
            rho(1,n-1)*Y(:,1,n-1)*u(1,n-1)*A(n-1) + 1e-99);
end

[limiter1,limiter2] = LimiterTypes(limtype,congrad1,congrad2);
F1 = rho(1,n-1)*Y(:,1,n-1)*u(1,n-1)*A(n-1) + ...
    (1 - CFL)/2*(rho(1,n)*Y(:,1,n)*u(1,n)*A(n) - ...
    rho(1,n-1)*Y(:,1,n-1)*u(1,n-1)*A(n-1))*limiter1;
F2 = rho(1,n)*Y(:,1,n)*u(1,n)*A(n) + ...
    (1 - CFL)/2*(rho(1,n+1)*Y(:,1,n+1)*u(1,n+1)*A(n+1) - ...
    rho(1,n)*Y(:,1,n)*u(1,n)*A(n))*limiter2;
%        mixing_length = 0.075*sqrt(A(n)/pi); %prandtl ...
    mixing length for axisymmetric jet
%        turb_visc = ...
    rho(2,n)*mixing_length^2*u(2,n)/(sqrt(A(n)/pi)); %eddy ...
    or turbulent viscosity
%        spec_diff(2,n) = 0+(turb_visc);
%        spec_diffusion(:,1,n) = ...
    spec_diff(1,n)*A(n+1)/dx*(Y(:,1,n+1) - Y(:,1,n)) - ...
    spec_diff(1,n)*A(n-1)/dx*(Y(:,1,n) - Y(:,1,n-1));
spec_advection(:,1,n) = F1 - F2 + ...
    marate(1,n)*massFractions(diffflame);
Y(:,2,n) = (rho(1,n)*V(n)*Y(:,1,n)...
    + (spec_advection(:,1,n))*dt)/(rho(2,n)*V(n));


% energy transport
if n==2
    congrad1 = 0;
    congrad2 = (rho(1,n)*enthalpy(1,n)*u(1,n)*A(n) - ...
        rho(1,n-1)*enthalpy(1,n-1)*u(1,n-1)*A(n-1))/...
        (rho(1,n+1)*enthalpy(1,n+1)*u(1,n+1)*A(n+1) - ...
        rho(1,n-1)*enthalpy(1,n-1)*u(1,n-1)*A(n-1) + 1e-99);
```

```matlab
        elseif n==length(x)
            congrad1 = (rho(1,n-1)*enthalpy(1,n-1)*u(1,n-1)*A(n-1) - ...
                rho(1,n-2)*enthalpy(1,n-2)*u(1,n-2)*A(n-2))/...
                (rho(1,n)*enthalpy(1,n)*u(1,n)*A(n) - ...
                rho(1,n-1)*enthalpy(1,n-1)*u(1,n-1)*A(n-1) + 1e-99);
            congrad2 = 0;
        else
            congrad1 = (rho(1,n-1)*enthalpy(1,n-1)*u(1,n-1)*A(n-1) - ...
                rho(1,n-2)*enthalpy(1,n-2)*u(1,n-2)*A(n-2))/...
                (rho(1,n)*enthalpy(1,n)*u(1,n)*A(n) - ...
                rho(1,n-1)*enthalpy(1,n-1)*u(1,n-1)*A(n-1) + 1e-99);
            congrad2 = (rho(1,n)*enthalpy(1,n)*u(1,n)*A(n) - ...
                rho(1,n-1)*enthalpy(1,n-1)*u(1,n-1)*A(n-1))/...
                (rho(1,n+1)*enthalpy(1,n+1)*u(1,n+1)*A(n+1) - ...
                rho(1,n-1)*enthalpy(1,n-1)*u(1,n-1)*A(n-1) + 1e-99);
        end
        [limiter1,limiter2] = LimiterTypes(limtype,congrad1,congrad2);
        F1 = rho(1,n-1)*enthalpy(1,n-1)*u(1,n-1)*A(n-1)  + ...
            (1 - CFL)/2*(rho(1,n)*enthalpy(1,n)*u(1,n)*A(n) - ...
            rho(1,n-1)*enthalpy(1,n-1)*u(1,n-1)*A(n-1))*limiter1;
        F2 = rho(1,n)*enthalpy(1,n)*u(1,n)*A(n)  + ...
            (1 - CFL)/2*(rho(1,n+1)*enthalpy(1,n+1)*u(1,n+1)*A(n+1) ...
                - ...
            rho(1,n)*enthalpy(1,n)*u(1,n)*A(n))*limiter2;
%        therm_diff(2,n) = 0.05/(cp_mass(react))+turb_visc;
%        therm_diffusion(1,n) = ...
    therm_diff(1,n)*A(n+1)/dx*(enthalpy(1,n+1) - enthalpy(1,n)) - ...
    therm_diff(1,n)*A(n-1)/dx*(enthalpy(1,n) - enthalpy(1,n-1));
        therm_advection(1,n) = F1 - F2 + ...
            marate(1,n)*enthalpy_mass(diffflame);
        enthalpy(2,n) = (rho(1,n)*V(n)*enthalpy(1,n)...
            + (therm_advection(1,n))*dt)/(rho(2,n)*V(n));
```

```matlab
    %insert enthalpy and species into reactor at node n and time t
    set(react,'H',enthalpy(2,n),'P',ambpress,'Y',Y(:,2,n));


    %let react for time step
     mw = molecularWeights(react);
     y0 = [temperature(react);massFractions(react)];
     tel = [0 dt];
     options = odeset('RelTol',1.e-5,'AbsTol',1.e-12,'Stats','off');
     out = ode15s(@conhp,tel,y0,options,react,mw);


    %update enthalpy and species
    T(2,n) = temperature(react);
    Y(:,2,n) = massFractions(react);
    enthalpy(2,n) = enthalpy_mass(react);
    HRR(1,n) = sum(gasconstant.*enthalpies_RT(react).*...
        temperature(react).*netProdRates(react));


    %reset diffusion flame reactor to ambient gases
    set(diffflame,'T',ambtemp,'P',ambpress,'X',setstring);


    %stop computation at head of jet
    stop = find(u(2,2:end)==0,1,'first')+1;
    if stop<3, stop = 3;
    elseif stop>length(x)-1, stop = length(x)-1;
    end
end


%copy cell contents from current time step to use as previous in ...
    next
%time step
u(2,1) = u(1,1);
```

```matlab
        T(2,1) = T(1,1);

        Y(:,2,1) = Y(:,1,1);

        mf(1,:) = mf(2,:);

        M(1,:) = M(2,:);

        u(1,:) = u(2,:);

        ma(1,:) = ma(2,:);

        marate(1,:) = marate(2,:);

        mfrate(1,:) = mfrate(2,:);

        rho(1,:) = rho(2,:);

        Xf(1,:) = Xf(2,:);

        T(1,:) = T(2,:);

        Y(:,1,:) = Y(:,2,:);

        enthalpy(1,:) = enthalpy(2,:);
%       therm_diff(1,:) = therm_diff(2,:);
%       spec_diff(1,:) = spec_diff(2,:);


        %save variables only at specified time step
        j = floor(i)+1;

        Tsave(j,:) = T(2,:);

        Ysave(:,j,:) = Y(:,2,:);

        mfsave(j,:) = mf(2,:);

        masave(j,:) = rho(2,:).*V.*(reshape(Y(in2,2,:),1,length(x)) + ...
            reshape(Y(io2,2,:),1,length(x)));

        maratesave(j,:) = marate(2,:);

        usave(j,:) = u(2,:);

        Xfsave(j,:) = Xf(2,:);

        rhosave(j,:) = rho(2,:);

        enthalpysave(j,:) = enthalpy(2,:);
%       therm_diffusionsave(j,:) = therm_diffusion(1,:);
        spec_advectionsave(:,j,:) = spec_advection(:,1,:);

        therm_advectionsave(j,:) = therm_advection(1,:);
%       spec_diffusionsave(:,j,:) = spec_diffusion(:,1,:);
```

174

```matlab
        HRRsave(j,:) = HRR(1,:);


        % Vapor penetration
        ii = find(M(2,:)/dt>0.05*max(M(2,:)));
        if isempty(ii), vaporpen(i+1) = 0;
        else vaporpen(i) = x(ii(end));
        end


        time = [time time(end)+dt];% update time
        time(end)
        i=i+1;          % update iteration count
end
```

APPENDIX C

LIMITS OF OH* CHEMILUMINESCENCE MEASUREMENT

C.1 Limits of OH* Chemiluminescence Measurement

Chemiluminescence measurements often remain qualitative due to significant challenges in relating the measured signal to the quantity of the emitting species. The emitting species must first become excited through chemical reactions and/or thermal excitation and then relaxed back down to ground state through spontaneous radiative transitions. Photons emitted through these transitions are captured by the camera and then recorded as the chemiluminescence signal. But, the excited species may also return to ground state non-radiatively through collisional quenching or could be removed from it's excited state through reaction with another molecule. Thus, the ability to relate the measured signal to the quantity of the emitting species depends on knowledge of these sub-steps.

Often times, collisional quenching dominates the entire process and the limiting step is the formation rate of the excited species [112]. Thus, the excited species can be assumed to be in quasi-steady state and can be found with the following relation,

$$[OH*] = \frac{k_1[O][H][M] + k_2[CH][O_2]}{\sum_j k_j[M_j]},$$ (57)

where $[XY]$ is the species concentration and k is the reaction rate constant. The reaction rate constants are taken as those given in Ref. [112]. From this relation, we can observe the time evolution of OH* during ignition of a stoichiometric mixture of n-dodecane (363 K) and air (900 K) in Figure 80a. The majority of the emission occurs in approximately 1 μs, which is on the order of a typical camera exposure duration.

176

Therefore, it is likely that a camera will collect much of the light emitted during ignition. In other words, time integration during the ignition process is required to yield a meaningful comparison to other conditions.
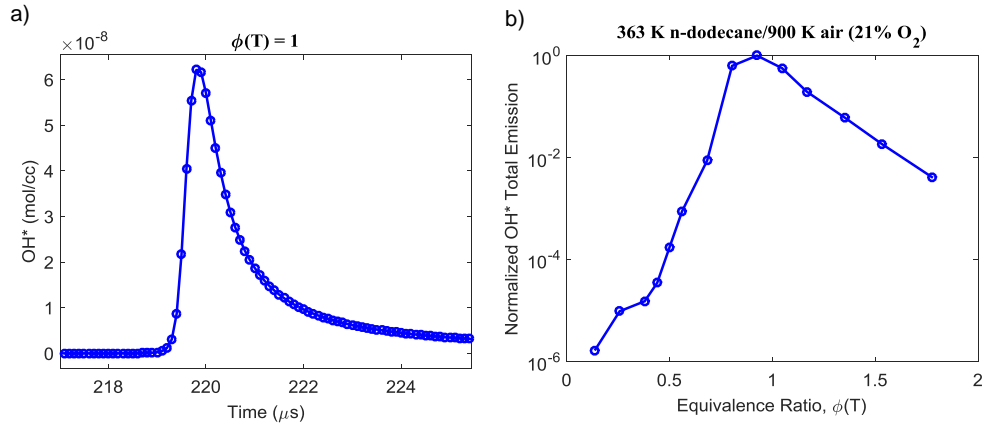
Figure 80: (a) OH* concentration during ignition of stoichiometric n-dodecane/air mixture and (b) Total OH* emission during ignition normalized by maximum value in series. N-dodecane - 363 K and air (21% O2) - 900 K.

Assuming all other parameters equal, e.g. camera collection optics, volume of reacting gas, etc., we can observe how the chemiluminescence signal should vary with equivalence ratio in Figure 80b. The data in this figure has been normalized by the maximum value observed at the stoichiometric condition to make the previous assumption meaningful. If the camera captures data with 12 bit resolution, the maximum measurable intensity will be 4096 counts at the stoichiometric conditions. A typical noise floor is on the order 10 counts, such that the lowest observable signal is two orders of magnitude below the maximum. Based on Figure 80b, this implies that the lower bound of equivalence ratio detection is approximately 0.5-0.7.

It may be reasonable to extend this understanding of detection limits to measurements of combustion recession because autoignition appears to dominate. Caution should be exercised, however, because some of the assumptions may not be valid in this context. For instance, the volume of reacting gas gets smaller towards the nozzle, which will naturally decrease the chemiluminescence emitted from this region.

Also, the relative contributions of premixed and non-premixed flames to the total chemiluminescence is unknown, which have their own dependencies on fluid dynamic parameters not considered in the previous analysis, e.g. flame surface area, strain rate, etc.

REFERENCES

[1] M. P. Musculus, P. C. Miles, and L. M. Pickett, "Conceptual models for partially premixed low-temperature diesel combustion," *Progress in Energy and Combustion Science*, vol. 39, no. 2, pp. 246–283, 2013.

[2] W. Colban, P. Miles, and S. Oh, "Effect of intake pressure on emissions from an automotive diesel engine operating in low temperature combustion regimes," in *SAE Paper 2007-01-4063*.

[3] B. Keeler and P. Shayler, "Constraints on fuel injection and EGR strategies for diesel PCCI-type combustion," in *SAE Paper 2008-01-1327*.

[4] S. Kook, C. Bae, P. Miles, D. Choi, and L. Pickett, "The influence of charge dilution and injection timing on low-temperature diesel combustion and emissions," in *SAE Paper 2005-01-3837*.

[5] W. Hardy and R. R.D., "A study of the effects of high EGR, high equivalence ratio, and mixing time on emissions levels in a heavy-duty diesel engine for PCCI combustion," in *SAE Paper 2006-01-0026*.

[6] K. Kitano, R. Nishiumi, Y. Tsukasaki, and T. Toshiaki, "Effects of fuel properties on premixed charge compression ignition combustion in a direct injection diesel engine," in *SAE Paper 2003-01-1815*.

[7] T. Kanda, T. Hakozaki, T. Uchimoto, J. Hatano, N. Kitayama, and H. Sono, "PCCI operation with early injection of conventional diesel fuel," in *SAE Paper 2005- 01-0378*.

[8] S. Kimura, O. Aoki, H. Ogawa, S. Muranaka, and Y. Enomoto, "New combustion concept for ultra-clean and high-efficiency small DI diesel engines," in *SAE Paper 1999-01-3681*.

[9] S. Kimura, O. Aoki, Y. Kitahara, and E. Aiyoshizawa, "Ultra-clean combustion technology combining a low-temperature and premixed combustion concept for meeting future emission standards," in *SAE Paper 2001-01-0200*.

[10] M. P. Musculus, T. Lachaux, L. M. Pickett, and C. A. Idicheria, "End-of-injection over-mixing and unburned hydrocarbon emissions in low-temperature-combustion diesel engines," in *SAE Paper 2007-01-0907*.

[11] C. P. Koci, Y. Ra, R. Krieger, M. Andrie, D. E. Foster, R. M. Siewert, and P. Miles, "Detailed unburned hydrocarbon investigations in a highly-dilute diesel low temperature combustion regime," in *SAE Paper 2009-01-0928*.

[12] C. L. Genzale, R. D. Reitz, and M. P. Musculus, "Effects of spray targeting on mixture development and emissions formation in late-injection low-temperature heavy-duty diesel combustion," *Proceedings of the combustion institute*, vol. 32, no. 2, pp. 2767–2774, 2009.

[13] J. O'Connor and M. Musculus, "Optical investigation of the reduction of unburned hydrocarbons using close-coupled post injections at LTC conditions in a heavy-duty diesel engine," in *SAE Paper 2013-01-0910*.

[14] J. Dec, "A conceptual model of di diesel combustion based on laser-sheet imaging," in *SAE Paper 970873*.

[15] H. Kosaka, V. H. Drewes, L. Catalfamo, A. A. Aradi, N. Iida, and T. Kamimoto, "Two–dimensional imaging of formaldehyde formed during the ignition process of a diesel fuel spray," tech. rep., SAE Technical Paper, 2000.

[16] J. E. Dec and C. Espey, "Chemiluminescence imaging of autoignition in a di diesel engine," tech. rep., SAE Technical paper, 1998.

[17] Y. B. Zeldovich, "The oxidation of nitrogen in combustion and explosions," *Acta Physicochim. URSS*, vol. 21, no. 4, pp. 577–628, 1946.

[18] D. L. Siebers and B. S. Higgins, "Flame lift-off on direct-injection diesel sprays under quiescent conditions," in *SAE Paper 2001-01-0530*.

[19] D. L. Siebers, B. S. Higgins, and L. M. Pickett, "Flame lift-off on direct-injection diesel fuel jets: Oxygen concentration effects," in *SAE Paper 2002-01-0890*.

[20] Y. Wakuri, M. Fujii, T. Amitani, and R. Tsuneya, "Studies on the penetration of fuel spray in a diesel engine," *Bulletin of JSME*, vol. 3, no. 9, pp. 123–130, 1960.

[21] J. Naber and D. L. Siebers, "Effects of gas density and vaporization on penetration and dispersion of diesel sprays," tech. rep., SAE technical paper, 1996.

[22] H. Hiroyasu and M. Arai, "Structures of fuel sprays in diesel engines," in *SAE paper 900475*, 1990.

[23] H. Hiroyasu, T. Kadota, and M. Arai, "Supplementary comments: fuel spray characterization in diesel engines," *Combustion modeling in reciprocating engines*, pp. 369–408, 1980.

[24] J. Dent, "A basis for the comparison of various experimental methods for studying spray penetration," in *SAE paper 710571*, 1971.

[25] D. L. Siebers, "Scaling liquid-phase fuel penetration in diesel sprays based on mixing-limited vaporization," tech. rep., SAE technical paper, 1999.

[26] C. Bajaj, J. Abraham, and L. M. Pickett, "Vaporization effects on transient diesel spray structure," *Atomization and Sprays*, vol. 21, no. 5, 2011.

[27] J. Manin, M. Bardi, L. Pickett, R. Dahms, and J. Oefelein, "Microscopic investigation of the atomization and mixing processes of diesel sprays injected into high pressure and temperature environments," *Fuel*, vol. 134, pp. 531–543, 2014.

[28] R. N. Dahms and J. C. Oefelein, "On the transition between two-phase and single-phase interface dynamics in multicomponent fluids at supercritical pressures," *Physics of Fluids (1994-present)*, vol. 25, no. 9, p. 092103, 2013.

[29] C. K. Westbrook, "Chemical kinetics of hydrocarbon ignition in practical combustion systems," *Proceedings of the Combustion Institute*, vol. 28, no. 2, pp. 1563–1577, 2000.

[30] M. Mehl, W. J. Pitz, C. K. Westbrook, and H. J. Curran, "Kinetic modeling of gasoline surrogate components and mixtures under engine conditions," *Proceedings of the Combustion Institute*, vol. 33, no. 1, pp. 193–200, 2011.

[31] E. Mastorakos, "Ignition of turbulent non-premixed flames," *Progress in Energy and Combustion Science*, vol. 35, no. 1, pp. 57–97, 2009.

[32] M. Bolla, D. Farrace, Y. M. Wright, K. Boulouchos, and E. Mastorakos, "Influence of turbulence–chemistry interaction for n-heptane spray combustion under diesel engine conditions with emphasis on soot formation and oxidation," *Combustion Theory and Modelling*, vol. 18, no. 2, pp. 330–360, 2014.

[33] Y. Pei, E. R. Hawkes, S. Kook, G. M. Goldin, and T. Lu, "Modelling n-dodecane spray and combustion with the transported probability density function method," *Combustion and Flame*, vol. 162, no. 5, pp. 2006–2019, 2015.

[34] L. M. Pickett, D. L. Siebers, and C. A. Idicheria, "Relationship between ignition processes and the lift-off length of diesel fuel jets," tech. rep., SAE technical paper, 2005.

[35] L. M. Pickett, S. Kook, H. Persson, and Ö. Andersson, "Diesel fuel jet lift-off stabilization in the presence of laser-induced plasma ignition," *Proceedings of the Combustion Institute*, vol. 32, no. 2, pp. 2793–2800, 2009.

[36] H. Juneja, Y. Ra, and R. D. Reitz, "Optimization of injection rate shape using active control of fuel injection," tech. rep., SAE Technical Paper, 2004.

[37] X. Wang, Z. Huang, O. A. Kuti, W. Zhang, and K. Nishida, "Experimental and analytical study on biodiesel and diesel spray characteristics under ultra-high injection pressure," *International journal of heat and fluid flow*, vol. 31, no. 4, pp. 659–666, 2010.

[38] L. M. Pickett and D. L. Siebers, "An investigation of diesel soot formation processes using micro-orifices," *Proceedings of the Combustion Institute*, vol. 29, no. 1, pp. 655–662, 2002.

[39] B. Hu, M. P. Musculus, and J. C. Oefelein, "The influence of large-scale structures on entrainment in a decelerating transient turbulent jet revealed by large eddy simulation," *Physics of Fluids (1994-present)*, vol. 24, no. 4, p. 045106, 2012.

[40] M. P. Musculus, "Entrainment waves in decelerating transient turbulent jets," *Journal of Fluid Mechanics*, vol. 638, pp. 117–140, 2009.

[41] M. P. Musculus and K. Kattke, "Entrainment waves in diesel jets," in *SAE Paper 2009-01-1355*.

[42] S. Singh and M. P. Musculus, "Numerical modeling and analysis of entrainment in turbulent jets after the end of injection," *Journal of Fluids Engineering*, vol. 132, no. 8, p. 081203, 2010.

[43] W. E. Eagle, M. P. B. Musculus, and B. G. Malbec, L-M.C., "Measuring transient entrainment rates of a confined vaporizing diesel jet," in *ILASS Americas 26th Annual Conference on Liquid Atomization and Spray Sytems, Portland, OR, May 2014*.

[44] C. Espey and J. Dec, "Diesel engine combustion studies in a newly designed optical-access engine using high-speed visualization and 2-D laser imaging," in *SAE Paper 930971*.

[45] M. K. Bobba, C. L. Genzale, and M. P. Musculus, "Effect of ignition delay on in-cylinder soot characteristics of a heavy duty diesel engine operating at low temperature conditions," *SAE International Journal of Engines*, vol. 2, no. 2009-01-0946, pp. 911–924, 2009.

[46] C. L. Genzale, R. D. Reitz, and M. P. Musculus, "Effects of piston bowl geometry on mixture development and late-injection low-temperature combustion in a heavy-duty diesel engine," *SAE International Journal of Engines*, vol. 1, no. 2008-01-1330, pp. 913–937, 2008.

[47] L. T. Musculus MPB, "Two-stage ignition and unburned fuel emissions for heavy-duty diesel low-temperature combustion of neat n-heptane,"

[48] A. Swantek, D. Duke, F. Tilocco, N. Sovis, C. Powell, and A. Kastengren, "End of injection, mass expulsion behaviors in single hole diesel fuel injectors," *Proceedings of ILASS Americas*, 2014.

[49] S. Moon, W. Huang, Z. Li, and J. Wang, "End-of-injection fuel dribble of multi-hole diesel injector: Comprehensive investigation of phenomenon and discussion on control strategy," *Applied Energy*, vol. 179, pp. 7–16, 2016.

[50] W. Eagle and M. Musculus, "Cinema-stereo imaging of fuel dribble after the end of injection in an optical heavy-duty diesel engine," in *Thiesel Conference Proceedings*, 2014.

[51] B. W. Knox, C. L. Genzale, L. M. Pickett, J. M. Garcia-Oliver, and W. Vera-Tudela, "Combustion recession after end of injection in diesel sprays," *SAE Int. J. Engines*, vol. 8, no. 2015-01-0797, pp. 679–695, 2015.

[52] B. W. Knox and C. L. Genzale, "Effects of end-of-injection transients on combustion recession in diesel sprays," *SAE Int. J. Engines*, vol. 9, no. 2016-01-0745, pp. 932–949, 2016.

[53] B. W. Knox, M. J. Franze, and C. L. Genzale, "Diesel spray rate-of-momentum measurement uncertainties and diagnostic considerations," *Journal of Engineering for Gas Turbines and Power*, vol. 138, no. 3, p. 031507, 2016.

[54] J. A. Falcone, B. W. Knox, and C. L. Genzale, "Identifying uncertainties in diesel spray rate-of-momentum transients under elevated back pressure," in *ASME 2015 Internal Combustion Engine Division Fall Technical Conference*, pp. V001T02A013–V001T02A013, American Society of Mechanical Engineers, 2015.

[55] B. W. Knox and C. L. Genzale, "Reduced-order numerical model for transient reacting diesel sprays with detailed kinetics," *Int. J. Engine Res.*, vol. 17, no. 3, pp. 261–279, 2016.

[56] M. Meijer, B. Somers, J. Johnson, J. Naber, S.-Y. Lee, L. M. Malbec, G. Bruneaux, L. M. Pickett, M. Bardi, R. Payri, *et al.*, "Engine combustion network (ecn): Characterization and comparison of boundary conditions for different combustion vessels," *Atomization and Sprays*, vol. 22, no. 9, pp. 777–806, 2012.

[57] "Engine combustion network," Aug. 2013.

[58] W. Bosch, "The fuel rate indicator: a new measuring instrument for display of the characteristics of individual injection," tech. rep., SAE Technical Paper, 1966.

[59] J. Manin, A. Kastengren, and R. Payri, "Understanding the acoustic oscillations observed in the injection rate of a common-rail direct injection diesel injector," *Journal of engineering for gas turbines and power*, vol. 134, no. 12, p. 122801, 2012.

[60] J. Desantes, R. Payri, F. Salvador, and J. Gimeno, "Measurements of spray momentum for the study of cavitation in diesel injection nozzles," in *SAE Paper 2003-01-0703*.

[61] T. Husberg, V. Manente, R. Ehleskog, and S. Andersson, "Fuel flow impingement measurements on multi-orifice diesel nozzles," tech. rep., SAE Technical Paper, 2006.

[62] M. Lindström and H.-E. Angstrom, "Development of a fuel spray impulse measurement device and correlation with time resolved mass flow," tech. rep., SAE Technical Paper, 2009.

[63] H. Zaheer, "Transient microscopy of primary atomization in gasoline direct injection sprays," 2015.

[64] S. A. Skeen, J. Manin, and L. M. Pickett, "Simultaneous formaldehyde plif and high-speed schlieren imaging for ignition visualization in high-pressure spray flames," *Proc. Combust. Inst.*, vol. 35, no. 3, pp. 3167–3174, 2015.

[65] G. S. Settles, *Schlieren and shadowgraph techniques.* 2001.

[66] P. M. Lillo, L. M. Pickett, H. Persson, O. Andersson, and S. Kook, "Diesel spray ignition detection and spatial/temporal correction," *SAE International Journal of Engines*, vol. 5, no. 2012-01-1239, pp. 1330–1346, 2012.

[67] M. P. Musculus and L. M. Pickett, "Diagnostic considerations for optical laser-extinction measurements of soot in high-pressure transient combustion environments," *Combustion and Flame*, vol. 141, no. 4, pp. 371–391, 2005.

[68] L. Pickett, J. Caton, M. Musculus, and A. Lutz, "Evaluation of the equivalence ratio-temperature region of diesel soot precursor formation using a two-stage lagrangian model," *International Journal of Engine Research*, vol. 7, no. 5, pp. 349–370, 2006.

[69] J. Desantes, J. Pastor, J. García-Oliver, and J. Pastor, "A 1d model for the description of mixing-controlled reacting diesel sprays," *Combustion and Flame*, vol. 156, no. 1, pp. 234–249, 2009.

[70] V. Macián, R. Payri, X. Margot, and F. Salvador, "A cfd analysis of the influence of diesel nozzle geometry on the inception of cavitation," *Atomization and sprays*, vol. 13, no. 5&6, 2003.

[71] H. Chaves, M. Knapp, A. Kubitzek, F. Obermeier, and T. Schneider, "Experimental study of cavitation in the nozzle hole of diesel injectors using transparent nozzles," tech. rep., SAE technical paper, 1995.

[72] D. Goodwin, "Cantera: Object-oriented software for reacting flows," *California Institute for Technology (Caltech).¡ http://www. cantera. org¿(accessed July, 2007)*, 2005.

[73] "Mechanisms," Aug. 2013.

[74] "Chemical-kinetic mechanisms for combustion applications," Aug. 2013.

[75] R. Novella, A. García, J. Pastor, and V. Domenech, "The role of detailed chemical kinetics on cfd diesel spray ignition and combustion modelling," *Mathematical and Computer Modelling*, vol. 54, no. 7, pp. 1706–1719, 2011.

[76] B. R. Stanmore, J. F. Brilhac, and P. Gilot, "The oxidation of soot: a review of experiments, mechanisms and models," *Carbon*, vol. 39, no. 15, pp. 2247–2268, 2001.

[77] D. Han and M. G. Mungal, "Direct measurement of entrainment in reacting/nonreacting turbulent jets," *Combustion and flame*, vol. 124, no. 3, pp. 370–386, 2001.

[78] J. E. Broadwell and A. E. Lutz, "A turbulent jet chemical reaction model: Nox production in jet flames," *Combust. Flame*, vol. 114, no. 3, pp. 319–335, 1998.

[79] L. M. Pickett, J. Manin, C. L. Genzale, D. L. Siebers, M. P. Musculus, and C. A. Idicheria, "Relationship between diesel fuel spray vapor penetration/dispersion and local fuel mixture fraction," *SAE International Journal of Engines*, vol. 4, no. 1, pp. 764–799, 2011.

[80] L. M. Pickett, J. Manin, R. Payri, M. Bardi, and J. Gimeno, "Transient rate of injection effects on spray development," tech. rep., SAE Technical Paper, 2013.

[81] J. Benajes, R. Payri, M. Bardi, and P. Martí-Aldaraví, "Experimental characterization of diesel ignition and lift-off length using a single-hole ecn injector," *Applied Thermal Engineering*, vol. 58, no. 1, pp. 554–563, 2013.

[82] H. Wang, Y. Ra, M. Jia, and R. D. Reitz, "Development of a reduced n-dodecane-pah mechanism and its application for n-dodecane soot predictions," *Fuel*, vol. 136, pp. 25–36, 2014.

[83] L. Cai, L. Krger, and H. Pitsch. personal communication.

[84] E. Ranzi, A. Frassoldati, R. Grana, A. Cuoci, T. Faravelli, A. Kelley, and C. Law, "Hierarchical and comparative kinetic modeling of laminar flame speeds of hydrocarbon and oxygenated fuels," *Progress in Energy and Combustion Science*, vol. 38, no. 4, pp. 468–501, 2012.

[85] C. A. Idicheria and L. M. Pickett, "Formaldehyde visualization near lift-off location in a diesel jet," in *SAE paper 2006-01-3434*, 2006.

[86] R. Seiser, H. Pitsch, K. Seshadri, W. J. Pitz, and H. J. Gurran, "Extinction and autoignition of n-heptane in counterflow configuration," *Proceedings of the Combustion Institute*, vol. 28, no. 2, pp. 2029–2037, 2000.

[87] R. Collin, J. Nygren, M. Richter, M. Aldén, L. Hildingsson, and B. Johansson, "Simultaneous oh-and formaldehyde-lif measurements in an hcci engine," tech. rep., SAE Technical paper, 2003.

[88] H. W. Coleman and W. G. Steele, *Experimentation, validation, and uncertainty analysis for engineers*. John Wiley & Sons, 2009.

[89] R. Peters, "Penetration and dispersion research of non-reacting evaporating diesel sprays," *Graduation Rep., Eindhoven Univ. of Technology Mechanical Engineering-Combustion Technology*, 2007.

[90] J. Gimeno, "Desarrollo y aplicación de la medida del flujo de cantidad de movimiento de un chorro diesel," *PhD diss., tesis doctoral UPV*, 2008.

[91] "Pcb 113b26 product manual., pcb piezotronics inc., depew, ny.."

[92] "Kistler 9215 product manual, kistler instrument corporation., amherst, ny.."

[93] "Kistler 4065 product manual, kistler instrument corporation., amherst, ny.."

[94] L. M. Pickett, J. Manin, A. Kastengren, and C. Powell, "Comparison of near-field structure and growth of a diesel spray using light-based optical microscopy and x-ray radiography," *SAE International Journal of Engines*, vol. 7, no. 2014-01-1412, pp. 1044–1053, 2014.

[95] P. Leick, T. Riedel, G. Bittlinger, C. Powell, A. Kastengren, and J. Wang, "X-ray measurements of the mass distribution in the dense primary break-up region of the spray from a standard multi-hole common-rail diesel injection system," in *21st Annual ILASS-Europe Conference*, 2007.

[96] A. Swantek, A. Kastengren, D. Duke, Z. Tilocco, N. Sovis, and C. F. Powell, "Quantification of shot-to-shot variation in single hole diesel injectors," *SAE International Journal of Fuels and Lubricants*, vol. 8, no. 2015-01-0936, pp. 160–166, 2015.

[97] R. Payri, J. Gimeno, J. Cuisano, and J. Arco, "Hydraulic characterization of diesel engine single-hole injectors," *Fuel*, vol. 180, pp. 357–366, 2016.

[98] W. Nurick, "Orifice cavitation and its effect on spray mixing," *Journal of fluids engineering*, vol. 98, no. 4, pp. 681–687, 1976.

[99] J. J. López, F. Salvador, A. Oscar, and J. Arrègle, "A comprehensive study on the effect of cavitation on injection velocity in diesel nozzles," *Energy Conversion and Management*, vol. 64, pp. 415–423, 2012.

[100] P. Linstrom and W. Mallard, *NIST Chemistry WebBook, NIST Standard Reference Database*. National Institute of Standards and Technology, Gaithersburg MD, 20899.

[101] J. Boree, N. Atassi, and G. Charnay, "Phase averaged velocity field in an axisymmetric jet subject to a sudden velocity decrease," *Exp. Fluids*, vol. 21, no. 6, pp. 447–456, 1996.

[102] S. Kook, L. M. Pickett, and M. P. B. Musculus, "Influence of diesel injection parameters on end-of-injection liquid length recession," in *SAE Paper 2009-01-1356*.

[103] A. Cavaliere and M. de Joannon, "Mild combustion," *Progress in Energy and Combustion science*, vol. 30, no. 4, pp. 329–366, 2004.

[104] P. Yeung and S. Pope, "An algorithm for tracking fluid particles in numerical simulations of homogeneous turbulence," *Journal of computational physics*, vol. 79, no. 2, pp. 373–416, 1988.

[105] T. Yao, Y. Pei, B. J. Zhong, S. Som, and T. Lu, "A hybrid mechanism for n-dodecane combustion with optimized low-temperature chemistry," in *9th US National Combustion Meeting. Cincinnati. OH, 114IC-0055*, 2015.

[106] J. Manin, S. Skeen, L. Pickett, E. Kurtz, and J. E. Anderson, "Effects of oxygenated fuels on combustion and soot formation/oxidation processes," *SAE Int. J. Fuels Lubr.*, vol. 7, no. 2014-01-2657, pp. 704–717, 2014.

[107] L. M. Pickett and D. L. Siebers, "Soot in diesel fuel jets: effects of ambient temperature, ambient density, and injection pressure," *Combust. Flame*, vol. 138, no. 1, pp. 114–135, 2004.

[108] G. Lequien, S. Skeen, J. Manin, L. M. Pickett, and O. Andersson, "Ignition quality effects on lift-off stabilization of synthetic fuels," *SAE Int. J. Engines*, vol. 8, no. 2015-01-0792, pp. 625–634, 2015.

[109] F. R. Westlye, K. Penney, S. Skeen, J. Manin, L. Pickett, , and A. Ivarsson, "Experimental setup for high temporal diffuse back-illumination measurements," *Applied Optics*, submitted 2016.

[110] A. Kastengren, C. F. Powell, F. Z. Tilocco, Z. Liu, S. Moon, X. Zhang, and J. Gao, "End-of-injection behavior of diesel sprays measured with x-ray radiography," *Journal of Engineering for Gas Turbines and Power*, vol. 134, no. 9, p. 094501, 2012.

[111] Y. Jung, J. Manin, S. Skeen, and L. M. Pickett, "Measurement of liquid and vapor penetration of diesel sprays with a variation in spreading angle," tech. rep., SAE Technical Paper, 2015.

[112] V. Nori and J. Seitzman, "Evaluation of chemiluminescence as a combustion diagnostic under varying operating conditions," *AIAA paper*, vol. 953, 2008.